May 2024

Characterisation of the first large-scale prototypes for the ALICE ITS3 Upgrade

Styliani Paniskaki

Project duration: 9 months, 60 ECTS

Thesis submitted for degree Master of Science
Supervised by David Silvermyr

LUND
UNIVERSITY

Department of Physics
Division of Particle & Nuclear Physics

Abstract

This thesis deals with the characterization of the approved inner tracker upgrade of the ALICE experiment involving an innovative and ultra-thin silicon detector with a cylindrical geometry. During this thesis work, Monolithic Active Pixel Sensors (MAPS) were studied for the first large-scale prototype of the upgrade, together with a sensor of the same technology with smaller size. Properties of the detectors were studied with test beams, resulting in information about the detection efficiency and spatial resolution of the pixel matrix of the prototypes. The smaller prototype was also tested under nominal irradiation levels, in order to evaluate the performance of the detector under the actual conditions in the ALICE experiment over time.

Acknowledgments

First of all, I would like to thank my supervisor, David Silvermyr, for all the help and guidance that he provided to me for the last year, as well as for the opportunity to work on such an interesting project and have the possibility to work closely on the detector at CERN.

Secondly, I would like to thank Miljenko Suljic from CERN and Iaroslav Panasenko, post-doctoral researcher at Lund University, for always explaining to me in detail how the detector works, while also providing a great environment of work at CERN. I would also like to thank all the people that I worked together with on the test beams, and special thanks to Livia Terlizzi for the good cooperation in the data analysis.

Lastly, I would like to thank my friends and family for all the support they provided me with, in order to study abroad and have these opportunities.

List of acronyms

ADC Analog to Digital Converter
ALICE A Large Ion Collider Experiment
ALPIDE ALICE PIxel DEtector
ATLAS A Toroidal LHC ApparatuS
ASICs Application-Specific Integrated Circuits
CERN The European Organization for Nuclear Research
CFRP Carbon Fibre Reinforced Plastic
CMOS Complementary Metal-Oxide Semiconductor
CMS Compact Muon Solenoid
CUID Carrier Unique ID
CYSS CYlindrical Structure Cell
DAC Digital to Analog Converter
DAQ Data AcQuisition
DUT Device Under Test
EMCAL ElectroMagnetic Calorimeter
ER Engineering Run
FHR Fake-Hit Rate
FMD Forward Multiplicity Detector
FPC Flexible Printed Circuit
FPGA Field Programmable Gate Arrays
HIC Hybrid Integrated Circuit
HMPID High Momentum Particle Identification Detector
HU Half Unit
IB Inner Barrel
I/O Input/Output
ITS Inner Tracking System
LED Light Emitting Diode
LEIR Low Energy Ion Ring
LHC Large Hadron Collider
LHCb Large Hadron Collider beauty
LS Long Shutdown
MAPS Monolithic Active Pixel Sensor
MIP Minimum Ionising Particle
MOSAIX MOnolithic Stitched pArticle pIXel detector
MOSS MOnolithic Stitched Sensor
OB Outer Barrel
PCB Printed Circuit Board
PHOS PHOton Sprectrometer
PMD Photon Multiplicity Detector
PS Proton Synchrotron
QCD Quantum ChromoDynamics
QGP Quark Gluon Plasma
RICH Ring-Imaging CHerenkov
ROI Region Of Interest
RSU Repeated Sensor Unit
SDD Silicon Drift Detector

SNR Signal to Noise Ratio
SPD Silicon Pixel Detector
SPS Super Proton Synchrotron
SSD Silicon Strip Detector
TDR Technical Design Report
THR THReshold
TOF Time-Of-Flight
TPC Time Projection Chamber
TPSCo Tower Partners Semiconductor Company
TRD Transition Radiation Detector
USB Universal Serial Bus
YETS Year-End Technical Stop

Contents

Chapter 1

1 Introduction

Mankind has always been eager to understand the world surrounding us. Theoretical ideas about fundamental building blocks of matter have been around for millennia. The first subatomic particle to be discovered was the electron in 1897. Many more ideas and discoveries have resulted in a remarkable insight into the foundational structure of matter. Everything in the universe, as far as we know now, is found to be made from a few basic building blocks called elementary particles, governed by four fundamental forces. Our current understanding of how these particles are related to three of the fundamental forces is that, described in the Standard Model of particle physics [1]. The model was first developed in the early 1960s and it successfully explained almost all experimental results and predicted a wide variety of phenomena. Among the many experiments done, a famous example of the success of the theory was the discovery of the Higgs boson in 2012. Peter Higgs, along with others, proposed the existence of this particle in 1964, but it was only in 2012, almost 50 years later, that the experimental data have found a new particle with a mass of 125 GeV/c^2, thus establishing the Standard Model as a successful theory [2, 3].

In order to conduct experiments that would help proving or rejecting these different theoretical ideas, scientists were in need of large-scale experiments at high energies. From 1952, the CERN laboratory started getting constructed near the border between France and Switzerland. CERN is the host of many particle accelerators including the Large Hadron Collider (LHC), the world's largest and highest-energy particle collider [4]. At the LHC, there are four larger experiments, but this thesis focuses on the ALICE (A Large Ion Collider Experiment) experiment. ALICE focuses on the Quantum Chromo-Dynamics (QCD), the strong interaction sector of the Standard Model. Besides studying the collisions between lead (Pb) nuclei, ALICE also studies collisions with lighter nuclei (e.g. Xe - Xe), proton-proton (pp or p-p) and dedicated proton-nucleus runs. The ALICE detector is 26 m long, 16 m wide and 16 m high with a total weight of approximately 10,000 t and consists of 18 detector subsystems with their own specific technology and design constraints [5].

The part of the detector that is the closest to the beampipe is called the Inner Tracking System (ITS) and is located in the central barrel of ALICE. The ITS is used for the reconstruction of the event vertex produced in the collision, and for tracking and identifying low-momentum particles. The ITS has been upgraded during the Long Shutdown 2 (2019-2021) in order to improve reconstruction efficiency and precision. The original ITS consisted of six layers of different silicon detector technologies, while in ITS2 another cylindrical layer was added and the detector now consists of seven layers of monolithic active pixel sensors (MAPS) making it possible to reconstruct tracks based on ITS information alone [6].

Currently, there is a new and recently approved upgrade that is called ITS3 and is planned to be installed during Long Shutdown 3 (2026-2028)[1], to replace the innermost three layers of the current detector [7]. This Master's Thesis studies the detection effi-

[1] According to the plan at the time of the writing of this thesis. Subject to change.

ciency and spatial resolution, as well as other characteristics, of the first ITS3 prototypes. The prototypes tested are the MOSS (MOnolithic Stitched Sensor) and the related, so-called, babyMOSS, which is a smaller version of the MOSS that was created in order to simplify the testing procedure. This was also the first ever detector prototype that was built using silicon stitching technology, and thus the results are very important for further studies and the preparation of the final ITS3 detector.

The new ITS3 detector will have a material budget for the inner layers of only 0.05% X_0 in each layer, with the innermost layer positioned at only 19 mm radial distance from the interaction point, reducing the scattering of the examined particles. A traditional Si tracking detector would typically have a thickness of 1-2% X_0 per layer, or be 20-40 times thicker in terms of material budget. The detector consists of silicon, but it is going to be thin enough to be bent around the axis of the beam. That fact, together with the stitching technology, will lead to a self-supportive detector, that has very little need for supporting material. This thinness will result in a large improvement of the tracking precision and efficiency at low transverse momentum with ITS3. Another outcome of this is the significant advancement in the measurement of low momentum charmed hadrons and low-mass dielectrons in heavy-ion collisions at the LHC [7].

The prototypes studied here are not bent, since the first part of testing this new idea was to find the detection efficiency and spatial resolution of this very thin detector. The bending has been studied in earlier beam tests with non-stitched sensors, therefore meaning that the efficiency of the bent sensors is already measured. It is important that both the efficiency and spatial resolution are improved compared to the already known values for ITS2. Thus this report focuses on the components of the system that were necessary to conduct the tests with beam, as well as the results of these tests.

Chapter 2

2 Theoretical and experimental background

2.1 The Standard Model

The Standard Model is the theory that describes how the fundamental particles interact via three of the four fundamental forces. This means that the model describes the strong, weak and electromagnetic interaction but does not include gravity [1]. The currently known information on the fundamental particles and forces are schematically summarized in Figure 1 [8].

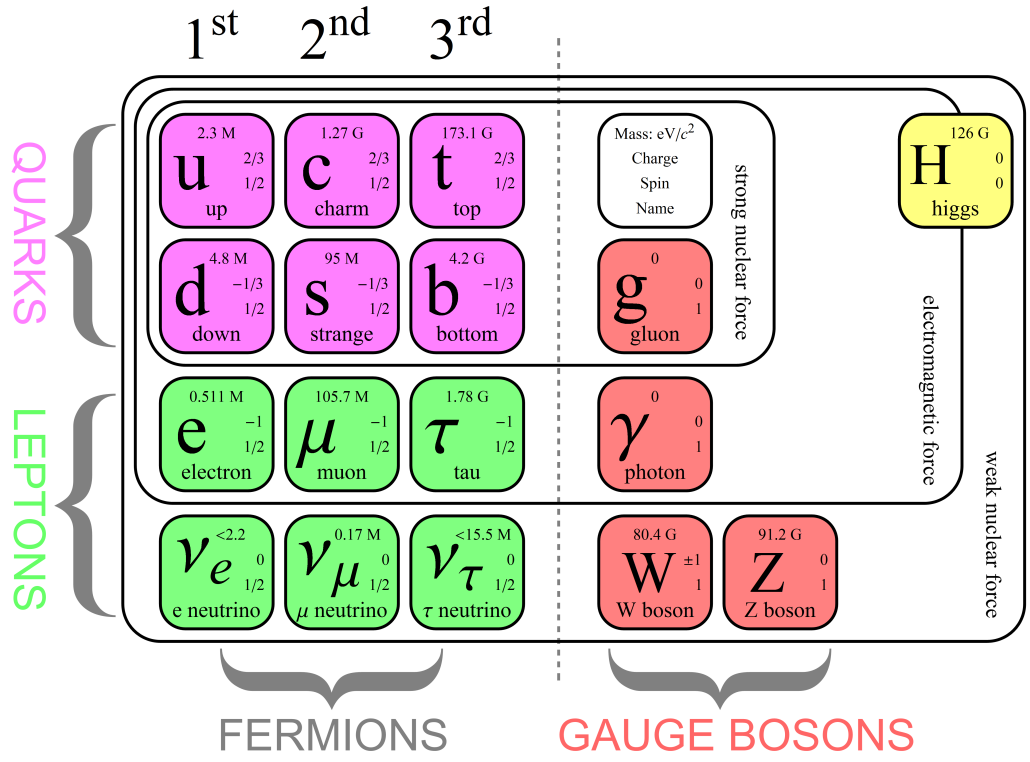

Figure 1. A schematic representation of the Standard Model including all the fundamental particles and fundamental forces. Picture obtained from Ref. [8].

The first way to categorize the particles is by their spin numbers. There are particles with integer spins that are called bosons and particles with half-integer spins, the fermions. A very important difference between them is that fermions must abide the Pauli Exclusion Principle, which says that there are not two particles in the same system that can occupy the same quantum state. This leads to differences in quantum statistic calculations. Thus, bosons follow the Bose-Einstein statistics, while fermions the Fermi-Dirac statistics [9]. In the Standard Model there are twelve fermions and twelve anti-fermions, and five bosons, γ, g, Z, W^+, W^-.

After the particles are characterized as fermions, they can be further distinguished as leptons or quarks that carry a color charge (red, blue or green). Leptons are color-free and interact only by the weak or electromagnetic force. In terms of electric charge e,

there are two kinds of leptons. The charged leptons (e, μ, τ) have a charge of -1, while the neutral called neutrinos, have no charge. The anti-particles carry the opposite charge and quantum numbers, but they have the same mass. There are six quarks, three up-like quarks (u, c, t) with charge +2/3 e and three down-like quarks (d, s, b) with charge -1/3 e, divided in three generations, and with the corresponding anti-particles.

Quark interactions are described by a theory called Quantum ChromoDynamics (QCD) and the so-called color confinement. The theory stipulates that isolated free quarks cannot be observed. Two or three quarks create hadrons by interacting with the strong force to form color-neutral states. These states can either be baryons, which consist of three quarks (qqq) or three anti-quarks ($\bar{q}\bar{q}\bar{q}$), thus with half-integer spin (fermions), or mesons with integer spin (bosons) that are bound states of a quark with an anti-quark ($q\bar{q}$). The quarks that are forming a baryon have different colors leading to a color-neutral baryon, while in mesons, the quark has a color charge and the anti-quark the corresponding anti-color charge [10]. Figure 2 shows how the mesons and baryons are connected to the Bose-Einstein and Fermi-Dirac statistics, respectively [11].

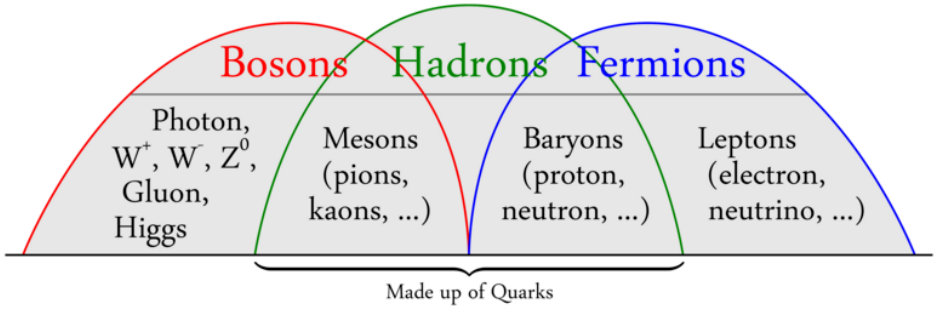

Figure 2. A schematic representation of the Standard Model particles and how composite particles are categorized in bosons and fermions. Picture obtained from Ref. [11].

Last but not least, the Standard Model includes the particles that are force carriers. These are the photon (γ), the gluon (g), the Z^0 boson and the $W^{\pm}$ boson. The photon is responsible for the electromagnetic force, while the Z and W bosons are the force carriers for the weak force with both them and the photons being able to interact with all fermions. On the other hand, gluons are the force carriers of the strong force, have no mass and no electric charge, but are bosons with a color and an anti-color charge. This combined with the fact that quarks have a color charge is what makes the quarks able to interact with gluons, and thus the strong force [10]. It is interesting to note that the photon, which is the force carrier for the electromagnetic force, has no electromagnetic charge, while the gluon, the carrier of the strong force, has a color charge.

Another particle predicted by the Standard Model, is the Higgs boson, which was observed in 2012 and is associated with the Higgs field. This was a breakthrough in particle physics, because this is the particle that gives mass to the fundamental particles. This is a result of a breaking of the symmetry in the Higgs field, meaning that it has a non-zero value (or vacuum expectation) everywhere. Although this was a very important discovery and needs to be addressed when describing the Standard Model, the ALICE experiment does not focus on the study of the Higgs.

2.2 Quark Gluon Plasma

Shortly after the Big Bang, the universe was filled with a remarkably hot and dense state of matter made of all kinds of fundamental particles moving at nearly the speed of light. This state of matter was dominated by quarks and gluons and in those first moments of extreme temperature they were not yet bound into hadrons but rather free to move on their own in what's called a Quark-Gluon Plasma (QGP). The powerful accelerators at CERN make direct collisions between massive ions, such as lead nuclei to recreate these extreme conditions. During these heavy-ion collisions the hundreds of protons and neutrons within two such nuclei collide with energies exceeding a few trillion electronvolts each. This forms a very hot "fireball" in which everything "melts" into a quark-gluon plasma. Subsequently, this fireball expands and cools quickly, and the quarks and gluons (or all-together called partons) reassemble into ordinary hadronic matter that disperses in all directions. An important discovery was that the quark-gluon plasma exhibits behavior more akin to that of a perfect fluid with small viscosity rather than of a gas, which had been expected by many researchers [12].

The conditions under which the QGP is created, are only present for a short time during and after the collision, thus making it impossible to directly study the QGP. In order to study the QGP, one needs to study its effects, such as strangeness enhancement, which indicates that in high-energy nucleus-nucleus collisions, an enhanced production of strange hadrons is observed [13]. Another effect is the collective flow which describes the movement of a large number of ejectiles either in a common direction or at a common magnitude of velocities [14]. It is important to note that in these nucleus-nucleus collisions at LHC, thousands of particles will be produced in single collisions, and they need to be individually tracked and identified.

2.3 Multiple scattering and material budget

Scattering in physics refers to the collision of particles, which result in a change in the direction of motion of one or all of the particles. The collision can happen between two particles that repel each other, e.g. two positive or two negative particles, and the force between these particles follows Coulomb's law [15]. We can define three types of scattering, depending on the number of particles interacting. Single scattering is when the particle interacts with a single target particle, meaning that the thickness of the material is exceptionally small. When the number of Coulomb scattering rises but remains below a few tens of interactions, then the scattering is characterized as plural. In a case of a real detector as the ALICE detector, the material thickness increases, leading to so-called multiple scattering (many interactions) and in this case the angular dispersion can be modelled as Gaussian [16].

When a particle travels through a thicker material it scatters multiple times with particles of the material, thus making it more difficult to reconstruct the initial trajectory of the particle. In a particle detector, it is very important to be able to know the trajectory of the observed particle, in order to identify the particle and determine its properties. It is therefore preferable that a tracking detector consists of as little material as possible. In order to quantify the material thickness, one uses the radiation length - X_0. The radiation length of a material is the mean length, measured in cm, to reduce an electron's energy by a factor of 1/e [17]. The material budget (X/X_0), is referred to in terms of the radiation length. For example, the current Inner Tracking System of ALICE has a material budget

per layer of 0.3% X_0 for the inner layers [18], while other inner tracking systems in high-energy physics experiments often have a thickness of 1-2% X_0 per layer.

2.4 Bethe-Bloch formula: mean energy loss

Ionization energy losses play a crucial role for all charged particles, overshadowing radiation energy losses at all energy levels except the highest attainable ones, particularly for particles other than electrons and positrons. In the 1930s, Bethe, Bloch and others, described such losses mainly as a result of Coulomb scattering. The resulting Bethe-Bloch formula [10] for spin 0 bosons with a ± q charge (in terms of electrons), mass M and velocity υ, is:

$$-\frac{dE}{dx} = \frac{Dq^2 n_e}{\beta^2}[\ln(\frac{2m_e c^2 \beta^2 \gamma^2}{I}) - \beta^2 - \frac{\delta(\gamma)}{2}] \tag{2.1}$$

where x is the distance travelled through the medium, $\beta = \upsilon/c$, $\gamma = (1-\beta^2)^{-1/2}$ the Lorentz factor, m_e is the electron mass, h the Planck constant, α the fine structure constant and

$$D = \frac{4\pi\alpha^2 h^2}{m_e} = 5.1 \times 10^{-25}\text{MeVcm}^2 \tag{2.2}$$

The other constants are the properties of the medium with n_e the electron density, I the ionization potential and δ is a dielectric screening correction, for highly relativistic particles. The most important take-aways from this formula is that $\frac{dE}{dx}$ is proportional to q^2, and inversely proportional to β^2. These are key for particle identification.

2.5 Large Hadron Collider

The world's largest and most powerful accelerator is located at the European Organization for Nuclear Research (CERN), on the border between Switzerland and France and is called the Large Hadron Collider (LHC). It first started in 2008, and it comprises a 27-kilometer ring of superconducting magnets with accelerating structures that are used to increase the energy of the particles. Inside the ring, two high-energy beams, such as proton or heavy-nuclei beams, travel with speeds close to the speed of light, in opposite directions, in ultra-high vacuum and temperatures lower than in the outer space. The superconducting magnets are used to guide the beams with their strong magnetic field, without energy loss or resistance [4].

LHC is CERN's latest addition in the accelerator complex that consists of nine different accelerators. In order for the particles to gain enough momentum in stages, the Proton Synchrotron (PS) accelerator injects particles (with a momentum up to 26 GeV/c) in the Super Proton Synchrotron (SPS) accelerator (momentum up to 450 GeV/c) that later injects them in the LHC. Other than that, PS and SPS are also used for experiments and test beams. Figure 3 shows a schematic overview of the LHC [19].

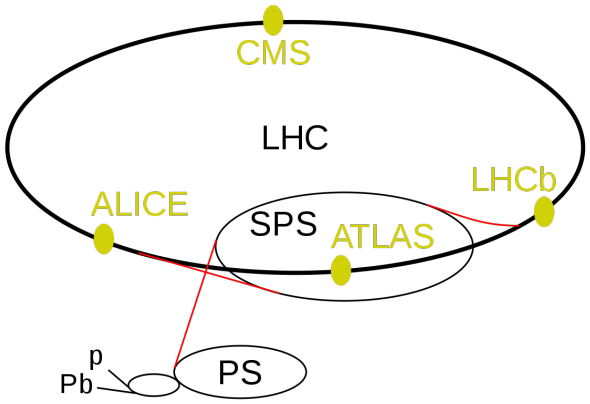

Figure 3. Overview of the LHC with its four main experiments and the two injectors PS and SPS. Picture from Ref. [19].

The LHC has four major experiments. ATLAS (A Toroidal LHC ApparatuS) and CMS (Compact Muon Solenoid), are more general experiments, investigating particles like the Higgs boson, which they discovered in 2012, and physics Beyond the Standard Model. LHCb (Large Hadron Collider beauty), focuses on matter and anti-matter physics and the bottom (or beauty) quark. Finally, ALICE (A Large Ion Collider Experiment), primarily studies heavy-ion physics and the QGP, as mentioned above. LHC takes proton-proton (pp) collision data for approximately seven months per year and one month of Pb-Pb collisions. The experiment, in addition to taking pp and Pb-Pb data, also takes some cosmic data throughout the seven-month period [20].

2.6 Common variables

The different detectors at the LHC, define their common variables following the needs and orientation of each experiment. The following subsections, focus on the ALICE experiment.

2.6.1 Coordinate system definition

The ALICE coordinate system is a right-handed orthogonal Cartesian system and is defined as follows [21]:

- x - *axis*: It is pointing towards the center of the LHC, aligned with the local horizontal plane and orthogonal to the beam direction.
- y - *axis*: pointing upwards and perpendicular to both the x - *axis* and the mean beam direction.
- z - *axis*: parallel to the beam direction.
- *azimuthal angle* ϕ: increases from the x - *axis* to the y - *axis*, from 0 to $\pi/2$.
- *polar angle* θ: increases from the z - *axis*, where it is 0, towards the x,y - *plane*, where it is $\pi/2$ and finally towards -z, where it takes the value π.

The point of origin of the system at the interaction point (IP) is *x, y, z = 0*. The conversion from spherical to Cartesian coordinates is thus given by:

$$\begin{aligned} x &= r\sin\theta\cos\phi \\ y &= r\sin\theta\sin\phi \\ z &= r\cos\theta \end{aligned} \tag{2.3}$$

2.6.2 Transverse momentum

For most experiments the transverse momentum is defined as

$$p_T = \sqrt{p_x^2 + p_y^2} \tag{2.4}$$

where the beam axis is along the z - axis. In the ALICE experiment, a particle's momentum is determined from its azimuthal bend ϕ within the xy-plane. Particles within the colliding beams by the interaction point in the center of ALICE, exclusively possess momentum in the z-direction, resulting in zero transverse momentum (note that this is true e.g. for protons but not the partons like quarks and gluons inside the protons). This characteristic is among the reasons why the observable p_T is frequently employed in data analysis.

2.6.3 Rapidity and pseudorapidity

As mentioned above, the particles inside the LHC are travelling at speeds close to the speed of light, thus meaning they have to be treated as relativistic particles. Note that the units used below are natural units, where the speed of light is considered to be equal to 1. Rapidity [22] is a useful variable at high energies because it is additive between different Lorentz frames and is given by

$$y = \ln\frac{E + p_z}{E - p_z} = \operatorname{arctanh}\beta_z \tag{2.5}$$

where p_z and β_z are the momentum and velocity of the relativistic particle, in the beam direction, respectively, and E is its energy, calculated by the mass (m) and the total momentum ($\mathbf{p}$) of it and given by the formula

$$E = \sqrt{\mathbf{p}^2 + m^2} \tag{2.6}$$

Since it is complicated to measure (correctly identify) the mass, momentum and velocity of all the particles produced in high-energy collisions, due to the fact that the particles are highly relativistic, the following approximation can be done

$$E \approx |\mathbf{p}|, \quad for \quad m << |\mathbf{p}| \tag{2.7}$$

This approximation leads to the variable pseudorapidity (η), which is equivalent to the rapidity for massless particles. η depends only on the polar angle θ and is given by the formula

$$\eta = \frac{1}{2}\ln\frac{|\mathbf{p}| + p_z}{|\mathbf{p}| - p_z} = -\ln\tan\frac{\theta}{2} \tag{2.8}$$

Chapter 3

3 A Large Ion Collider Experiment

The ALICE experiment schematically shown in Figure 4, is located in Saint-Genis-Pouilly in France, is one of the four main experiments at the LHC and focuses on heavy-ion physics, by investigating the QGP and the properties of deconfinment in QCD. The experiment consists of several different detector components that focus on different tasks, as particle tracking or particle identification.

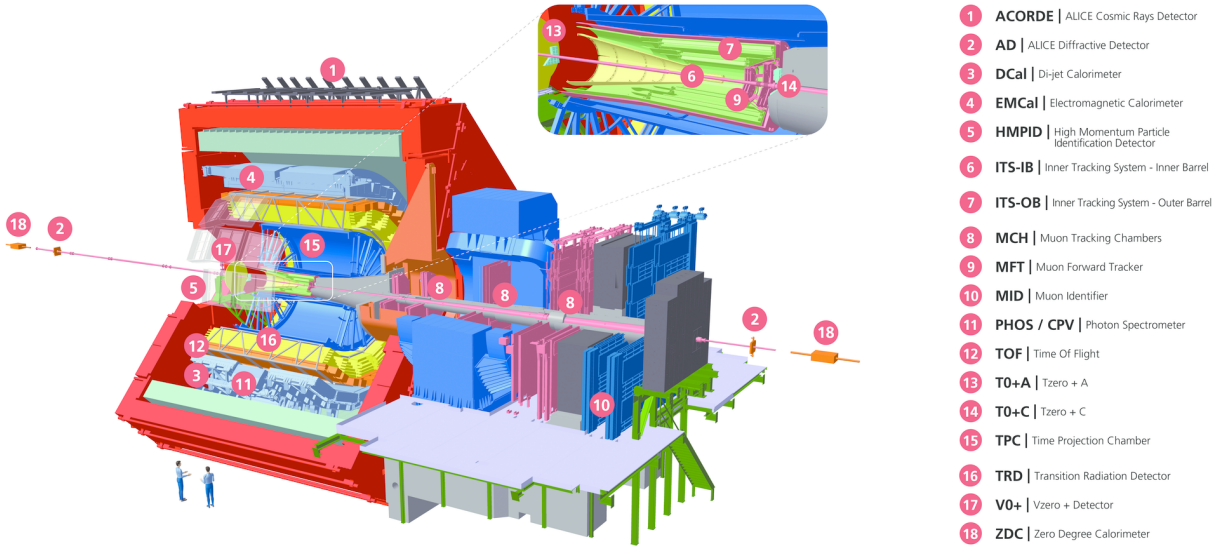

Figure 4. Illustration of the ALICE experiment with all the basic components, as it is currently after the second upgrade. Picture from Ref. [23].

The detector closest to the beam-pipe is the Inner Tracking System (ITS) and is in charge of the reconstruction of primary and secondary vertices from decays of produced particles. Following the ITS in the radial direction, the main tracking detector of ALICE is the Time Projection Chamber (TPC). After the TPC, the Transition Radiation Detector (TRD) is responsible for the electron identification and is followed by the Time-Of-Flight detector (TOF), which is responsible for identifying particles with momentum up to a few GeV/c. There are also several detectors that have limited azimuthal acceptance compared to the ITS-TPC-TRD-TOF detectors. These are: a Cherenkov detector (HMPID - High Momentum Particle Identification Detector), which provides additional particle identification information for high momentum particles, a homogeneous photon spectrometer (PHOS - PHOton Spectrometer), and a sampling electromagnetic calorimeter (EMCAL). A Photon Multiplicity Detector (PMD) and a muon spectrometer (MUON) are positioned at forward rapidities [24]. The detector system of most interest for this thesis is the Inner Tracking System and its upgrades (ITS2, ITS3).

3.1 Inner Tracking System

The initial ITS consisted of six cylindrical layers of silicon detectors placed coaxially around the beam pipe, placed at radii between 39 mm and 430 mm, with a material budget of approximately $1\%X_0$ for each layer [25]. There were three types of Silicon (Si) sensors, where the two innermost layers consisted of Silicon Pixel Detectors (SPD), to deal with the requirement for position resolution of primary and secondary vertices. The next two layers were Silicon Drift Detectors (SDD), which have a good multitrack reconstruction capability. The outer pair consisted of Silicon Strip Detectors (SSD) [24]. The inner radius was the minimum allowed by the radius of the beam pipe, while the outer radius was set by the requirement to match tracks with those from the TPC. The first layer had more extended pseudo-rapidity coverage and together with the Forward Multiplicity Detectors (FMD) provided continuous coverage for the measurement of charged particle multiplicity [25].

This ITS detector had limited read-out rate capabilities because it could run at a maximum rate of 1 kHz, irrespective of the detector occupancy. This rate limitation was acceptable for LHC Run 1 (2009-2013) but problematic towards the end of LHC Run 2 (2015-2018), since it restricted the ALICE experiment to use only a small portion of the full Pb–Pb collision rate of 8 kHz that the LHC could provide. The collection of required reference data in pp collisions was also prevented. The initial ITS was also impossible to access during the yearly maintenance period (YETS), and was removed and replaced during Long Shutdown 2, as described in the next section [25].

3.2 ITS2: Upgrade of ITS during Long Shutdown 2 (2019-2022)

The current form of the Inner Tracking System, shown in Figure 5, is called ITS2 and is a two-barrel structure. The Inner Barrel (IB), formed with layers 0 to 2 (also called Inner Layers) and the Outer Barrel (OB), formed by layers 3 to 6. Layers 3 and 4 are also called Middle Layers, while 5 and 6 are also called Outer Layers [26]. The layers are azimuthally segmented in mechanical independent units called Staves, which extend in the whole length of the layer.

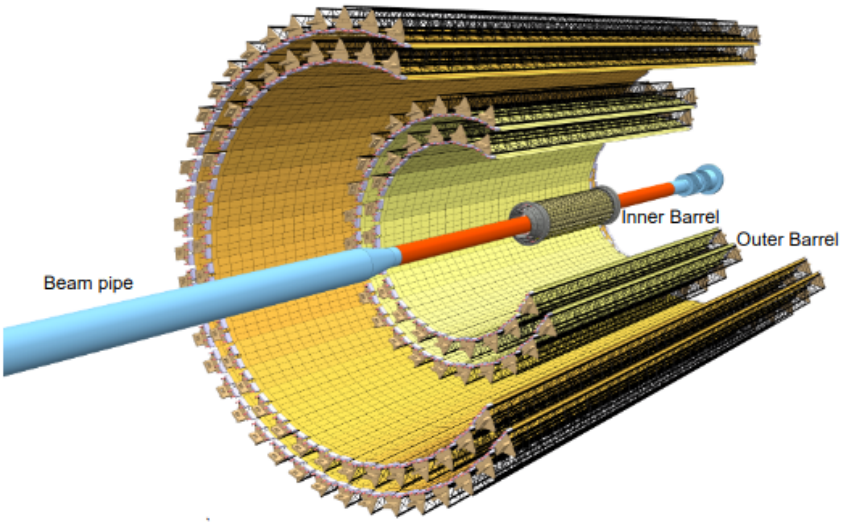

Figure 5. Illustration of ITS2 with its staves forming a cylinder. Picture from Ref. [25].

The Inner Layers have a sensitive area length of 271 mm, the Middle Layers of 843 mm and the Outer Layers, almost double, of 1475 mm. Staves form a half barrel by being fixed in a half-wheel shaped support structure. Mounted on the Staves, are the ALPIDE chips (ALice PIxel Detector), which consist of Monolithic Active Pixel Sensors (MAPS), which are going to be further discussed in Chapter 4. ALICE is the first LHC experiment that uses MAPS detector technology on a large scale.

Staves consist of the following main components and are illustrated in Figure 6 [25]:

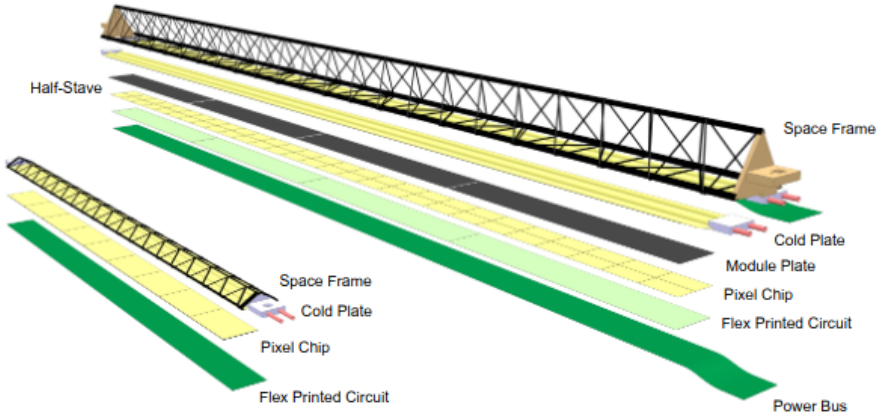

Figure 6. Schematic illustration of the Staves for the Inner Barrel (left) and the Outer Barrel (right), including their main components. Picture from Ref. [25].

- **Space Frame:** Lightweight mechanical support structure for a single stave based on carbon fiber.
- **Cold Plate:** Cooling pipes covered by a carbon material.
- **Hybrid Integrated Circuit (HIC):** It consists of a polyimide Flexible Printed Circuit (FPC) on which the Pixel Chips (2×7) and some passive components are bonded.
- **Half-Stave:** For the Outer Barrel, the Stave is further segmented azimuthally into two halves.
- **Module:** The Staves of the Outer Barrel are further segmented longitudinally to Modules. Each Module consists of a Hybrid Integrated Circuit that is glued onto a carbon plate (Module Plate). Each Half-Stave consists of a number of modules (four for the Middle Layers and seven for the Outer Layers) glued on a common cooling unit.

The main ITS2 design goals were to reduce the material budget and to have measurements closer to the collision point to improve the track pointing resolution (distance of closest approach) by a factor of three in the transverse plane and by a factor of five along the beam axis [6]. Figure 7 shows the material budget of Layer 0 in the IB. The highest peaks correlate with the overlap of the structures along the edges of the Space Frame, ensuring the essential stiffness, while the narrow spikes align with reinforcing the upper vertex. The peaks around 0.5% X_0 are due to the polyimide cooling pipes inside the Cold Plate. The average value (0.35% X_0) is of great importance for the ITS2 performance. The material budget in the Outer Barrel is approximately 0.8% X_0 per layer [26].

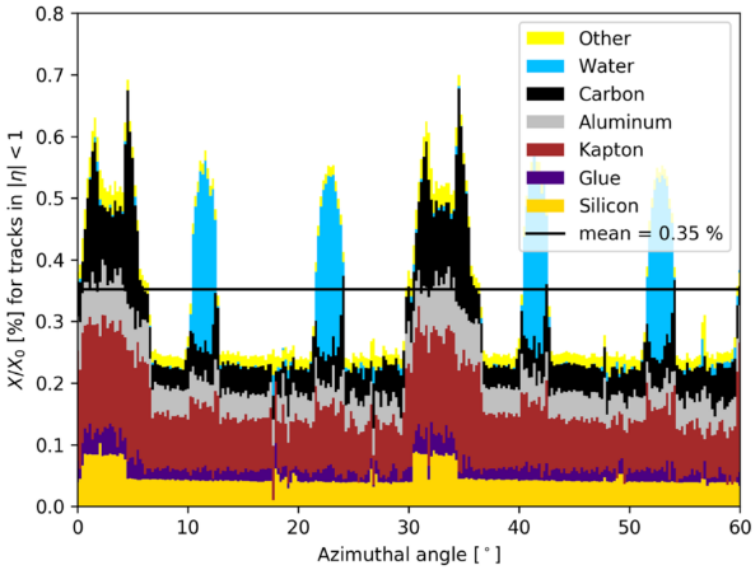

Figure 7. Material budget of Layer 0 of ITS2, averaged over $|\eta| < 1$. Picture from Ref. [26].

A further improvement of the material budget is proposed for the ITS3, as will be explained later on.

3.2.1 ALPIDE

ALPIDE is the Pixel Chip developed by a collaboration formed by CCNU (Wuhan, China), CERN, INFN (Italy), and Yonsei (South Korea) and the technology chosen is TowerJazz's 180 nm CMOS Imaging Process[2]. It comprises a unique low-power in-pixel discriminator circuit, which operates an asynchronous address encoder circuit, with the address encoder located within the memory matrix itself. The circuitry inside each pixel features amplification, shaping, discrimination and multi-event buffering. The pixel's signal digitization eliminates the necessity for an analog column driver, resulting in a substantial reduction in power consumption and enabling rapid read-out (read-out rate of up to 100 kHz for Pb–Pb collisions and 400 kHz for p-p collisions for ITS2) [25, 26].

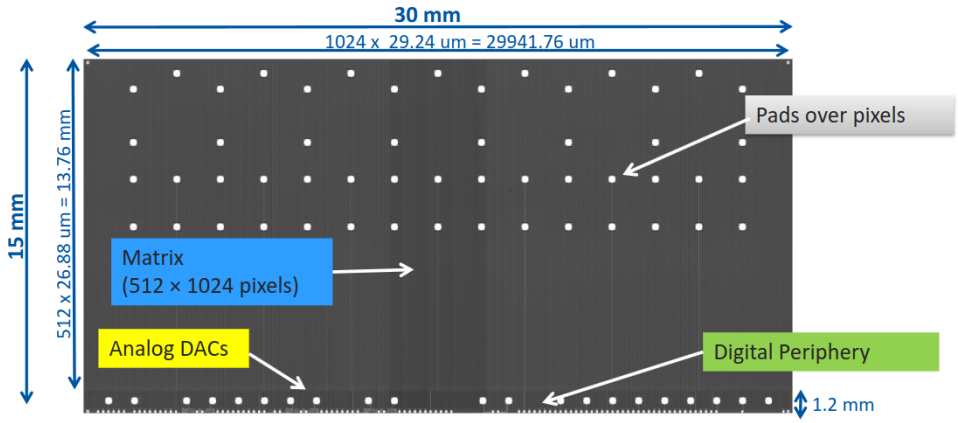

Figure 8. Representation of the inside of the ALPIDE, obtained from Ref. [27].

[2]www.jazzsemi.com

The ALPIDE chip comprises roughly 5×10^5 pixels with a size of 26.88 μm $\times$ 29.24 μm, ordered in 512 rows and 1024 columns, for a total area of 30 mm $\times$ 15 mm, as shown in Figure 8. The fact that the ALPIDE has such small dimensions brings up some problems regarding the way that the detector is built forming a cylinder. The total chip power consumption is 180 mW, which is analogous to a power density of about 40 mWcm^{-2}. The majority of this power, approximately 150 mW, is distributed by the digital interface circuitry and the high-speed output data links used for the read-out. These components are situated in a confined space measuring around 30 mm $\times$ 1.5 mm, positioned near one edge of the chip. Only a sixth of the total power is freed within the pixel matrix, leading in a power density of about 7 mWcm^{-2}. This falls comfortably within the range where air cooling proves to be a practical and efficient solution but brought up the question if there could be a pixel sensor digital periphery at the edge of the detector [26].

The ALPIDE chip needed to fulfill some specifications. The Fake-Hit Rate (FHR), for the IB and OB needed to be $< 10^{-6}$ in pixel^{-1}event^{-1}. For the ALPIDE it is $\approx 10^{-8}$ pixel^{-1}event^{-1}, the detection efficiency is higher than 99% for a wide range of threshold settings, while the spatial resolution for the ALPIDE is around 5 μm. The requirement of spatial resolution for the IB was 5 μm, while for the OB it was 10 μm [28].

3.2.2 Particle detection with ITS2 MAPS

As depicted in Figure 9, when a charged particle crosses through the active volume of the silicon sensor, it releases charge carriers (electrons and holes) within the semiconductor material. Electrodes then collect the liberated charge, revealing not only the presence of a particle but also its impact point on the sensor, because of the fine segmentation. The characteristics and quantitative behavior of the charge collection process rely on material properties (such as resistivity or doping level/profile), geometry (including the thickness of the sensitive material, pixel pitch, and electrode shape), and the electric field configuration (in terms of electrode potential and geometry) of the sensor. The quantity of deposited charge varies depending on the particle's type and momentum (Bethe-Bloch equation 2.1).

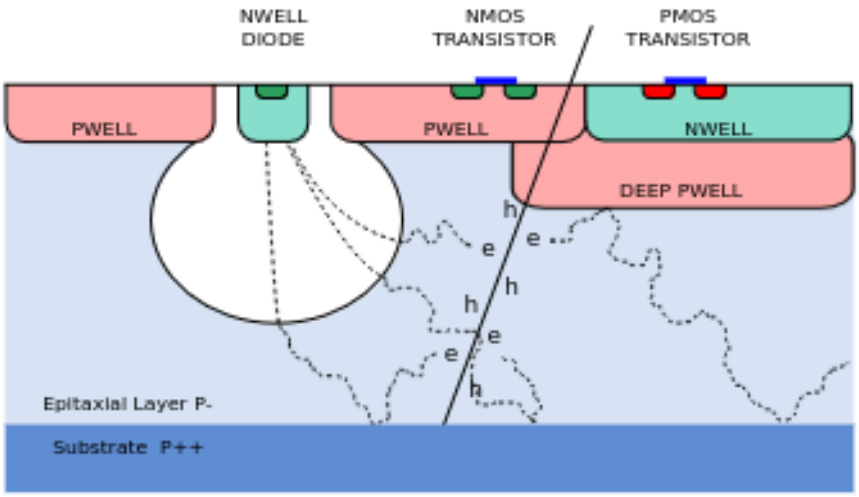

Figure 9. Schematic representation of a pixel in the TowerJazz 0.18 µm imaging CMOS with the deep p-well feature. Picture from Ref. [25].

Minimum Ionizing Particles (MIPs), like 0.5 GeV/c pions that set the minimum detectable charge requirement, commonly release around 60 electrons per 1 µm path length in thin silicon layers. The ITS2 is about 50 μm thick, leading to about 3000 liberated electrons for a MIP [25]. The signal from the collected electrons is compared with a threshold, and a yes/no pixel-fired information is given for each pixel. Only pixels with a collected signal above the threshold are reported (zero-suppressed information).

The complicated mechanical structure of ITS2 together with the rather small material contribution from the Si detector material itself, resulted in the proposal of the new ITS3 detector, that also uses MAPS, but reduces the total material budget considerably.

3.3 Proposal for ITS3

ALICE is preparing for the new ITS upgrade, called ITS3, which will take place in the next Long Shutdown 3 (LS3, 2026-2028), and that will replace the three innermost layers of the current ITS2, with minimal mechanical support. It is a new vertex detector that consists of three cylindrical layers based on curved wafer-scale stitched sensors, featuring a material budget of only 0.05% X_0 per layer, with the first layer positioned at a radial distance from the interaction point of only 19 mm. The new material budget for Layer 0 is shown in Figure 10 and can be compared to the one of ITS2 in Figure 7.

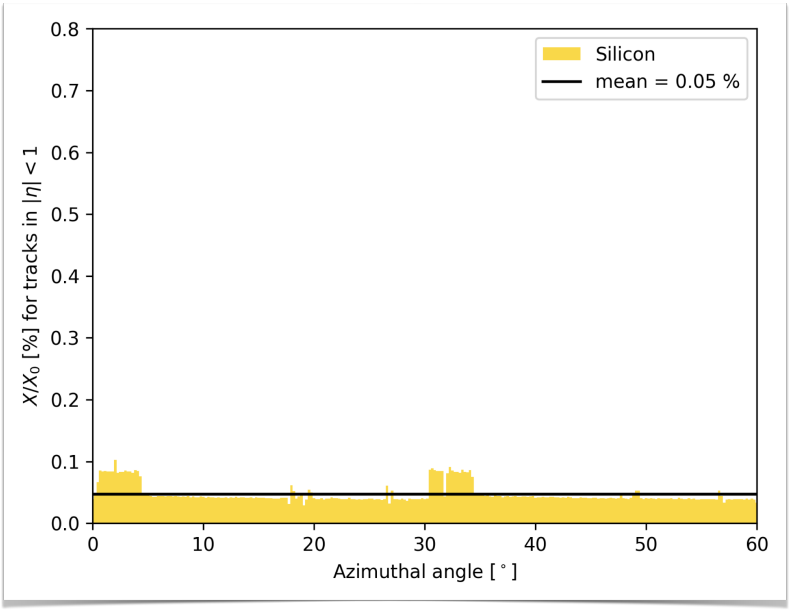

Figure 10. Material budget of Layer 0 in ITS2, averaged over $|\eta| < 1$. Picture from Ref. [29].

This detector is based on the new feature of CMOS imaging sensor technologies, called *stitching*, that will allow a new larger area of single MAPS detectors with a combined area of 14 cm × 14 cm and it will change the current 180 nm technology to TPSCo 65 nm technology. Along with the upgrade of ITS3, there will be a new beam-pipe installed with smaller radius (16 mm) and thickness (500 μm). The first layer of this ITS3 is going to be closer to the interaction point and with six times less material budget, thus improving the tracking precision and efficiency in the low transverse momentum region. The read-out rate is going to be the same as for ITS2 [30].

While the OB will stay the same as in ITS2, the IB will be completely renewed. It will consist of two halves, named half-barrels, that will allow the detector to be mounted

along the beam-pipe. Each half-barrel will be composed by three half-layers that are set out inside the half-barrel as shown in Figure 11.

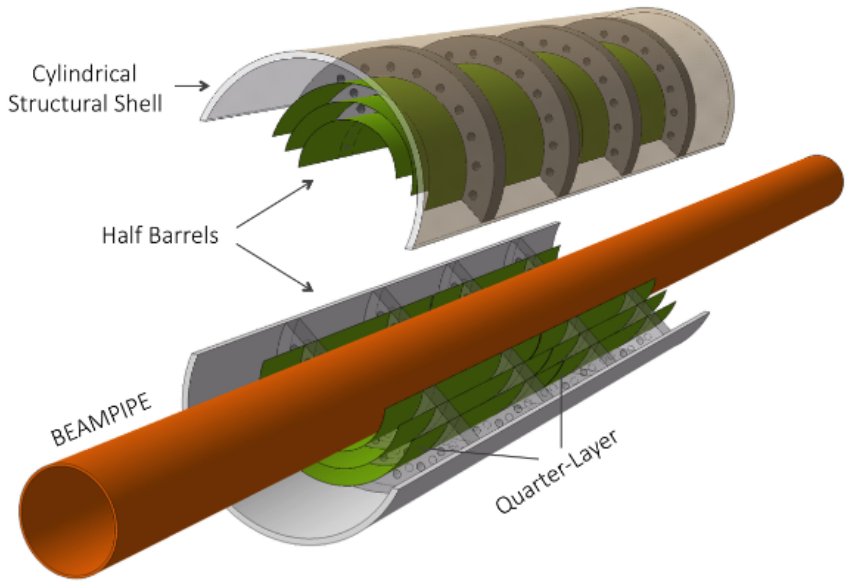

Figure 11. Representation of the Inner Barrel of ITS3 including the half-barrels, obtained from Ref. [30].

The half-barrels will have a half-cylindrical shape, with each half-layer segmented at z = 0 (longitudinally) in two halves, the quarter-layers. Every quarter-layer contains a single large pixel chip (stitched), which is bent to a cylindrical shape and its periphery and interface pads are all located on one edge. This edge is where the chip is attached to a flexible printed circuit, about 5 mm in length, facilitating electrical connections via aluminum wedge wire bonding. The flexible printed circuit employs polyimide as the dielectric and aluminum as the conductor. Extending lengthwise from the chip's edge through the End-Wheel, it ultimately reaches a patch panel a few centimeters away. At this point, interconnections to the electrical data cables and power cables are established [30].

The End-Wheels and the outer CYlindrical Structural Shell (CYSS), depicted in Figure 12, are the key structural components of the new IB. The End-Wheels are connected to the CYSS, that provides the support of the three layers. Constructed from Carbon Fiber Reinforced Plastic (CFRP) materials, both the End-Wheels and CYSS feature lightweight half-wheel spacers made of open cell carbon foam, strategically inserted between layers to define their radial positions. These half-wheel spacers facilitate the connection of the half-layers to the outer CYSS and to each other, starting from Layer 2 [30].

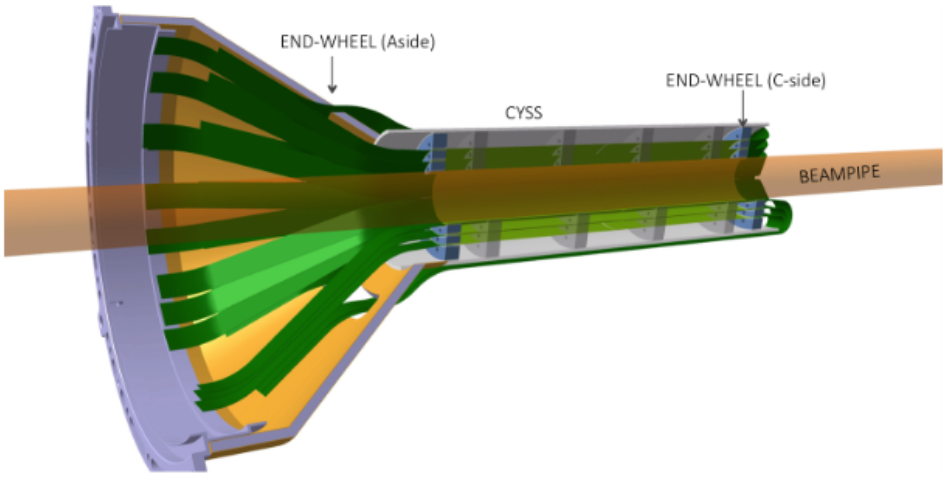

Figure 12. The Inner Barrel of ITS3 including a side-view of the End-Wheels and CYSS. The cables exit from the C-side of the End-Wheel, are folded back to the outside of the CYSS and then led to the A-side. Picture from Ref. [30].

Chapter 4

4 ITS3: Detector information

The project focuses on the function of the new detector and more specifically on the first prototypes created and used in 2023-2024 test beams. Thus, it is important to understand the hardware of these detectors.

4.1 Pixel Detectors

A pixel detector (PIcture ELement - PIXEL) is a device that can detect an image and the size of the pixel represents the granularity of the picture. Particle physics requires detectors that can study short-lived particles, as well as handle high interaction rates and energies. These detectors should also have certain values for the material thickness, read-out speed and radiation hardness [31], which led to the use of pixel detectors in particle physics. The pixel detectors were implemented in the 1980s, with the sensors being based on silicon (Si) semiconductor technology and of the read-out electronics CMOS technology (application-specific integrated circuits, ASICs) [25]. There are two important pixel detector categories, the Hybrid Pixel Detectors and the CMOS Monolithic Active Pixel Sensors (MAPS).

4.1.1 Hybrid Pixel Detectors

Hybrid PIxel Detectors are made of two parts, as indicated by the name hybrid. They consist of a pixel sensor, which is a silicon diode organized in pixel cells, and from one or more readout chips with the same cell pattern, both connected in each pixel by a conducting microconnection called bump bond. These detectors are fast and able to detect particles with high energies and electromagnetic radiation [32]. According to Ref. [32], the LHC has particle fluxes of the order of 10^{11} particles per second that travel by the tracker volume and for a luminosity of 10^{34} $\mathrm{cm}^{-2}\mathrm{s}^{-1}$ about 1200 particles pass the tracking detector, with a 25 ns beam crossing occurrence. The occupation density or occupancy, is high close to the interaction point, so many independent detector layers are needed for the reconstruction, thus making pixel detectors the best suited instrument due to the small sizes of the pixels [32]. Note that these numbers are true for the ATLAS and CMS, but the luminosity in ALICE is several orders of magnitude less (approximately 3 to 4) than that of the other experiments, thus detectors with lower read-out rate are appropriate.

The fact that the detector has different components for the sensor and read-out makes it possible to optimise both components separately. These complex entities have development times of several years and high costs of production, but the already developed readout chips can be used with different sensor types, due to their hybrid design. However, the expensive cost of building these detectors, as well as the large material thickness that is needed to reliably mate the two parts, together with the thickness of the support and cooling structures, led scientists to further investigate the Monolithic Pixel Sensors [32].

4.1.2 CMOS Monolithic Active Pixel Sensors - MAPS

In the early 1990s, the concept of pixel sensors and electronic circuitry forming one entity was proposed, so CMOS technology lines were used to create the Monolithic Active Pixel Sensors (MAPS). Usually, low cost and low ohmic substrate wafers are used, where an epitaxial layer is grown on the wafer. The doping profile on that layer, as well as the conduction type, can be controlled regardless of the substrate, and they can be chemically cleaned and constructed with higher resistivity compared to the substrate. As shown in Figure 9, when particles are travelling through the epitaxial layer, electrons can appear in small parts by drift in the depleted region, or primarily via diffusion towards a collection electrode, in the n^+ well. The absence of a directional drift field in the epitaxial layer, leads to incompleteness and slower charge collection mainly occurring by the undirected diffusion. The deposited charge is thus very small, which means that low noise of the readout electronics is needed, in order to achieve reasonable Signal to Noise Ratio (SNR) values [32].

Underneath the n well, there is a highly doped deep p well implanted, that shields the n well from becoming a competing collection node with other n wells. The low ohmic substrate is not contacted and thus the p-doped region has a negative potential relative to the collecting node, which in turn leads to a repulsive effect. That allows the pixel detector to have less material budget because the total thickness of the device can be reduced [32, 33]. The typical read-out for in-pixel circuits in MAPS is called three-transistor readout (3T readout). For the ALICE upgrade, MAPS using charge and voltage amplification and dedicated readout systems are successfully used [32]. For the new ITS3 (as well as the ITS2), the most important information is whether a particle passed a pixel or not, which is obtained by applying a threshold to the analog signal of a collection node [25].

For ITS3 a new technology was selected, called 65 nm TPSCo technology, which allowed longer stitched sensor ASICs and thinner epitaxial layer (10 μm instead of 25 μm for the 180 nm technology). The enhancement of sensor performance in the 180 nm TowerJazz imaging technology relied on pixel and process optimization, which subsequently laid the groundwork for process optimization in TPSCo technology. To allow proper comparison between the two technologies, different pixel designs were studied during the initial production stages. At the same time, the stitching allows the connection of otherwise unconnected reticles on a wafer from the early stages of production and during that, the Repeated Sensor Units (RSU), which are selected parts of the reticles, are placed next to each other on the wafer. The End-cap structures are placed on the left and right side of the RSUs and the stitching process of the RSUs is happening in the beam direction. This is in order to interconnect data and power lines from all RSUs to the readout electronics on the left end-cap of the sensor ASIC forming the sensor segment. One of the two large stitched sensor ASICs is the MOnolithic Stitched Sensor (MOSS) [34], that was submitted in the first Engineering Run (ER1) in 2022 and is going to be further discussed in the following section.

4.2 MOSS

The MOSS prototype is the largest of the two prototypes for ER1, with dimensions 25.9 cm $\times$ 1.4 cm, and it consists of 10 RSUs, one left end cap and one right end cap. Every RSU is divided into two halves, top and bottom, called Half Units (HU), which have pixel

arrays with different pitches[3] [34, 35].

Each HU is a fully standalone functional unit with independent periphery, I/Os and powering and are characterised by different circuit densities, different widths and spacing of the interconnecting metal structures [34]. Even though the peripheries are pretty similar for both top and bottom HUs, the pixel pitch values are different in order to study the yield with different layout densities [35]. The top HU has four matrices, also called regions, with 256 × 256 pixels with a pixel of pitch 22.5 μm. The bottom HU also has four regions, but with 320 × 320 pixels with a pixel pitch of 18 μm. In total, MOSS contains 6.72 million pixels and its structure is shown in Figure 13a.

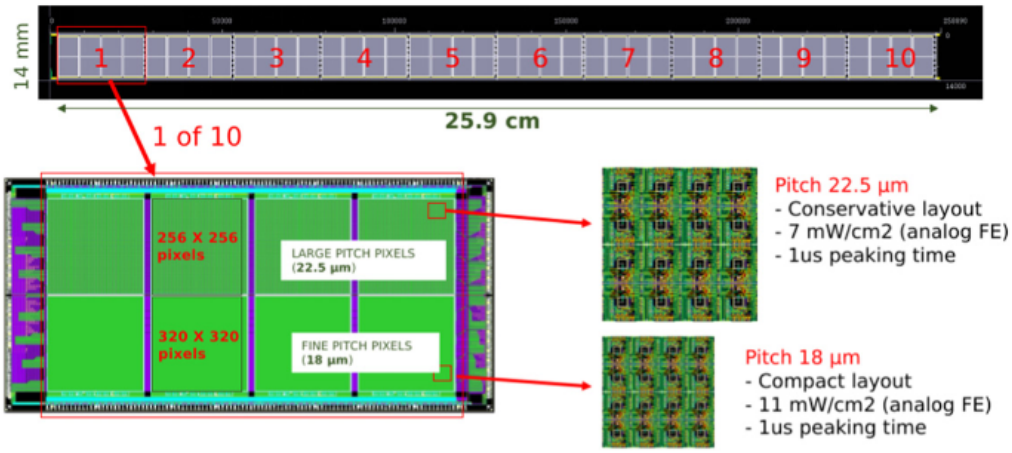

(a)

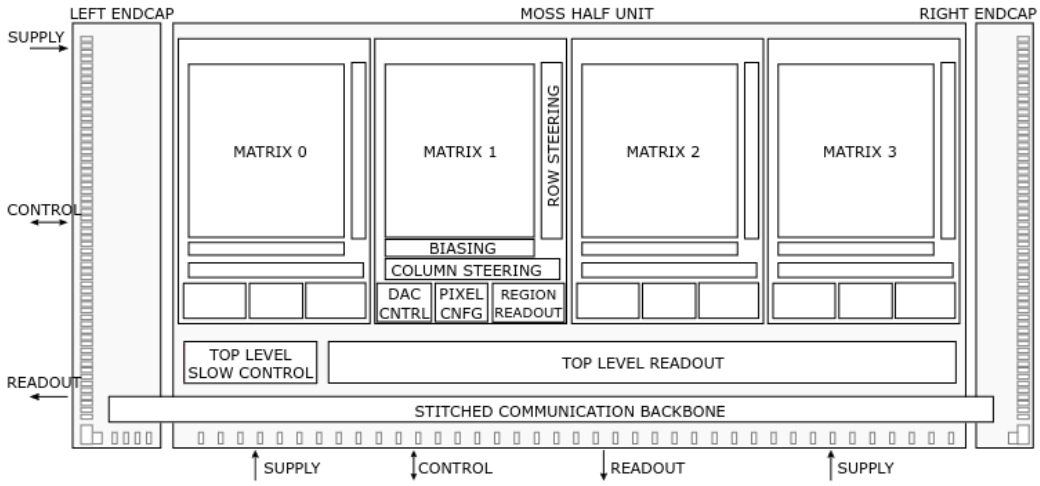

(b)

Figure 13. (a) Schematic view of MOSS showing the top and bottom halves, obtained from Ref. [35]. (b) Block diagram of one bottom half unit of the RSU, from Ref. [34].

The nominal power consumption value in terms of analog power densities is 11 mWcm^{-2} and 7 mWcm^{-2} for the fine (bottom) and coarse (top) pixel pitch, respectively [34]. The requirement for the maximum power density limit is 40 mWcm^{-2}. The power density can be kept below this limit by operating the front-ends below the maximum current setting and by reducing the leakage from applying reverse bias [36]. In addition, it divides the

[3]Pixel pitch is the distance between the center of two neighboring pixels.

pixel matrix into fully separated powered sub-matrices to be powered down in case of defects and defines the yield and electrical performance taking into account leakage currents, noise distributions, spreads of characteristics, etc. [34].

Figure 13b, shows the block diagram of the MOSS bottom RSU and the left and right endcap. Every half unit includes a top-level peripheral control module and a readout module and the only structures crossing the stitching boundaries are the metal interconnects. The metal stripes connecting all power domains extend from the left end-cap to the right end-cap, allowing RSUs to receive power either from pads along the long edge or from pads in the end-caps. The wiring through the stitching boundaries is also employed in the stitched communication backbones. These blocks are the prototypes for the wiring and circuits essential for signaling between RSUs and the left end-cap. The backbone operates within its own independent power domain, following conservative width and spacing layout rules. It uses one control bus for all RSUs and several point-to-point data readout buses to link each RSU with the left end-cap. This setup enables control and readout of the entire MOSS chip through interfaces located on the left end-cap [34].

Figure 14 shows the analog in-pixel front-end circuitry, where one can notice that there are eight different settings, that can affect the operation of the sensor. From the eight settings, there are four current settings, namely I_{reset}, I_{db}, I_{bias} and I_{biasn}, and four voltage settings, V_{casn}, V_{shift} (V_s in Figure 14), V_{casb} and V_{psub}. The most important setting, is V_{casb}, which is the one controlling the threshold, meaning that when V_{casb} increases, the threshold decreases, thus the noise in the sensor is increasing. V_{psub} is the setting that sets the circuit in biasing or reverse biasing, and when reverse bias is applied, then all other settings need to be adjusted accordingly. Finally, I_{reset} is the current that flows through the M7 diode (the diode that controls threshold) and V_{rcas} is a part of the I_{reset} current mirror and not adjustable. The current coming from diode D0 is also passing through M7, meaning that this current, that is a leakage current, has to be smaller, or in an ideal operation condition, equal to I_{reset}, so that the threshold is not affected by it.

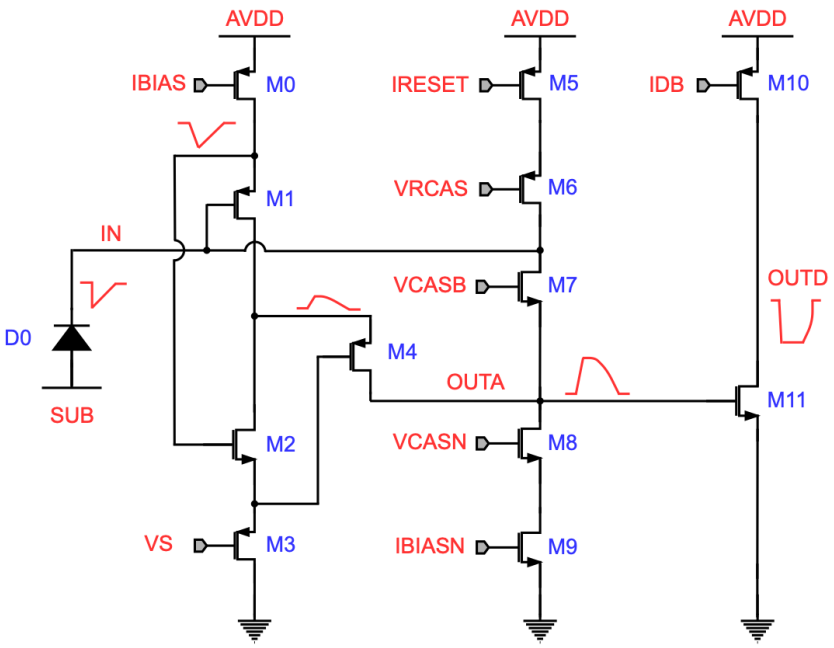

Figure 14. Analog in-pixel front-end with a simplified schematic, depicting all the internal settings of the pixel circuit. Obtained from Ref. [34].

There are different front-end variants within a HU, in order to examine which region operates better. Region 0 has the standard front-end variants for both top and bottom HUs, according to the sensor designers, together with the regions 1 and 2 in the bottom HU. Region 1 in top HU has a larger input transistor (M1), while region 2 has a larger discriminator input transistor (M11). Finally, region 3 in top HU has a larger common-source transistor (M2), and according to the chip designers, region 3 in bottom HU has a slightly different layout [37].

In order to test MOSS, the testing system consists of three different boards and is shown in Figure 15. First is the carrier board, that hosts and connects the MOSS chip and is a passive Printed Circuit Board (PCB), including decoupling. The board provides access to all features of the chip via five 560-pin connectors located along its perimeter. Four connectors are dedicated to the chip's four quadrants, each containing five independently operable HUs. A fifth connector operates the chip as two halves via the stitched backbone. The second kind of boards, are the proximity boards, which are five, one to control and read out each quadrant, and one for each whole top and bottom halves via the stitched backbone, while they also include voltage regulators, monitoring and biasing functionalities and Analog to Digital Converters (ADCs) [34]. Last but not least, is the automation board (or Mama board), which is a module to steer the proximity boards and interface the sensor control and readout with a computer. The Mama Board is connected to a computer via USB3 and it contains an LED that starts flashing when a USB cable is connected, even if the Mama Board is not powered on. It also contains a Field Programmable Gate Arrays (FPGA) that needs to be programmed. Both the Mama Board and proximity card require powering [38].

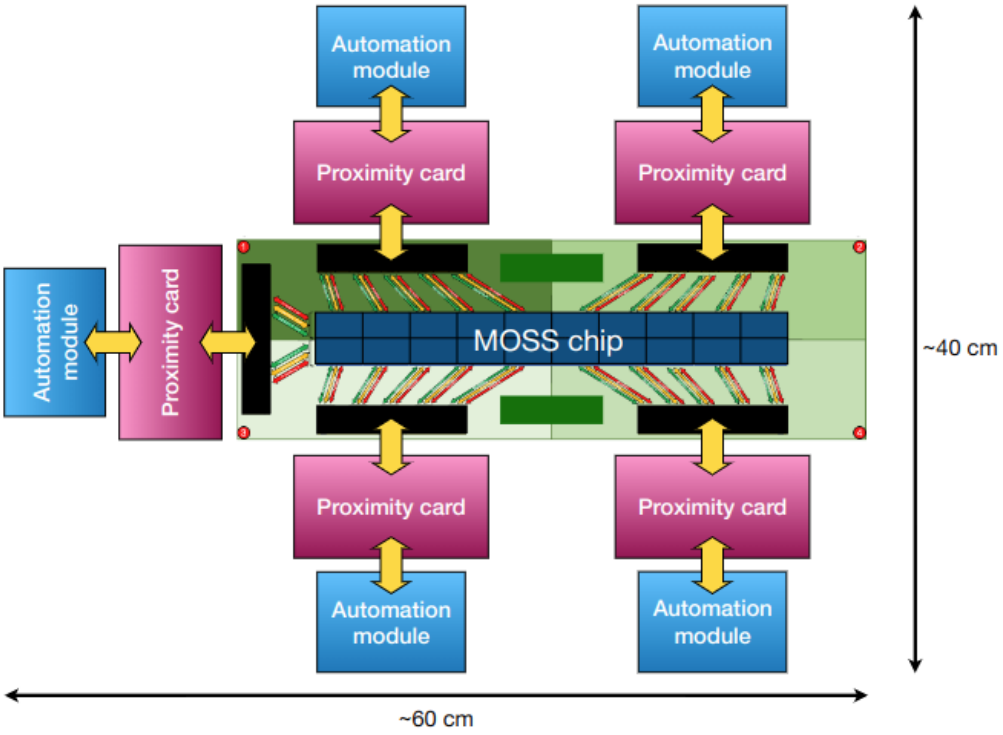

Figure 15. The MOSS testing system consisting of the carrier board, the proximity boards and the automation module. Obtained from Ref. [38] , which is a source accessible only to ALICE members.

4.3 BabyMOSS

As was mentioned in the previous section, MOSS is the largest prototype of ER1, but this also comes with some disadvantages in the testing process. The MOSS testing system is quite large, approximately 75 cm in the diagonal direction, especially if all 10 RSUs are tested. This led to the creation of a smaller prototype, the babyMOSS, which consists of only one RSU with the same features as the RSUs of the MOSS. BabyMOSS helps the testing process because it is smaller, making it easier to fit in a testing telescope and be tested in a test beam. As a result of that, the babyMOSS can be tested with a simpler system.

The babyMOSS testing system, depicted in Figure 16, consists of three boards, as for the MOSS. It is compatible with the proximity board and Mama board of MOSS, but since the production cost of them is large, there was an idea of a new system, less expensive, that uses components with an already well-known operation. Thus, instead of the proximity board, Lund University built the so-called raiser board. The raiser board is an interface between the babyMOSS carrier card, that supports the chip, and the ALPIDE DAQ board. The ALPIDE DAQ board controls and reads out the chip [39], and as the name indicates is also already used for the ALPIDE chips, so its functionality is well known.

Figure 16. Picture from the author, showing the babyMOSS testing system. It includes the ALPIDE DAQ board, the V1.0 raiser board and the babyMOSS carrier board.

The DAQ board is connected with the computer via USB and is the only board out of the three that needs to be connected to external power. The raiser board is connected to the carrier card by a 560-Pin connector and it can operate both HUs at the same time. The babyMOSS chip is wire-bonded to the carrier board and it can be identified with its Carrier Unique ID (CUID) [39].

There are two versions of the raiser board, that were tested in Lund during the period of this thesis and are going to be further discussed in the upcoming section.

4.3.1 Raiser Board

The raiser board is the interface between the ALPIDE DAQ board and the babyMOSS carrier card. It is used to support the babyMOSS and replace the functionality of the

proximity board on the control and read out of the sensor. There were two versions of the raiser board produced, where the second version had more testing points, for checking the voltage levels in different points of the circuit. Also, it contained two potentiometers that could change the voltage levels in a small window of 0.9 - 1.4 V, with 1.2 V being the desired value.

At the time that the new testing system was available, the software and firmware available were the ones used for the MOSS testing system. This meant that there was no possibility to test both HUs at the same time, therefore software and firmware needed to be developed accordingly. To do so, all scripts available for MOSS testing were adjusted to match the new babyMOSS testing system. For the purpose of this thesis, the script to scan all eight DACs that were involved in the analog in-pixel front-end circuit was created. The results of the DAC scans of one babyMOSS are available in Appendix G, which matches the expected output values and behavior of the DACs, according to the schematics[4].

In addition, in order to test the raiser boards and the connection of them with the babyMOSS, scans for the registers were conducted, by writing different values on the registers and reading them back. Moreover, readout tests were done, where the amount of fake hits in each region and each HU were read. In general, region 3 in bottom HU was always the most noisy with increasing V_{casb} (decreasing threshold), and the reason behind that is suspected to be the slightly different layout of that region's analog in-pixel front-end circuit.

Finally, there were 12 version 1 raiser boards produced and immediately sent to CERN and 45 version 2, that were tested as a part of this project and from which only one had a problem in readout.

[4]The schematics of the second version of the raiser board can be found at raiser2schematics.pdf.

Chapter 5

5 ITS3 Test beam data and Analysis procedure

Tests of the pixel matrix of the MOSS and babyMOSS and their response to charged particles have been performed in a number of test beam campaigns at the CERN PS, which the author of this report participated in, and the detection efficiencies and spatial resolutions were determined. Below, there are further details about these test beams.

The first test beam tested four HUs of the MOSS B4, B5, T6, T7, where B and T stand for bottom and top, respectively, for different V_{casb} settings, where V_{casb} is the internal DAC setting that controls the threshold, as explained before. Also, for one HU, there were strobe delay scans and a change in other internal DAC settings, I_{bias} and I_{biasn}. Finally, there was a high statistics run on one HU (T6) with one million triggers per run. The test beam took place from the 27th of September to the 4th of October 2023, with overall good data quality.

The second test beam tested only the top HU of the babyMOSS, but in contrast with previous tests, reverse bias (PSUB) was applied. There was no possibility of testing both HUs simultaneously at the time of the test beam, due to the lack of the appropriate software that reads both of them. The test beam was from the 25th to the 29th of October 2023[5], with overall good datasets, for the tests with different PSUB values and different V_{casn} and V_{shift} settings, provided by the designers.

By the third test beam, it was decided to test an irradiated babyMOSS, with irradiation level 10^{14} 1 MeV $n_{eq}cm^{-2}$. This irradiation is the expected level imposed on ITS3 during its expected future exposure in LHC Run 4 (2029-2032), produced by the fluence of 1 MeV neutrons. Particle fluence refers to the quantity of particles passing through a designated area within a specific point in space over a given interval. Typically expressed in units of particles per square centimeter (cm^{-2}), it provides a measure of particle density over time [40]. The test beam was originally planned to last from the 22nd to the 27th of March 2024, but it was decided to extend it until the 17th of April. The thesis focuses on the testing of the top HU, which took place until the 5th of April. After multiple tests in the lab, each region was tested individually, with and without reverse bias, while the rest of the regions were set in a low V_{casb} value. Then, since region 2 seemed to have the best results, a different value of the internal current I_{reset} was set, as well as a different value for the internal setting V_{shift}, in order to see if there is a better combination of settings. In Chapter 6, there is going to be an analytic description of all the internal settings, the reasons that led to the decision of testing them and the tests that were conducted.

In all cases, the goal of the test beams was the characterisation of the pixel matrices of the sensors, when applying different V_{casb} settings.

5.1 Test beam area: PS T10

The PS is a key component in the accelerator system of CERN and it began its operation in 1959. Typically, it accelerates protons coming from the Proton Synchrotron Booster

[5]The test beam lasted only four days, due to the winter shutdown of the LHC that started on the 29th of October.

or in some occasions heavy-ions coming from the Low Energy Ion Ring (LEIR) [41].

The East Area is an experimental area situated within the PS, located in building 157 of the CERN complex and it contains four beam lines: T8, T9, T10, T11. The PS provides the beam lines with the 24 GeV/c primary beam, which in turn provides 2.4 second cycles with a flat top of about 400 ms. Within these cycles, certain ones are directed towards the North target (for the T9, T10 and T11 beams) and are the ones of interest in this Thesis, but there are also some directed at the South target (for T8). The frequency of East Area cycles per super-cycle varies depending on the current schedule. The T10 beam is a secondary beam that delivers secondary particles and is the beam line where the test beams took place [42]. The particles provided in these test beams were 10 GeV/c π^-.

5.2 Test beam detector setup

At the time of the mentioned test beams, the testing system of the babyMOSS was not yet complete, so the MOSS testing system of the proximity board and the Mama board was used in all cases. The testing system was placed on a metal holder and inside a telescope, with the full setup shown in Figure 17.

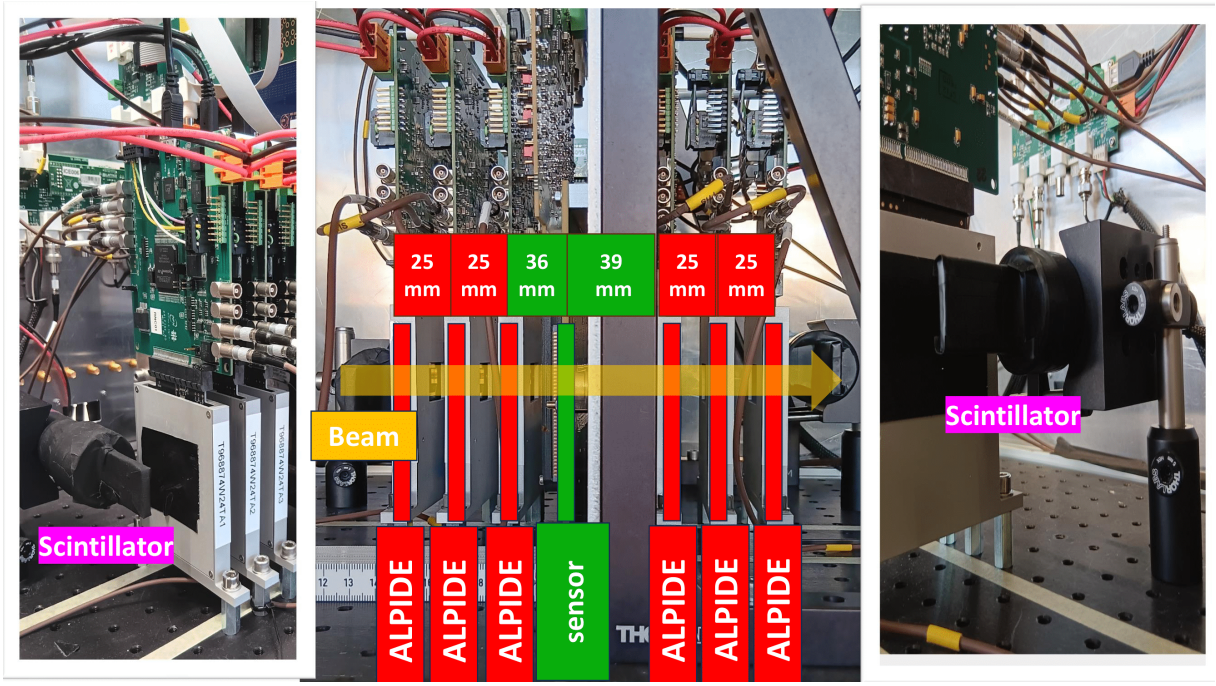

Figure 17. Picture from the author, showing the setup for the test beams, including the sensor tested, six ALPIDE planes as reference planes and two scintillators.

In order to find the efficiency and the spatial resolution of the sensors, reference planes were necessary. Thus, inside the telescope, there were six ALPIDEs, three placed before the sensor and three after it, since the properties of the ALPIDEs are already known. Each ALPIDE had 25 mm distance from the next one and 36 mm with the sensor from the front side (front meaning the one closer to the incoming beam) and 39 mm on the back side.

Also, two scintillators were used, at the edges of the planes (front and back), and they both had to be triggered in order to have a particle detection. In this case, the trigger board was sending a trigger signal to the ALPIDEs and then to the sensor, in

order to start the particle detection. While the scintillators were on, and there was a particle detection, there had to be a signal coming from the sensor and propagating to the ALPIDEs and then to the trigger board, to let them know that it is on the state *Busy*, in which there could not be another particle detection. The reference planes were aligned with the sensor/device under test and with the small opening of the telescope, for the incoming beam.

5.3 Beam information and alignment procedure

Initially, the telescope was aligned with the beam by using a laser and a mark on the wall of the PS T10 area, that indicated the location of the incoming beam. The telescope was put on an adjustable table, that could be moved in all directions with a precision of 10 mm. After a rough alignment, the beam was turned on and the alignment check was done by looking at the correlations of the x and y axis between the first ALPIDE (ALPIDE 0) and the last ALPIDE (ALPIDE 6). The correlation should be a straight line passing by 0. For the x axis, the alignment was quite good, but for the y axis, the correlation was shifted, indicating that the back of the telescope should be lifted. After a calculation to find how large of a distance this correlation line shift corresponds to, it was found to be less than the precision of the adjustable table. This was equal to less than 1 degree of rotation, which led to the conclusion that it would not affect the measurements and the analysis later on.

5.4 Analysis with Corryvreckan

Corryvreckan[6] is a test beam data reconstruction framework based on a modular concept of the reconstruction chain. It is written in C++, and it is designed to fulfill the prerequisites for offline event building in complex data-taking environments combining detectors with varying readout architectures. Users are able to add their own functionality (like event loaders for diverse data formats or analysis modules tailored to explore particular detector features), with an eliminated need to deal with centrally provided functionality, such as coordinate transformations, and analysis configuration, due to the flexibility of the framework [43]. In addition, Corryvreckan does not rely on a specific definition of an event, such as all data are related to a single trigger decision, but leaves it to the user to configure, which data constitute one event [44].

In Corryvreckan, the local coordinate system for a detector plane is a right-handed Cartesian coordinate system, with the x and y axes defining the sensor plane and the z axis pointing towards the readout side of the sensor. Its origin is placed at the centre of the active pixel or strip matrix of the sensor. The global coordinate system for the full detector setup is also a right-handed Cartesian coordinate system, where the z axis points in the direction of the particle beam. The orientation of a detector is described by extrinsic active rotations around the geometrical centre of the sensor. The transformations between local and global coordinate systems for each detector are provided by the detector class of the framework core [44].

There are three kinds of modules in this framework. Global modules are intended to process data from all available detectors, for example by implementing a track-finding algorithm, and are only instantiated once per run. Detector modules exclusively handle data from individual detectors within the setup, e.g. for clustering, and may be constrained to

[6]project-corryvreckan.web.cern.ch

processing data solely from a fragment of the available detectors. Lastly, Device Under Test (DUT) modules are specifically generated for detectors that are marked as such [44]. In these test beams, the DUTs were the MOSS and babyMOSS sensors, but since there can be only one DUT at a time, only one of the four regions was considered as DUT each time, ignoring the rest of the regions. The reconstruction and analysis chain of Corryvreckan and the detector geometry are configured through text files: a main configuration file and a geometry description file. These files contain section headers to identify modules, and key/value pairs for the individual configuration parameters. Corryvreckan is capable of interpreting the provided units, along with configuration parameters [44]. Below, there are further information about these files, as well as the procedure of the analysis, by using these configuration files.

5.4.1 Geometry

The geometry configuration file contains all the properties of the detectors and their position and orientation in the global reference frame. Only the detectors present in this file, are being processed by Corryvreckan. Figure 18, shows examples of the detectors that are included in the geometry file. The section header serves as an identifier for the detector device throughout the reconstruction [44].

```
[ALPIDE_1]
type = "ALPIDE"
position = 0mm,0mm,25mm
number_of_pixels = 1024,512
pixel_pitch = 29.24um, 26.88um
spatial_resolution = 5.00um, 5.00um
time_resolution = 2us
material_budget = 0.0005
coordinates = "cartesian"
orientation = 0deg,0deg,0deg
orientation_mode = xyz
```

(a)

```
[MOSS_reg0_3]
type = "MOSS"
position = 8mm,0mm,85mm
number_of_pixels = 256,256
pixel_pitch = 22.5um, 22.5um
spatial_resolution = 6.5um, 6.5um
time_resolution = 10s
material_budget = 0.024
coordinates = "cartesian"
orientation = 0deg,180deg,0deg
orientation_mode = xyz
role = "DUT"
```

(b)

```
[MOSS_reg1_3]
type = "MOSS"
position = 2mm,0mm,85mm
number_of_pixels = 256,256
pixel_pitch = 22.5um, 22.5um
spatial_resolution = 6.5um, 6.5um
time_resolution = 10s
material_budget = 0.0005
coordinates = "cartesian"
orientation = 0deg,180deg,0deg
orientation_mode = xyz
role = "DUT"
roi=[[80,0],[80,160],[256,160],[256,0]]
```

(c)

```
[MOSS_reg2_3]
type = "MOSS"
position = -4mm,0mm,85mm
number_of_pixels = 256,256
pixel_pitch = 22.5um, 22.5um
spatial_resolution = 6.5um, 6.5um
time_resolution = 10s
material_budget = 0.0005
coordinates = "cartesian"
orientation = 0deg,180deg,0deg
orientation_mode = xyz
role = "DUT"
roi=[[0,0],[0,160],[200,160],[200,0]]
```

(d)

Figure 18. Figure produced by the author. In (a) are the information about the ALPIDE detector in the geometry configuration file, while in (b), (c), (d), the information about the MOSS/babyMOSS detectors for regions 0, 1 and 2, respectively.

The information included are the type of the detector, the position, the number of pixels and the pixel pitch, the spatial and time resolution and the material budget. It also defines the coordinates and the orientation of the device. In Figure 18a, an example of

the ALPIDE information included in the file is depicted (six such modules were used, one for each ALPIDE). Figure 18b, shows the information about the MOSS and BabyMOSS sensor region 0, which is identical to the one of region 3. It is important to note that the framework included MOSS as a detector by the time of the test beams, but not BabyMOSS. Since MOSS and BabyMOSS have the same properties, it is correct to use the same name in Corryvreckan. Also, in this example, the geometry file was used for the analysis of a top HU, thus the number of pixels and pixel pitch are addressed accordingly and the orientation is rotated by 180 degrees on the y-axis. In case of bottom HU, the orientation would be 0 degrees and the pixel pitch and number of pixels different.

In Figures 18c and 18d, are the information for regions 1 and 2. There are two important differences between the section of region 0 and regions 1 and 2. The material budget is different for region 1 and 2, because they are mostly covered by the PCB. This leads to the second difference, which is implementing one more line called Region Of Interest (ROI) and it is used to exclude from the analysis the PCB covered regions. In order to obtain the information about the ROI, the analysis was first done without including this line and then the obtained local residuals were examined. In the regions of the sensor covered by the PCB, the residuals were widened. Last but not least, in each of the geometry information, there was also a line setting the detector as DUT. Since, as was mentioned above, there can only be one DUT at a time, while examining one section (one region), the others were commented out.

5.4.2 Masking, Prealignment and Alignment

The analysis is then done in four steps, with the four different configuration files. The first step is the masking of the noisy pixels, which uses the *createmask.conf* file, that takes the geometry file as an input. It then produces a new configuration file for each one of the regions (commenting the regions that are not counted as DUTs in each case), together with a ROOT[7] file [45], that shows the masked pixels for each region. This step is done only for the lowest V_{casb} (highest threshold) value that was scanned for each run, in order to mask only the pixels that are dead or firing all the time, and not the ones that become noisy with the increase of V_{casb} (decrease of threshold). Next, by using the new configuration file and the *prealign.conf*, the output are new geometry files for every region, as well as a ROOT file that gives information about the correlations between the different devices. In the next step, the DUT participates in the tracking, which means that the residuals of the tracks are optimized through the DUT. This also requires that the region that is specified as DUT is active, while the other regions are introduced as passive. The *align.conf* file then is used four times, one per region, and in each time it gives a new geometry file and an aligned ROOT file. In the ROOT file then, there are also tracking information plots such as χ^2 or χ^2 divided by the number of degrees of freedom (ndof), which should be centered around 1. All combinations of clusters in the first and the last hit detector plane are connected to form a straight line, which is the best approach for the test beam setup. Clusters in further detectors are then added if they are within the spatial cuts (in local coordinates) and time cuts, updating the reference track at each stage [44]. The final step of the analysis is discussed in the next subsection.

[7] www.root.cern

5.4.3 Analysis

The final step of the analysis is using the *analyse.conf* file, together with the output geometry file of the alignment step, which then produces the final analysis ROOT files. In the configuration file, there are several modules specified that produce different histograms. There is a generic analysis module for all types of detectors that produces a number of commonly used plots to gauge detector performance and allows to discard tracks based on their χ^2/ndof value. Another module is used to calculate the efficiency, which is one of the main goals of the analysis. It does so by comparing the cluster positions of the DUT with the interpolated track position at the DUT. The efficiency is calculated as the fraction of tracks with associated clusters on the DUT over the total number of tracks intersecting the DUT (or ROI in regions 1 and 2). In addition, there is a module that establishes an association between clusters on a DUT plane and a reference track. Last but not least, in order to calculate the spatial resolution and the cluster size, there is additional information. The cluster size is contained as a histogram and for the spatial resolution, one needs to have a look at the residuals in the global x and y axes. The residuals should be centered at 0, in the case of successful alignment, because they show the difference of the interpolated track intercept onto a given plane minus the position of its associated cluster [43]. An example of the residuals obtained from the analysis of the babyMOSS with -0.3 V of reverse bias, is shown in Figure 29 in the Appendix A, for regions 0 and 1. In all cases, the residuals are centered at 0, and in Chapter 6, the calculation of spatial resolution, with the help of these files, is going to be further discussed.

Chapter 6

6 Results and discussion

In the upcoming sections, results from all test beams are going to be presented and the analysis procedure is going to be explained in further detail.

6.1 MOSS Detection efficiency and fake-hit rate

During the first test beam, four HUs of MOSS were tested, two from the top HU and two from the bottom. These four HUs were aligned with the ALPIDE planes inside the telescope, by slightly moving the holder in which the MOSS was placed on (and rotating the MOSS by 180 degrees for testing the bottom HU). The goal of the test beam was the characterisation of the pixel matrix, by obtaining the detection efficiency and spatial resolution of MOSS, for different V_{casb} settings. After the analysis with the Corryvreckan framework, Figure 19 shows the results from the top HU 6 testing, where on the left y-axis, there is the detection efficiency in percentage, on the right y-axis, the Fake-Hit Rate (FHR) with units in hits per pixel per event and on the x-axis, the V_{casb} in DAC units. The FHR data were obtained immediately after the data taking by running a script when the beam was turned off.

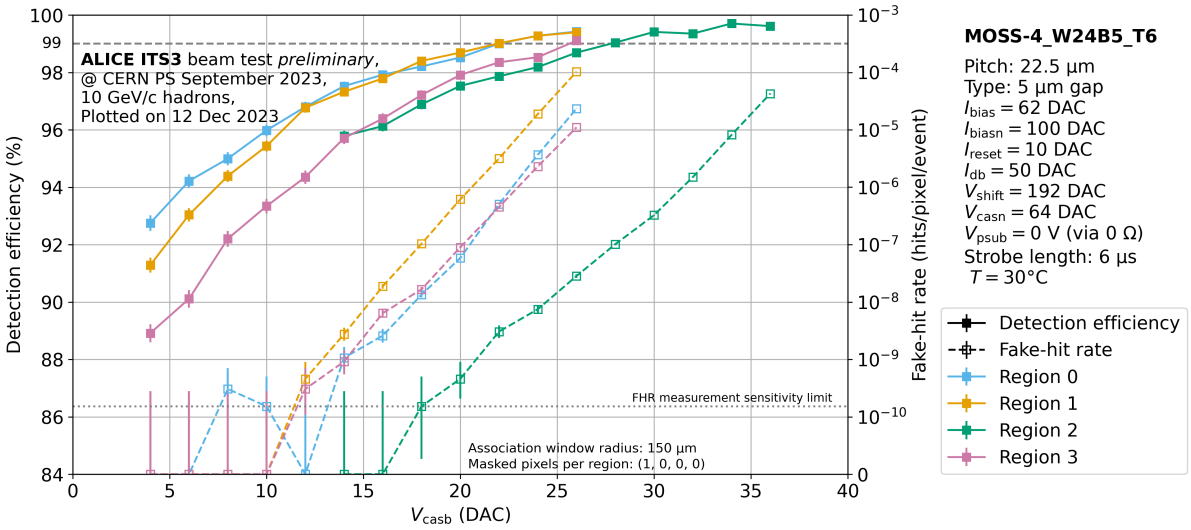

Figure 19. Detection efficiency (solid lines) and fake-hit rate (dashed lines) for different V_{casb} values from the September test beam, for MOSS − 4_W24B5 top HU 6. Region 0 is in blue color, region 1 in yellow, region 2 in green and region 3 in pink [46].

The figure includes the efficiencies (solid lines) and FHRs (dashed lines) of all four regions, while at the same time information about the values from the other settings and the temperature, are indicated on the right side of the plot. In addition, there is information for the number of masked pixels per region, where in this case there is one masked pixel in region 0. There is also a grey dashed line at the efficiency of 99%, which is the efficiency of the ALPIDEs and thus the lowest acceptable efficiency that the ITS3

detector should have. Finally, there is a grey dotted line which is the FHR measurement sensitivity limit.

If one takes a closer look at the figure, regions 0 and 1 only exceed the efficiency limit at V_{casb} values from 22 DAC counts, when the FHR for region 0 is below 10^{-6} hits/pixel/event, while for region 1 it is between 10^{-6} to 10^{-5} hits/pixel/event. In general, in order to consider the efficiency to be in an operational margin, except from the minimum efficiency limit being at 99%, the maximum FHR, after which the sensor becomes too noisy, is 10^{-6} hits/pixel/event. That means that region 0 only has one point in the operational margin, while region 1 has none. Region 3, slightly exceeds the efficiency limit, but the FHR is already too large, so there is no operational point for this region. On the other hand, region 2 seems to have two to three points above the efficiency limit, with the FHR being less than 10^{-6} hits/pixel/event, which means that the operational margin for region 2 is larger, in respect to the other regions.

In Appendix B there are the plots for top HU 7 that was tested, but also for the different I_{bias} (located at the main current branch in Figure 14) and I_{biasn} (current flowing through the cascode transistor M4 in Figure 14) settings, which show that top HU and especially region 2 seems to be the most effective design from this new prototype.

6.2 MOSS Spatial resolution and average cluster size

After determining the efficiency, the next step for the full characterisation of the pixel matrix, was the spatial resolution of the detector. The ROOT files produced by Corryvreckan, gave information about the residuals in global X and Y coordinates and their standard deviation. In order to calculate the spatial resolution, the Telescope Optimiser[8] was used. This is an online website in which one can put the full description of the setup and obtain the tracking resolution. Tracking resolution is the precision with which the detector can determine the trajectory or the path of the particle passing through it. It is an indicator of how accurately the detector can reconstruct the particle's position or other properties and a lower tracking resolution indicates finer spatial measurement capabilities, and thus it makes the detector more precise. For regions 0 and 3, the tracking resolution was 4.66 μm, while for regions 1 and 2, when there was overlap from the MOSS and the PCB, the tracking resolution was 2.18 μm. Varying the material budget for the MOSS regions 0 and 3 by 30% leads to a tracking uncertainty of 0.41 μm, that was considered to be symmetric. Thus the formula for calculating the spatial resolution for the x and y axes was

$$sp.\,resolution = \sqrt{RMS^2_{residuals} - tracking^2} \tag{6.1}$$

where for the x axis the global residual in x was used, and for the y axis, the global residual for the y axis. The mean of these two resolution calculations, equals the general spatial resolution, since the pixel pitch is the same for x and y. In order to calculate the uncertainty in the spatial resolution in regions 0 and 3, the formula for the absolute error of indirect measurement was used [47] (again with the respective x and y values),

$$sp.\,uncertainty = \sqrt{(\frac{residual}{sp.\,resolution})^2(error)^2 + (\frac{tr.\,resolution}{sp.\,resolution})^2(uncertainty)^2} \tag{6.2}$$

[8] mmager.web.cern.ch/telescope/tracking.html

where the error is the RMS error in the residuals, provided in the ROOT file, the tracking resolution is known from the Telescope Optimiser and the uncertainty is 0.41 μm, as mentioned before. Since the tracking uncertainty is considered negligible for regions 1 and 2, the formula in this case can be simplified as

$$sp.\,uncertainty = \frac{residual}{sp.\,resolution}(error) \tag{6.3}$$

This leads to the mean spatial resolution uncertainty given by

$$mean\ sp.\,uncertainty = \frac{1}{2}\sqrt{(sp.\,uncertainty X^2 + sp.\,uncertainty Y^2)} \tag{6.4}$$

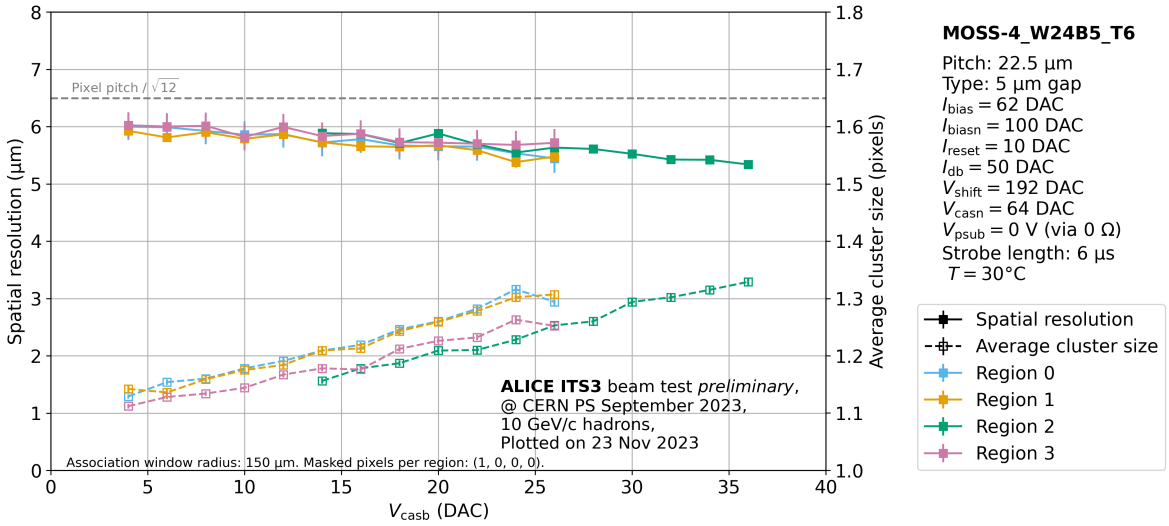

Figure 20. Spatial resolution (solid lines) and average cluster-size (dashed lines) for different V_{casb} values from the September test beam, for MOSS − 4_W24B5 top HU 6. Region 0 is in blue color, region 1 in yellow, region 2 in green and region 3 in pink [46].

Figure 20 shows the plot for spatial resolution (left y-axis) in μm with solid lines and average cluster size (right y-axis) in pixels with dashed lines, as functions of V_{casb} in DAC units, for all regions. The same information as for the efficiency plots are included in this plot, but in this case the theoretical expectation for the spatial resolution (grey dashed line) is included instead of the efficiency limit. The theoretical expectation is given by the ideal case in which a pixel with size equal to the pixel pitch p, would on average get a hit in the center of the pixel, meaning that the standard deviation (variance) would be given by the formula [32],

$$\sigma^2 = \frac{1}{p}\int_0^p (x-\mu)^2\,dx = \frac{p^2}{12} \Rightarrow \sigma = \frac{p}{\sqrt{12}} \tag{6.5}$$

where μ=p/2 (center of the pixel) and in this case the information is in digital form (1 if there is a hit and 0 if there is no hit) and is called single hit response.

In general the spatial resolution can be seen to always be below the theoretical limit, which can be explained by the fact that the average cluster size is larger than 1. The average cluster size should be 1 when the particle hits close to the center of a pixel. If

the hit is closer to the border of the pixel, one can expect some charge-sharing with the neighboring pixel. If the threshold is lowered, it is more likely to register the contribution to the neighbor, and taking the average position of the two hit pixels will then be a slightly better estimate than the center of the pixel.

6.3 BabyMOSS Detection efficiency and fake-hit rate

During the second test beam, it was decided to test a babyMOSS at first without reverse bias, in order to compare the results with MOSS and later on, by applying reverse bias in steps of -0.3 V, from 0 V up to -1.5 V. One of the reasons behind the need to test reverse bias on babyMOSS, was that babyMOSS consists only of one HU, in contrast with MOSS. So, if one wants to apply reverse bias for MOSS, that would be applied to all RSUs, resulting in a risk in damaging the detector in case there is a shortcut present. At the time of the test beam, there was no available software to test the whole sensor, thus it was decided to only test the top HU, that in principle seems to have better operation margins from the results of the previous test beam.

Figure 21 shows the efficiency and FHR as functions of V_{casb} for the different reverse bias (V_{psub}) values, for region 2. It is important to note that the V_{casb} values are increased when reverse bias increases, and in order to find the desirable values for testing, FHR scans before turning on the beam were done in the sensor. The reason behind that increase is that when applying reverse bias, then a depleted region in the epitaxial layer appears and then the flow of the current I_{reset} in the diode D0 and in the M7 changes, thus changing the V_{casb} needed to operate the sensor in normal levels. In Appendix C there are plots for other regions, as well as plots where the V_{psub} value is fixed, but all regions are shown. In addition, the V_{casn} and V_{shift} settings were changed according to the instructions from the designers.

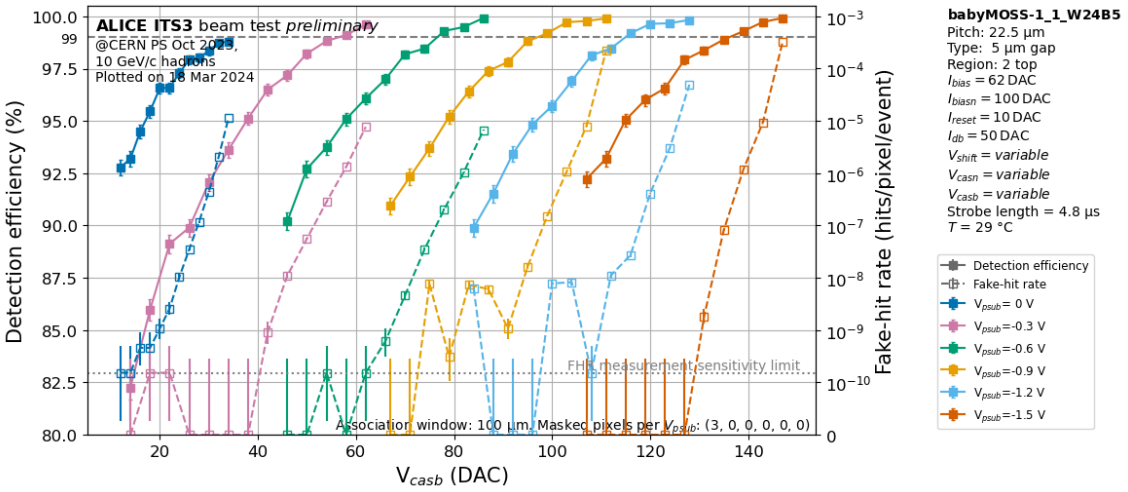

Figure 21. Detection efficiency (solid lines) and fake-hit rate (dashed lines) for different V_{casb} values from the October test beam with babyMOSS-1_1_W24B5, with fixed region 2 and variable reverse bias. Figure produced by the author.

After examining the plot, one can notice that as the reverse bias increases, the efficiency starts exceeding the 99% limit, while the FHR increases less steeply. For example, for

zero reverse bias (dark blue), the efficiency barely reaches the limit, in contrast with the MOSS efficiency from Figure 19, while the FHR is one order of magnitude larger than the maximum limit. But if one looks at higher reverse biases, for example -1.2 V (light blue), there are two points which are above the efficiency limit and below the FHR limit, making the sensor have a small operational margin. Even though the margin is still not the expected for the new ITS3 detector, it led to the important result, that applying reverse bias to the detector improves its functionality. This also resulted into further discussions, as on how this is going to be applied on the MOSS sensor, without the risk of damaging any of the units. It is now planned to test the full MOSS testing system with reverse bias applied, in the upcoming months[9].

6.4 BabyMOSS Spatial resolution and average cluster size

In addition to the detection efficiency, one needed to study also how the reverse bias affects the spatial resolution and average cluster size. The spatial resolution was calculated in the same way as for the MOSS, and the results are shown in Figure 22. By closely studying the figure, one can notice how the spatial resolution shifts to lower values as V_{casb} and V_{psub} increase, while at the same time the average cluster size increases. This is explained in the same way as before, because when the average cluster size is larger than 1 due to the decreased threshold, then the spatial resolution improves/decreases, thanks to the charge-sharing when the hit is near pixel borders. Since the spatial resolution and average cluster size do not seem to have a significant difference from the ones at zero reverse bias, these results are not contradicting the statement that reverse bias improves the operational margins of the sensor. Thus, reverse bias seems to have a positive impact on the sensor operation.

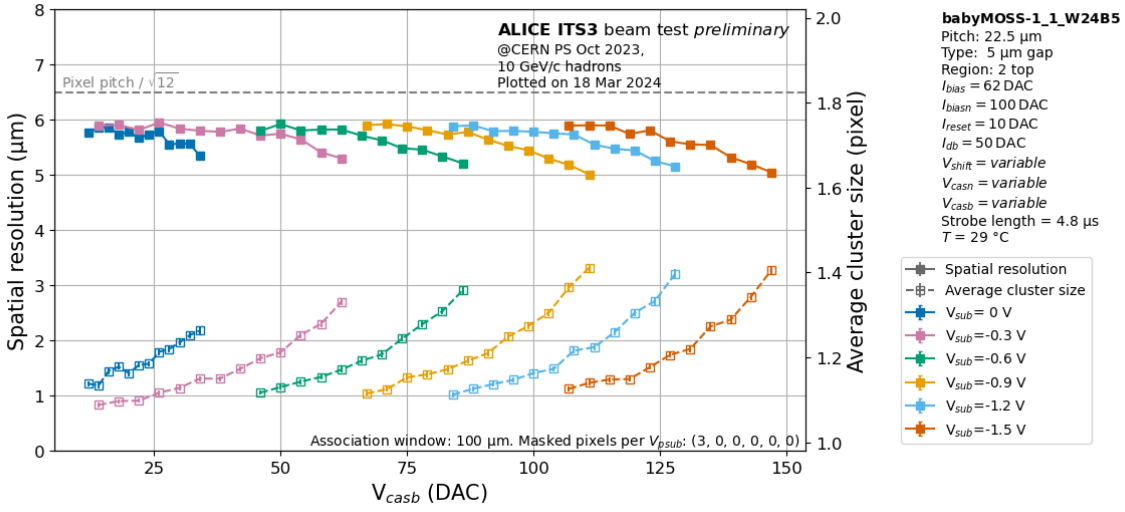

Figure 22. Spatial resolution (solid lines) and average cluster-size (dashed lines) for different V_{casb} values from the October test beam with babyMOSS-1_1_W24B5, with fixed region 2 and variable reverse bias. Figure produced by the author.

[9]Not until after this Thesis is finished.

6.5 Irradiated BabyMOSS Detection efficiency and fake-hit rate

After the first two test beams, the ITS3 collaboration continued testing the sensors, in order to understand better their behavior under certain conditions, such as temperature variation and different internal settings, to be able to apply reverse bias to the complete MOSS testing system and also to convert V_{casb} values to threshold values. Even though the results here are presented as functions of V_{casb}, in Appendix H, there are also plots versus threshold. While conducting these tests, it was noticed that temperature variations significantly affected the FHR and the threshold (THR) as functions of V_{casb}. This led to the testing of the MOSS in a climate chamber, where it was observed that FHR increases with increased temperature as a result of the lowering of the threshold. The reason behind that, is that the leakage current increases with increased temperature. This results in more current flow from I_{reset} to the diode D0 (to compensate for the leakage), thus less current flowing through diode M7 (from Figure 14), thus changing the threshold. At the same time, it was observed that for high V_{casb} values (low threshold) and when the sensor becomes more noisy, the regions start to affect one another, resulting in more noise. In order to be more precise, it was decided that in the next test beam, every region would be tested individually, while the rest of them will be at a fixed low V_{casb} (high threshold) value, to not affect the one tested.

Since the tests on the MOSS with reverse bias were not complete by the time of the third test beam, an irradiated babyMOSS was decided to be tested, with an irradiation level of 10^{14} 1 MeV n_{eq} cm^{-2} (Results from the comparison with a second tested irradiated babyMOSS are included in Appendix I). When a sensor is irradiated, the leakage current increases, meaning that the I_{reset} has to be increased further, to be able to compensate for the leakage current and at the same time the threshold will change due to the change in the current flowing through the M7 diode. If the I_{reset} is slightly higher than the leakage current and there is a sudden increase in temperature, then the front-end circuit will not be able to work anymore. Thus, instead of using the nominal I_{reset} value of 10 DAC, 30 DAC was used instead, which was the value for which the babyMOSS was functioning in normal lab conditions.

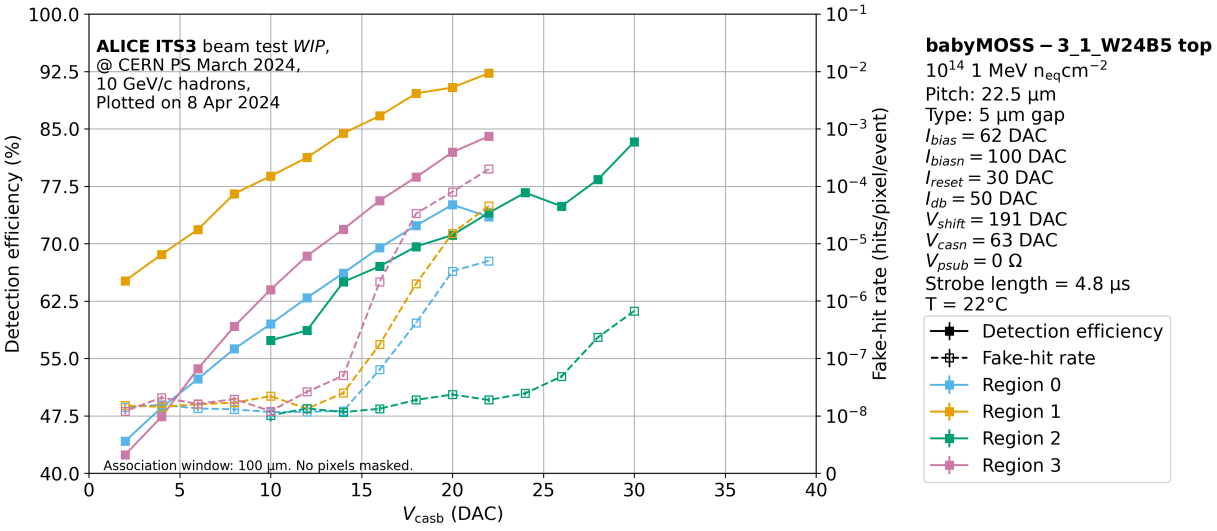

Figure 23. Detection efficiency (solid lines) and fake-hit rate (dashed lines) for different V_{casb} values from the March test beam with the irradiated babyMOSS-3_1_W24B5, with grounded reverse bias for all regions. Figure produced by the author.

Figure 23 shows the efficiency (solid lines) and FHR (dashed lines) plots as functions of V_{casb} for the irradiated babyMOSS, at a grounded reverse bias for all regions. As was mentioned before, each region was tested individually, while the others were set in a low V_{casb} value (5 DAC) - high threshold. Another difference between this test beam and the previous ones, is that the temperature was almost ten Celsius degrees lower and almost equal to the temperature at which the lab tests were conducted. It is clear from the image, that there is no region or setting, for which the irradiated babyMOSS is reaching the operational margin, even though regions 1 and 2 seem to be operating slightly better than regions 0 and 3, by having lower FHR and reaching higher efficiencies.

6.5.1 I_{reset}

As was explained above, I_{reset} is needed to overcome the leakage current, but also flow through M7 and change the threshold. It was then decided, to increase I_{reset} to 40 DAC in region 2 and study the effects in the efficiency and the FHR (or threshold). Figure 24 shows the detection efficiency (solid lines) and FHR (dashed lines) as functions of V_{casb} for the different I_{reset} values, for region 2.

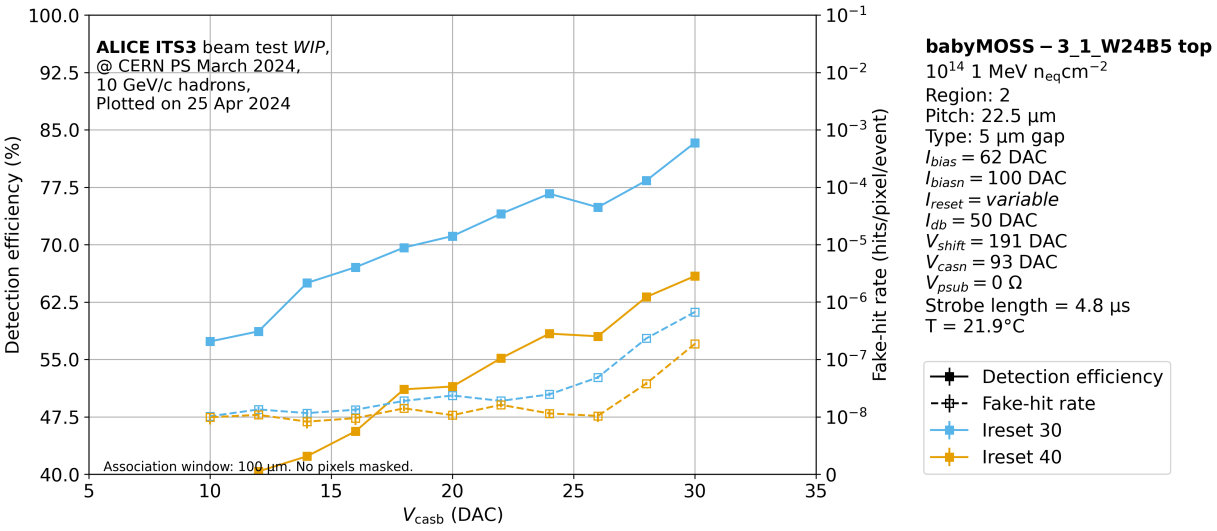

Figure 24. Detection efficiency (solid lines) and fake-hit rate (dashed lines) for different V_{casb} values from the March test beam with the irradiated babyMOSS-3_1_W24B5, with grounded reverse bias and different I_{reset} settings for region 2. Figure produced by the author.

One can notice from the image that the efficiencies are much lower than the lower limit, with the efficiency at I_{reset} 40 DAC (yellow solid line) being more than 10% lower, while the FHR for both values is almost equal. That indicates that higher I_{reset} is less effective, but FHR was expected to be different for both cases, since by changing I_{reset}, the threshold is indirectly affected. Therefore, this measurement has to be repeated in the future in a more controlled environment as is the lab, in order to verify that the measurement in the test beam was correct and to understand the origin of the result. It is important to note that at the time of the measurement there was a problem with the beam, which resulted in a beam stop for a few days, so it is suspected that there could also have been noise contamination in the results.

6.5.2 V_{shift}

While testing the parameters of MOSS, there was an indication that V_{shift} could provide better sensor operation, if decreased. Figure 25 shows FHR (left) and THR (right) as functions of V_{shift}, for top HU 2, region 2. The nominal value for V_{shift} is 191 DAC, but while FHR seems to be steady for such a value, THR seems to be on the edge of the steady region. Plots for other regions are included in Appendix D, where this effect is more clearly seen. This resulted in the decision that V_{shift} could be decreased to the first available operational setting below 150 DAC, where FHR is steady, and THR does not start increasing yet. Thus, it was decided to study the irradiated babyMOSS with a V_{shift} value of 142 DAC for region 2 in the test beam, with the other regions fixed in a low V_{casb} (high threshold) value of 5 DAC.

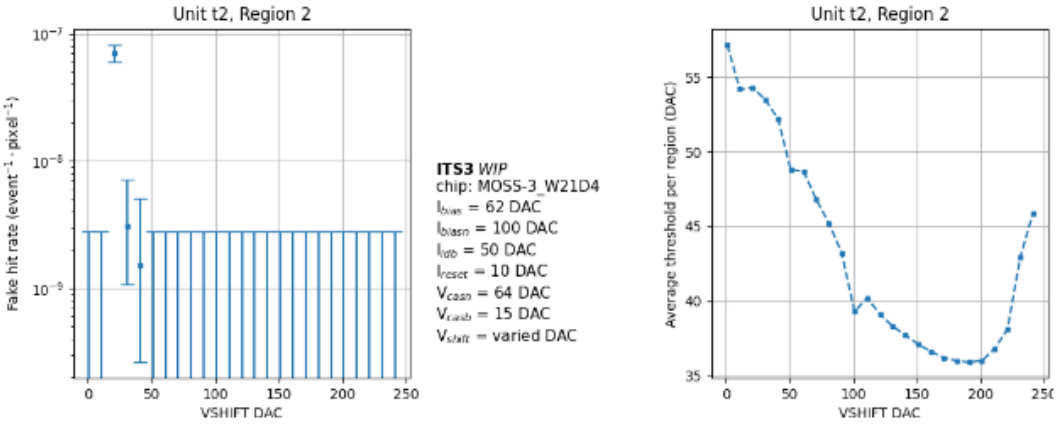

Figure 25. Left: the fake hit rate as a function of V_{shift} in DAC units. Right: the average threshold per region as a function of V_{shift} in DAC units. Both plots are for top HU 2, region 2 of MOSS-3_W21D4, which should be similar for the babyMOSS, since they have the same analog in-pixel circuitry. Figure produced by the test beam team.

Figure 26 shows the detection efficiency and FHR as functions of V_{casb} for different V_{shift} values, for region 2. The nominal V_{shift} is in blue and the V_{shift} that was decided by the test beam team is in yellow. It is clearly seen again that the efficiency for both V_{shift} settings does not reach the 99% limit, even though the FHR is already higher than the maximum limit. By looking at the efficiency, one can understand that the efficiency of the nominal V_{shift} test is higher for all V_{casb} values than the one of V_{shift} 142 DAC.

At the same time, FHR for low V_{casb} values, seems to be very similar for both V_{shift} settings, but at a V_{casb} of around 18 DAC, FHR for the V_{shift} of 142 DAC with the yellow solid line, makes a steep increase of around two orders of magnitude in comparison with FHR of nominal V_{shift} (solid blue line). This, together with the fact that the efficiency is around 10% lower, in all V_{casb} values for the lower V_{shift}, leads to a clear result that nominal V_{shift} provides better operation for the sensor. Therefore, since this is in contrast with the parameter scans, the scans are going to be performed again in the future, to better understand the reason behind this contradiction between lab and test beam measurements (if it is due to temperature variations etc.).

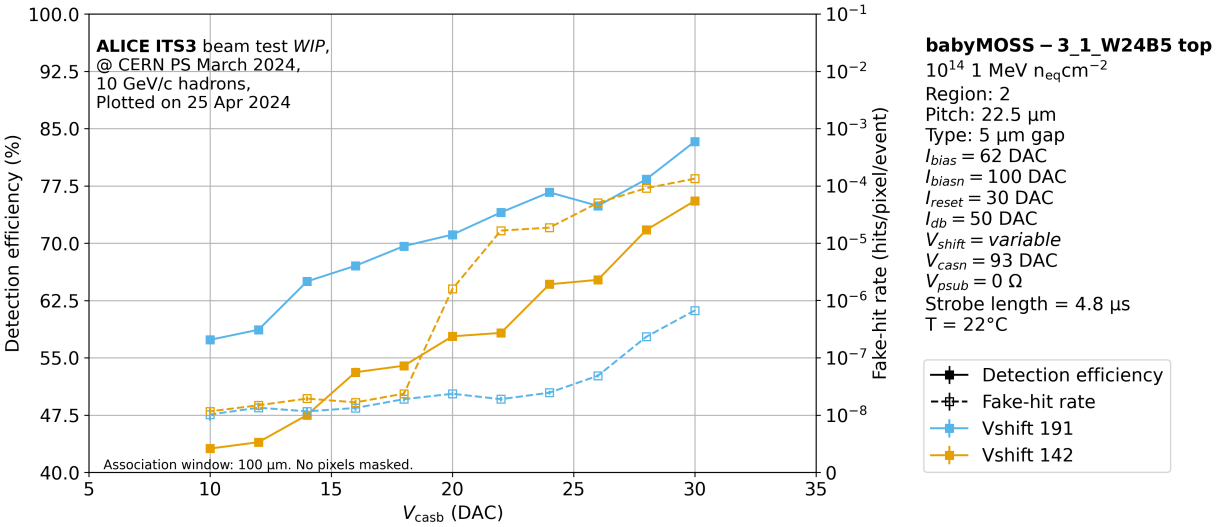

Figure 26. Detection efficiency (solid lines) and fake-hit rate (dashed lines) for different V_{casb} values from the March test beam with the irradiated babyMOSS-3_1_W24B5, with grounded reverse bias and different V_{shift} settings, for region 2. Figure produced by the author.

6.5.3 Reverse bias

The last part of testing the top HU of this irradiated babyMOSS, was by applying reverse bias, which as was seen in the last test beam, had a positive effect on the operation of the sensor. It was decided to test a reverse bias of -1.2 V, for each region individually, while the rest of them were set in a low V_{casb} value, to not affect the region tested. The regions that were fixed, were set with a V_{casb} value of 70 DAC instead of 5 DAC, since when applying reverse bias the V_{casb} value needs to be increased in order to have the same noise levels. This lowering of the threshold was made in order to have higher statistics for the regions that are not scanned. Also, V_{shift} and V_{casn} were adjusted accordingly with the settings provided from the designers.

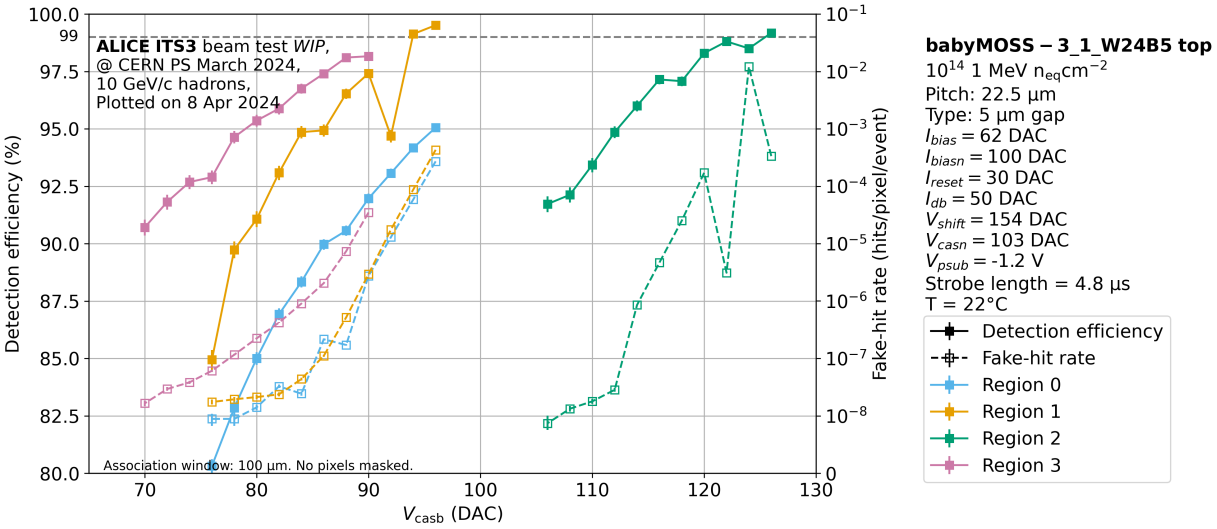

Figure 27. Detection efficiency (solid lines) and fake-hit rate (dashed lines) for different V_{casb} values from the March test beam with the irradiated babyMOSS-3_1_W24B5, with grounded reverse bias. Figure produced by the author.

Figure 27 shows the detection efficiency and FHR as functions of V_{casb}, for all regions for a reverse bias of -1.2 V. The 99% efficiency limit is also included in the plot as well as information about the number of masked pixels, which is zero in this case. After taking a closer look at the image, one can notice that only regions 1 and 2 exceed the efficiency limit, again indicating that they operate slightly better than regions 0 and 3. At the same time, the FHR is much higher than the maximum limit, resulting in the sensor having no operational margin.

Even though one would expect the efficiency to constantly increase, at a V_{casb} of 92 DAC, there is a sudden drop in efficiency. During the testing of region 1 with reverse bias applied, it was observed in the correlation plots that when V_{casb} exceeded 90 DAC, the noise in the sensor was too much and also the data files were 10 times larger than normally. At the V_{casb}=92 DAC, the correlations looked less noisy, which was not matching the expectations. The correlation plots are shown in Appendix E. It was thus decided that the reason behind this abnormal behavior was the presence of very high levels of noise, that resulted in the unexpected performance of the sensor at higher V_{casb} values. The same explanation could also be given for the "bumps" of region 2 FHR, but the FHR scans are going to be repeated in the lab, in order to have a clearer view, in a more controlled environment. In general, it is evident that applying reverse bias to the sensor, improves its operating performance.

6.6 Irradiated BabyMOSS Spatial resolution and average cluster size

Since the most effective operation of the irradiated babyMOSS, is by applying reverse bias, Figure 28 shows the spatial resolution (solid lines) and average cluster size (dashed lines) as functions of V_{casb}, for -1.2V reverse bias and including all regions. The spatial resolution and average cluster size plots of all other scans conducted, are included in Appendix F.

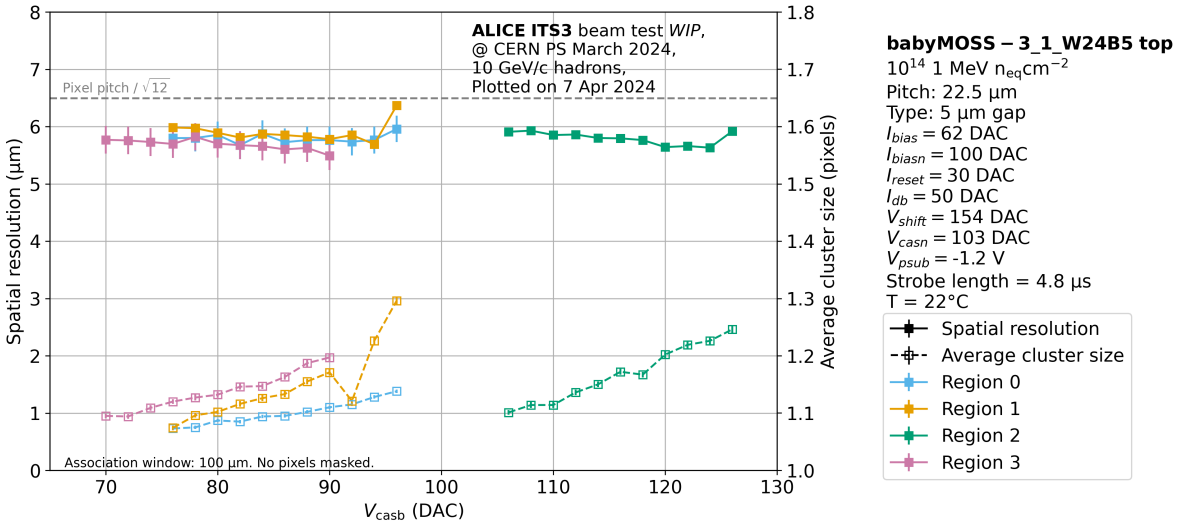

Figure 28. Spatial resolution (solid lines) and average cluster size (dashed lines) for different V_{casb} values from the March test beam with the irradiated babyMOSS-3_1_W24B5, with -1.2 V reverse bias applied and for all regions. Figure produced by the author.

The spatial resolution in this case is again below the theoretical limit obtained by

equation 6.5. In region 1 it is seen again for V_{casb} 92 DAC that the spatial resolution makes a small increase and the average cluster size decreases, matching the behavior of the sensor seen in the efficiency and correlation figures discussed in the previous section. Later, when the noise becomes too high, the average cluster size increases to 1.3, indicating the presence of noise. It is also observed that for regions 0, 1 and 2, spatial resolution starts increasing, approaching the theoretical limit. This is a result from scanning the sensor in V_{casb} values that are already too high for operation, since the noise is much higher than the maximum limit. The same behavior would have been expected of region 3, if V_{casb} was increased even further.

Chapter 7

7 Conclusion and outlook

7.1 Discussion

As was discussed in Chapter 6, several test beam campaigns were conducted, and new results were obtained, that contribute in the characterization of the pixel matrix of the first large-scale prototypes for ITS3.

When MOSS was tested in September, different HUs were examined under different V_{casb} conditions, but with the remaining settings being fixed at the nominal, suggested by the chip designers, values. The efficiency for the top HUs had a larger operational margin, and especially for region 2. This margin is smaller than the required for the ITS3 detector, thus leading to the ITS3 team discussing ways to improve the detector performance.

In the second test beam and when the first babyMOSS was examined, only the top HU was studied under nominal settings and by applying reverse bias. The operational margin of the babyMOSS without reverse bias was smaller than the one of the two top HUs of MOSS that were tested. In principle and since the MOSS and babyMOSS consist of the same circuits, the efficiency in both cases should be approximately equal, which is not the case. This can also be observed by the difference the two HUs have in efficiency. In order to understand these effects, the ITS3 team decided to conduct more detailed tests on the detectors, by testing each HU individually under different operational settings. Since the detector involves the stitching technology, for the first time in this type of application, it was important to understand how this affects the electrical parameters in the pixel circuits. Changing the value of one parameter in the analog front-end in-pixel circuit also affects the other DAC settings, thus introducing the need to understand thoroughly how this circuit works. At the same time, applying reverse bias in the sensor, resulted in a much higher operational margin with the FHR showing a slight decrease. Therefore, another parameter that was decided to be tested in the future on the MOSS was the reverse bias[10].

By the time of the third test beam, many tests were conducted on both MOSS and babyMOSS in the laboratory, in order to understand the functionality of the detector. The most important observation at this time was that when the threshold is lowered, resulting in the presence of more noise in the detector, then the regions start affecting one another, resulting in even more noise. At the same time, scans where all parameters are changed were done, so that one can understand the effect these changes have in the FHR. Since the tests on the MOSS were not finished yet, it was decided to test an irradiated babyMOSS for the first time. To power on the irradiated babyMOSS, I_{reset} had to be increased, to compensate for the leakage current that is present in the irradiated detector. Simultaneously, some differences between the FHR values obtained in the second test beam and the ones observed in the lab tests were noticed, which were equal to 2 orders of magnitude. At first, there was an idea that these differences are caused by the different temperature of around 10 Celsius degrees in the sensor, between the lab and the test beam area. The MOSS was placed inside a climate chamber, where it was shown that

[10]The tests with application of reverse bias on the MOSS detector have not yet been completed by the end of this thesis.

temperature affects the threshold by changing the amount of leakage current composed in the diode that controls the threshold, resulting in the variations in the FHR measurements between the lab and the test beam. In addition, while scanning the different DAC settings, it was seen that a lower V_{shift} could result in lower FHR levels. As was presented in the results in Chapter 6, lowering V_{shift} led to the FHR being approximately two orders of magnitude higher than for the nominal value and the efficiency almost 10% lower. Even though an increase in I_{reset} was expected to improve the efficiency, it had the opposite effect, with the tests of the sensor with a lower I_{reset} being impossible, since in that case the sensor could not be powered on due to the high leakage current. The application of reverse bias increased the efficiency significantly in comparison with the efficiency with grounded/zero bias, but there was still no operational margin in any case.

All the other DAC settings are planned to be tested in the upcoming months and after the end of this thesis work.

7.2 Summary

This thesis focused on the characterization of the first large-scale prototype of the new ITS3 detector upgrade that is going to be installed in the next Long Shutdown of LHC in the ALICE experiment. The ITS3 detector is going to consist of very thin bent silicon layers in the three innermost layers, using the new CMOS 65 nm technology. Monolithic Active Pixel Sensors (MAPS) were studied, in order to understand their properties and the process of detecting particles. Stitching, which allows the connection of otherwise unconnected reticles on a wafer, was used to produce the large-scale prototype, which consists of 10 RSUs. This prototype is called MOnolithic Stitched Sensor (MOSS) and it has different number of pixels and pixel pitches in each half unit, as well as slightly different analog front-end circuitry for some regions, so as to test which is the best candidate for the final detector. BabyMOSS, which is 1/10th of the MOSS in terms of size, and consists of only one unit, was also tested. The testing system of MOSS, which consists of five Mama Boards and five proximity boards, is quite large, 75 cm in the diagonal direction, meaning it is hard to build a telescope with these sizes. Thus, babyMOSS is ideal for such tests, since it is compatible with the MOSS testing system (Mama board and proximity board), but also it can be tested with cheaper components, as the ALPIDE DAQ board, for which the operation was already familiar, and the raiser board. The raiser boards were produced in Lund and were tested during this thesis.

For the purpose of this thesis, there was participation in three test beams, in order to obtain the detection efficiency and spatial resolution of the detector. The analysis of the test beams was conducted with the help of the Corryvreckan framework that is designed for such purposes. The Corryvreckan framework used the detailed structure of the sensors, which was provided externally by specifically created geometry configuration files, different for each HU.

In the first test beam, four HUs of MOSS were tested under different V_{casb} values, that altered the threshold. It was in general observed, that top HU with the pixel pitch of 22.5 μm, operates better than bottom HU, and from all regions of the top HU, region 2 seems to be better. Region 2 has a larger discriminator in the analog front-end in-pixel circuitry, and it requires a higher V_{casb} value to reach the same noise levels as the other regions.

In the second test beam, the top HU of a babyMOSS was tested, in order to compare the results with the results from the testbeam with MOSS, which showed slightly worse

results. Then reverse bias was applied for the first time, and the behavior under this condition was examined. The operational margins of the sensor were increasing, with the increase of reverse bias, as was seen from the detection efficiency plots. The spatial resolution was not showing any significant difference that would indicate any problem with the detector.

Therefore, in the third test beam an irradiated babyMOSS was tested, at first with grounded reverse bias, showing that there is no operational margin. Then, different parameters were scanned, I_{reset} and V_{shift}, to check the correspondence of the detector in a change of these parameters that affect the threshold and the leakage current. Finally, reverse bias was applied, which showed again the increase in efficiency in such a case, but there was no operational margin, even though the efficiency managed to exceed the ALPIDE efficiency limit. The spatial resolution did not show any negative effect of the irradiation in the sensor, since it was below the theoretical limit.

In general, the sensor needs further improvements, as expected, before the installation, since the operational margin is still small under conditions of zero irradiation. The results of some of these studies are included in the Technical Design Report (TDR), that is going to be published in the upcoming months.

7.3 Further studies

While working on this thesis, there were a lot of tests conducted on the prototype, in order to fully understand its functionality. Even though it was possible to move from V_{casb} values to threshold values, these values are still in DAC units instead of electron units. This is something that should be studied in the future, so that the studies have a more physical aspect. In addition to that, during the third test beam, there were a lot of different parameters to take into account, for example the temperature, I_{reset}, V_{shift} and many more other internal DAC settings. It should be well understood how each one affects the sensor, in order to have a better understanding of the results. All these tests can and will be conducted in a lab first, in a more controlled environment, and in a climate chamber.

Last but not least, MOSS should be tested with reverse bias applied, to check how this would affect its operation, but also to have a clearer image about the implications of the stitching in tasks like this. This is something that would be important for the final detector design and operation.

All these studies are going to be used for the design of the hopefully final detector in Engineering Run 2 (ER2) at the end of the year, which is called MOnolithic Stitched pArticle pIXel detector (MOSAIX).

References

[1] CERN. The Standard Model. https://home.cern/science/physics/standard-model. Accessed January 2024.

[2] THE NOBEL PRIZE. Peter Higgs. https://www.nobelprize.org/prizes/physics/2013/higgs/facts/. Accessed January 2024.

[3] Aad G, Abajyan T, Abbott B, Abdallah J, Abdel Khalek S, Abdelalim A, Abdinov O, Aben R, Abi B, Abolins M, *et al.* 2012 Observation of a new particle in the search for the standard model higgs boson with the atlas detector at the lhc. *Physics Letters B* **716**, 1, 1–29. (doi:https://doi.org/10.1016/j.physletb.2012.08.020).

[4] CERN. The Large Hadron Collider. https://home.cern/science/accelerators/large-hadron-collider. Accessed January 2024.

[5] The ALICE Collaboration. 2008 The alice experiment at the cern lhc. *Journal of Instrumentation* **3**, 08, S08002. (doi:10.1088/1748-0221/3/08/S08002).

[6] CERN. ALICE ITS3. https://alice-collaboration.web.cern.ch/menu_proj_items/ITS-3. Accessed January 2024.

[7] CERN. ALICE ITS. https://alice-collaboration.web.cern.ch/menu_proj_items/its. Accessed January 2024.

[8] Universität Zürich. Standard Model. https://www.physik.uzh.ch/groups/serra/StandardModel.html. Accessed January 2024.

[9] Chandler D. 1987 Introduction to modern statistical. *Mechanics. Oxford University Press, Oxford, UK* **5**, pp. 94–97.

[10] Brian R M, Graham S. 2017 *Particle Physics.*, vol. Fourth edition of *The Manchester Physics Series*. Wiley.

[11] Wikipedia contributors. 2023. Hadron — Wikipedia, the free encyclopedia. https://en.wikipedia.org/w/index.php?title=Hadron&oldid=1177490451. [Online; accessed 22-January-2024].

[12] CERN. Heavy ions and quark-gluon plasma . https://home.cern/science/physics/heavy-ions-and-quark-gluon-plasma. Accessed January 2024.

[13] 2017 Enhanced production of multi-strange hadrons in high-multiplicity proton–proton collisions. *Nature Physics* **13**, 6, 535–539.

[14] Herrmann N, Wessels JP, Wienold T. 1999 Collective flow in heavy-ion collisions. *Annual Review of Nuclear and Particle Science* **49**, 1, 581–632.

[15] The Editors of Encyclopaedia Britannica. Scattering. https://www.britannica.com/science/scattering. Accessed January 2024.

[16] Stefano Meroli. Exploring the Physics of Multiple Scattering for Particles in Matter. https://meroli.web.cern.ch/lecture_multiple_scattering.html. Accessed January 2024.

[17] Mukund Gupta. Calculation of radiation length in materials. https://cds.cern.ch/record/1279627/files/PH-EP-Tech-Note-2010-013.pdf. Accessed January 2024.

[18] Poonsawat W, Kobdaj C, Sitta M, Yan Y. 2017 Material Budget Calculation of the new Inner Tracking System, ALICE. Material Budget Calculation of the new Inner Tracking System, ALICE. Tech. rep. 13 pages, 9 figures, regular paper.

[19] Wikipedia contributors. 2024. Large hadron collider — Wikipedia, the free encyclopedia. https://en.wikipedia.org/w/index.php?title=Large_Hadron_Collider&oldid=1197111079. [Online; accessed 23-January-2024].

[20] CERN. ALICE. https://www.home.cern/science/experiments/alicer. Accessed January 2024.

[21] ALICE Collaboration. Definition of the ALICE Coordinate System and Basic Rules for Sub-detector Components Numbering. https://alice-servotech.web.cern.ch/HELP_DCDB-SVT/Help_Files/ALICE-INT-2003-038.pdf. Accessed January 2024.

[22] ATLAS EXPERIMENT. Rapidity and Pseudo-rapidity . https://atlas.cern/glossary/rapidity. Accessed January 2024.

[23] ALICE Figure. 3D ALICE Schematic RUN3 - with Description. https://alice-figure.web.cern.ch/node/11220. Accessed January 2024.

[24] Zampolli C. 2012 Particle identification with the alice detector at the lhc pp. 1–3.

[25] Abelev B, *et al.* 2014 Technical Design Report for the Upgrade of the ALICE Inner Tracking System. *J. Phys. G* **41**, 087002. (doi:10.1088/0954-3899/41/8/087002).

[26] Musa L. 2019 Letter of Intent for an ALICE ITS Upgrade in LS3. Tech. rep., CERN, Geneva. (doi:10.17181/CERN-LHCC-2019-018).

[27] Gianluca Aglieri Rinella. Overview of the ALPIDE Pixel Sensor Features. https://indico.cern.ch/event/863068/contributions/3752479/attachments/1996261/3330551/20200302-Aglieri-ALPIDE-Overview.pdf. Accessed January 2024.

[28] M Suljic on behalf of the ALICE Collaboration. ALPIDE: the Monolithic Active Pixel Sensor for the ALICE ITS upgrade. https://cds.cern.ch/record/2658226/files/fulltext.pdf. Accessed January 2024.

[29] Luciano Musa. Proposal for an ITS Upgrade in LS3. https://indico.cern.ch/event/836343/contributions/3533228/attachments/1896081/3128198/BERGEN_2019_Musa.pdf. Accessed May 2024.

[30] ALICE collaboration. 2018 Expression of Interest for an ALICE ITS Upgrade in LS3 .

[31] Rossi L. 2006 *Pixel detectors: From fundamentals to applications*. Springer Science & Business Media.

[32] Kolanoski H, Wermes N. 2020 *Particle Detectors: Fundamentals and Applications*. Oxford University Press. (doi:10.1093/oso/9780198858362.001.0001).

[33] Mager M. 2016 Alpide, the monolithic active pixel sensor for the alice its upgrade. *Nuclear Instruments and Methods in Physics Research Section A: Accelerators, Spectrometers, Detectors and Associated Equipment* **824**, 434–438. (doi: https://doi.org/10.1016/j.nima.2015.09.057). Frontier Detectors for Frontier Physics: Proceedings of the 13th Pisa Meeting on Advanced Detectors.

[34] ALICE collaboration. 2023 Technical design report of ITS3: A bent wafer-scale monolithic pixel detector p. 171.

[35] Leitao PV, Rinella GA, Bugiel S, Cecconi L, de Melo J, Robertis GD, Deng W, Martin AD, Dorosz P, Fang X, *et al.* 2023 Development of a stitched monolithic pixel sensor prototype (moss chip) towards the its3 upgrade of the alice inner tracking system. *Journal of Instrumentation* **18**, 01, C01044. (doi:10.1088/1748-0221/18/01/C01044).

[36] The Ac. 2024 Technical Design report for the ALICE Inner Tracking System 3 - ITS3 ; A bent wafer-scale monolithic pixel detector. Tech. rep., CERN, Geneva. Co-project Manager: Magnus Mager, magnus.mager@cern.chds.

[37] ITS3 Members. MOSS User Manual. `https://gitlab.cern.ch/groups/alice-its3-wp3/moss-testing/-/wikis/Moss%20user%20manual`. Accessed April 2024.

[38] ITS3 Members. MOSS Testing. `https://gitlab.cern.ch/groups/alice-its3-wp3/moss-testing/-/wikis/home`. Accessed January 2024.

[39] ITS3 Members. Getting Started with DAQ Raiser. `https://gitlab.cern.ch/groups/alice-its3-wp3/baby-moss/-/wikis/Getting-Started-with-DAQ-Raiser`. Accessed February 2024.

[40] Rudolf K Bock. Neutron Fluence. `http://arpg-serv.ing2.uniroma1.it/patera/didattica/fis_mod/trasp_riv/Glossario/node123.html`. Accessed April 2024.

[41] CERN. The Proton Synchrotron. `https://home.cern/science/accelerators/proton-synchrotron`. Accessed February 2024.

[42] Gatignon L. East Area Documentation - SBA. `http://sba.web.cern.ch/sba/beamsandareas/east/east.htm`. Accessed February 2024.

[43] Kroger J, Spannagel S, Williams M. 2024 Corryvreckan User Manual, Version 2.0 .

[44] Dannheim D, Dort K, Huth L, Hynds D, Kremastiotis I, Kröger J, Munker M, Pitters F, Schütze P, Spannagel S, *et al.* 2021 Corryvreckan: a modular 4d track reconstruction and analysis software for test beam data. *Journal of Instrumentation* **16**, 03, P03008.

[45] Brun R, Rademakers F. 1997 Root — an object oriented data analysis framework. *Nuclear Instruments and Methods in Physics Research Section A: Accelerators, Spectrometers, Detectors and Associated Equipment* **389**, 1, 81–86. (doi: https://doi.org/10.1016/S0168-9002(97)00048-X). New Computing Techniques in Physics Research V.

[46] ITS3 Members. ITS3-WP3-Approved-Plots. `https://gitlab.cern.ch/alice-its3-wp3/its3-wp3-approved-plots`. Accessed April 2024.

[47] Kachan S. 2022. Measurement errors. analysis and evaluation. https://rep.bntu.by/handle/data/126047. Accessed April 2024.

Appendix

A Examples of residuals from the Corryvreckan analysis for -0.3 V reverse bias

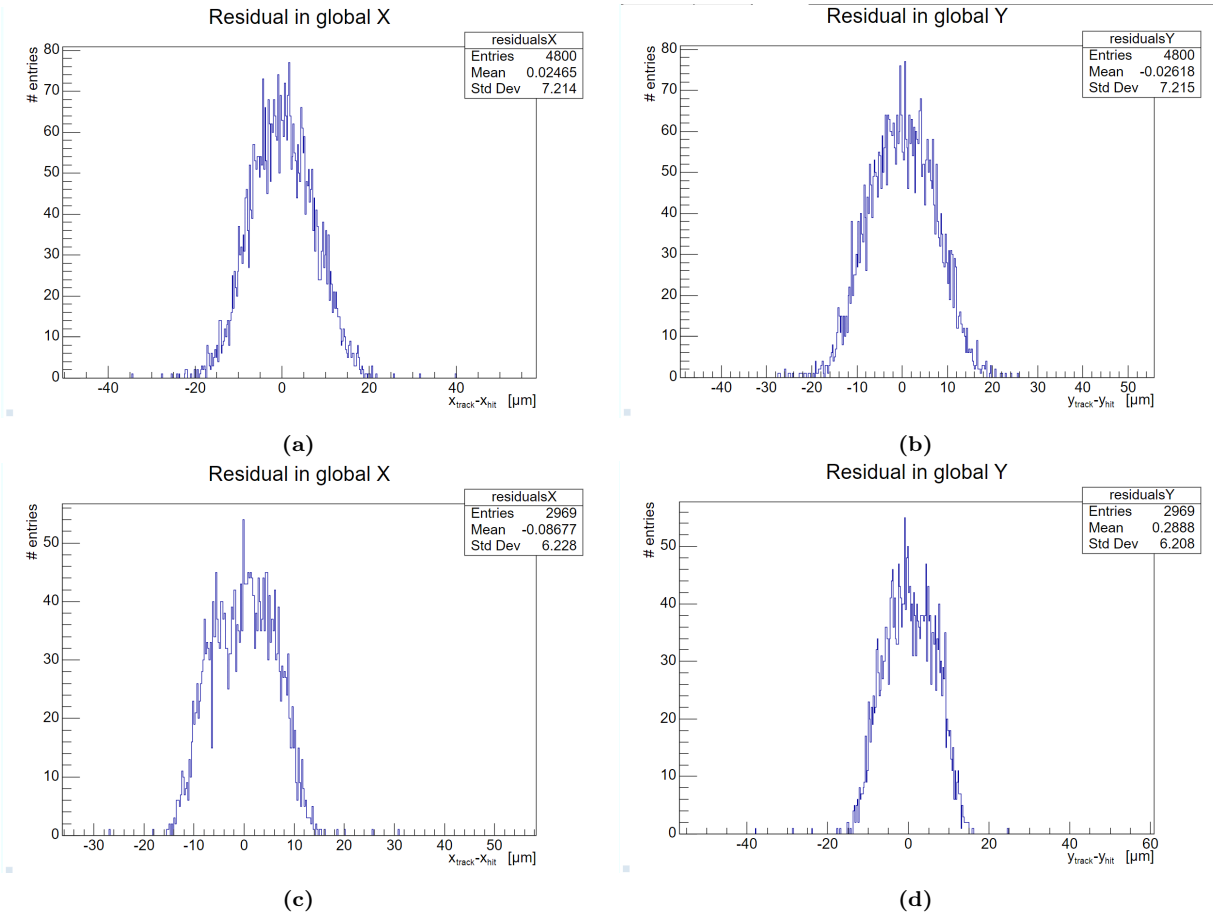

Figure 29. Figures produced by the author. In (a) and (c) are the residuals of region 0 in X and Y global system, respectively, while in (b) and (d) are the ones of region 1, X and Y global system, respectively. The plots are obtained from the Corryvreckan analysis during the test beam with babyMOSS-1_1_W24B5, for a reverse bias of -0.3 V.

B Plots from the MOSS test beam in September

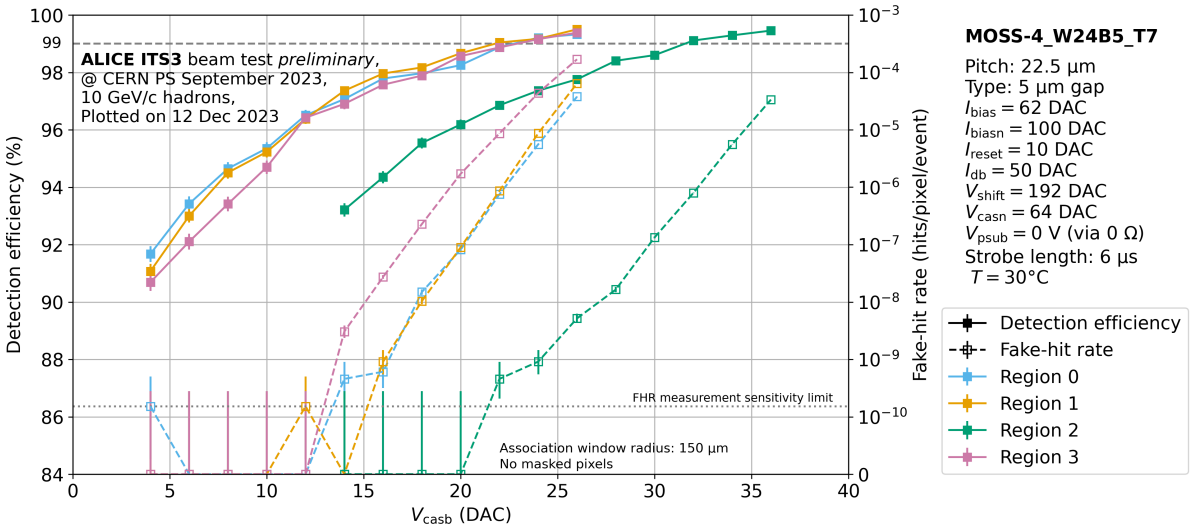

Figure 30. Detection efficiency (solid lines) and fake-hit rate (dashed lines) for different V_{casb} values from the September test beam, for MOSS − 4_W24B5 top HU 7. Region 0 is with blue color, region 1 with yellow, region 2 with green and region 3 with pink [46].

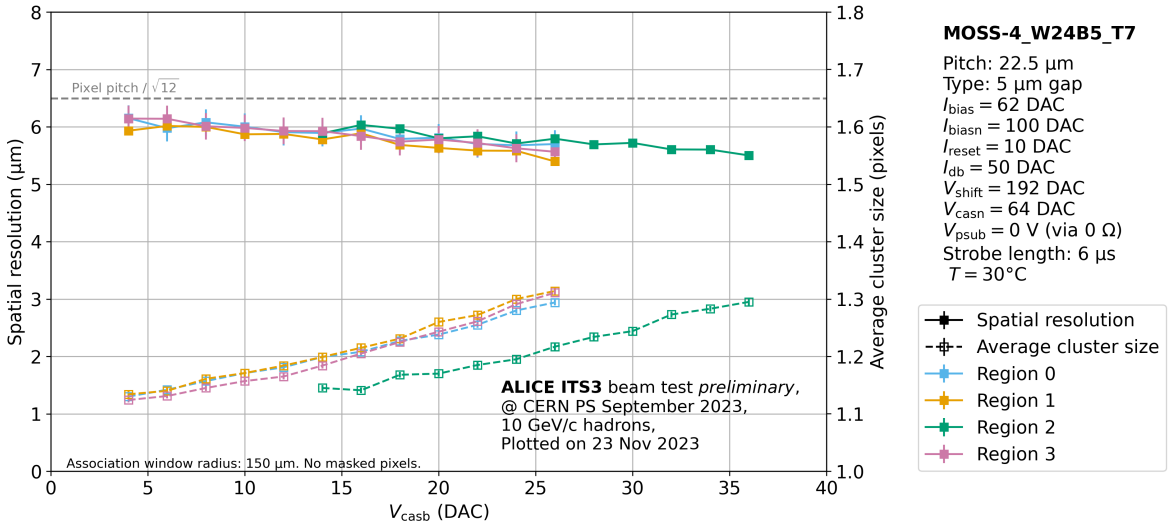

Figure 31. Spatial resolution (solid lines) and average cluster size (dashed lines) for different V_{casb} values from the September test beam, for MOSS − 4_W24B5 top HU 7. Region 0 is with blue color, region 1 with yellow, region 2 with green and region 3 with pink [46].

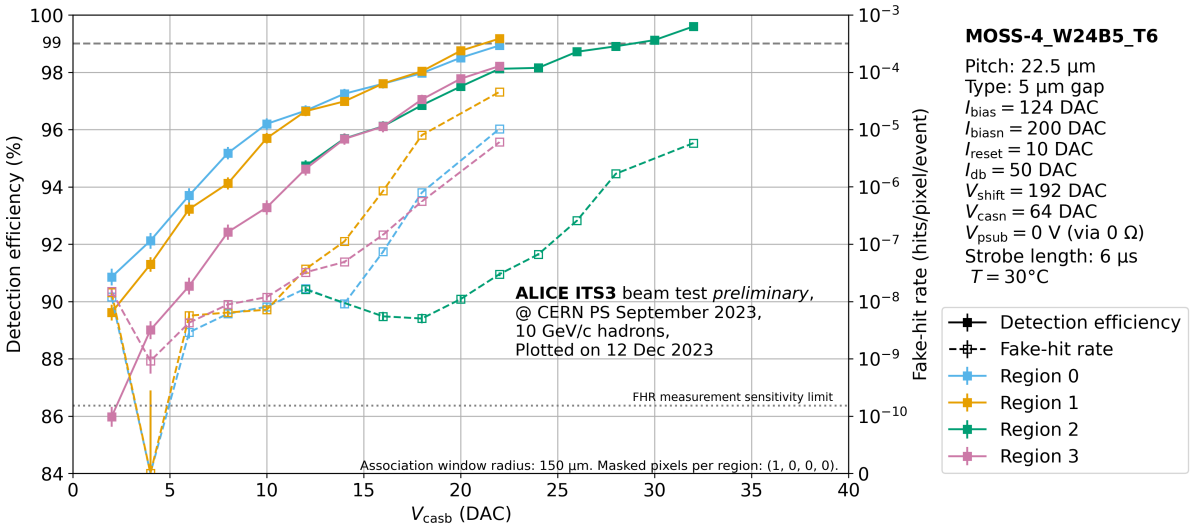

Figure 32. Detection efficiency (solid lines) and fake-hit rate (dashed lines) for different V_{casb} values from the September test beam, for MOSS – 4_W24B5 top HU 6, with higher I_{bias} and I_{biasn}. Region 0 is with blue color, region 1 with yellow, region 2 with green and region 3 with pink [46].

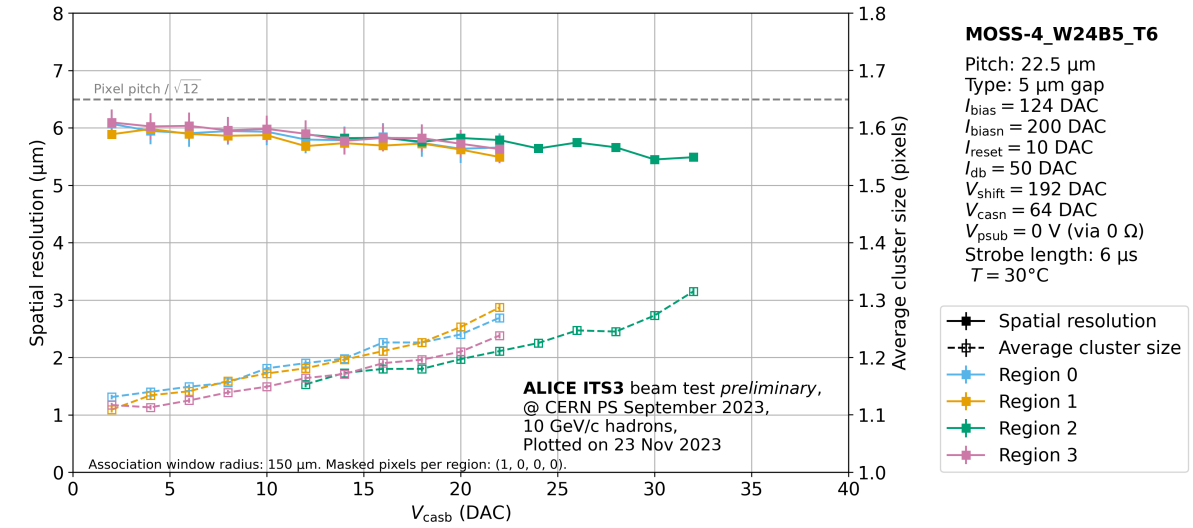

Figure 33. Spatial resolution (solid lines) and average cluster size (dashed lines) for different V_{casb} values from the September test beam, for MOSS – 4_W24B5 top HU 6, with higher I_{bias} and I_{biasn}. Region 0 is with blue color, region 1 with yellow, region 2 with green and region 3 with pink [46].

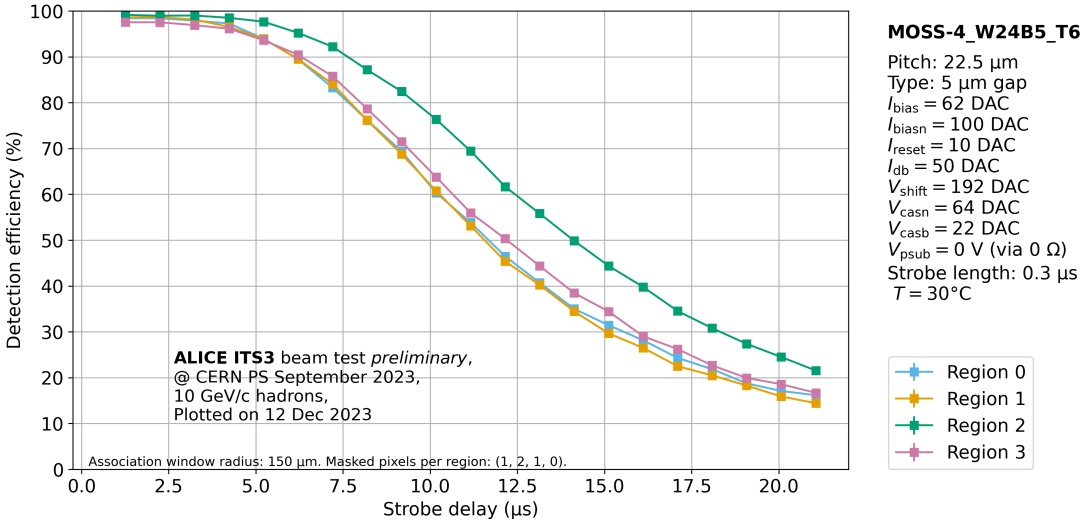

Figure 34. Detection efficiency (solid lines) as a function of strobe delay from the September test beam, for MOSS − 4_W24B5 top HU 6. Region 0 is with blue color, region 1 with yellow, region 2 with green and region 3 with pink [46].

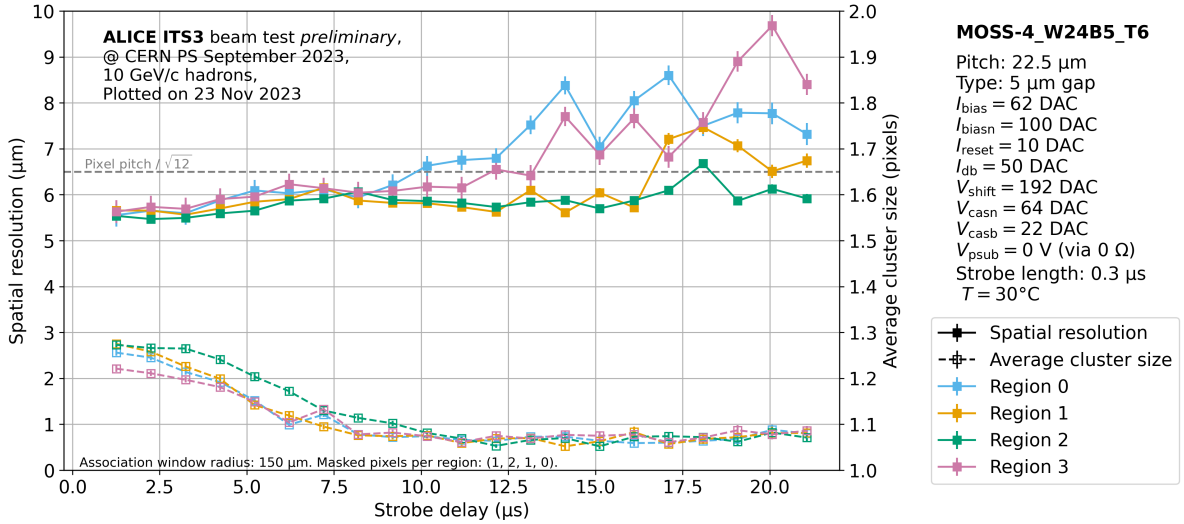

Figure 35. Spatial resolution (solid lines) and average cluster size (dashed lines) for different strobe delay values from the September test beam, for MOSS − 4_W24B5 top HU 6. Region 0 is with blue color, region 1 with yellow, region 2 with green and region 3 with pink [46].

C Plots from the babyMOSS test beam in October

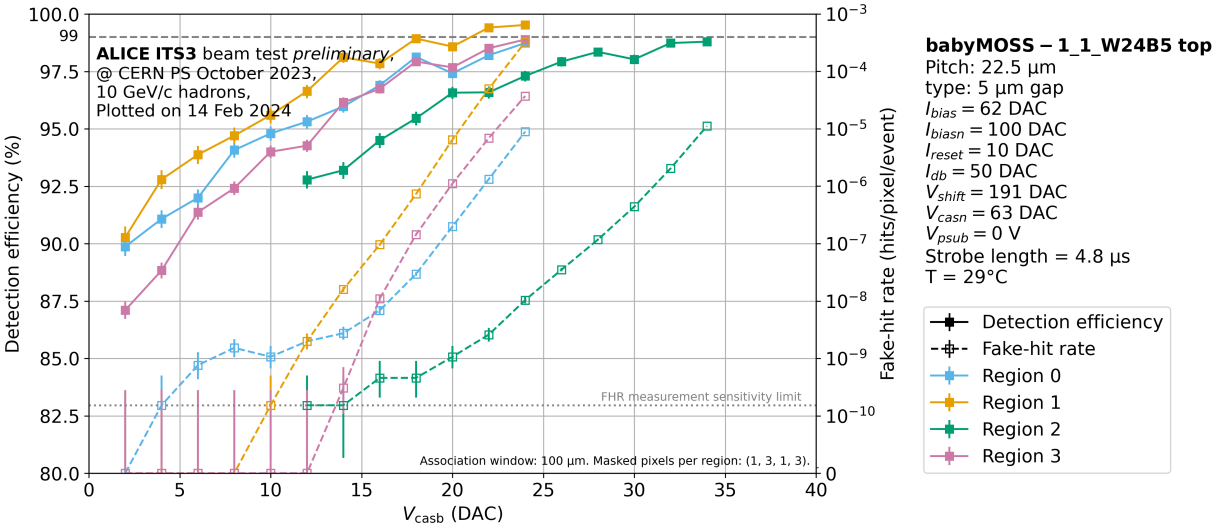

Figure 36. Detection efficiency (solid lines) and fake-hit rate (dashed lines) for different V_{casb} values from the October test beam with babyMOSS-1_1_W24B5, with fixed reverse bias at 0 V, for all the regions. Figure produced by the author.

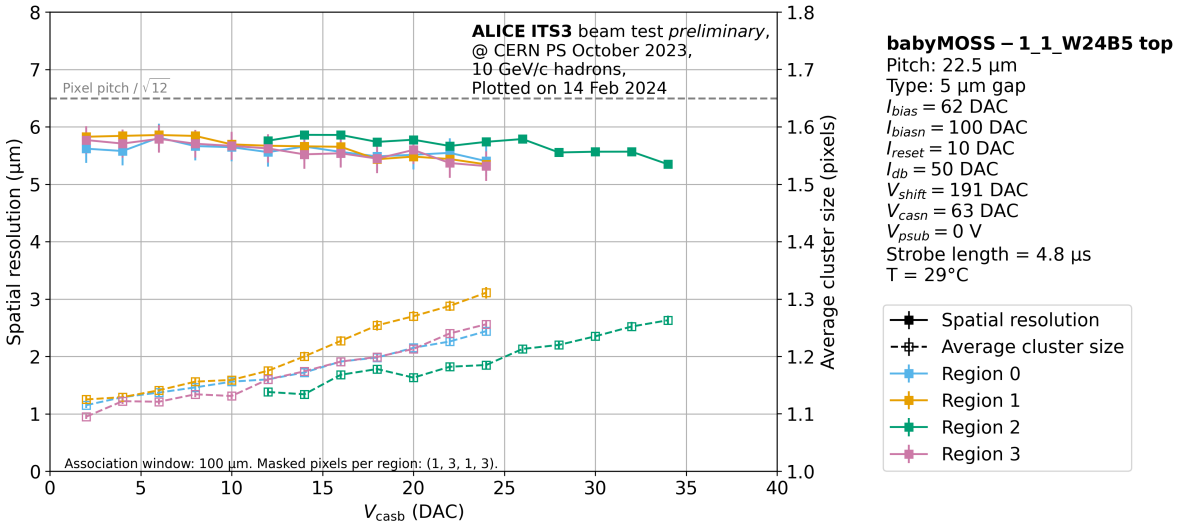

Figure 37. Spatial resolution (solid lines) and average cluster size (dashed lines) for different V_{casb} values from the October test beam with babyMOSS-1_1_W24B5, with fixed reverse bias at 0 V, for all the regions. Figure produced by the author.

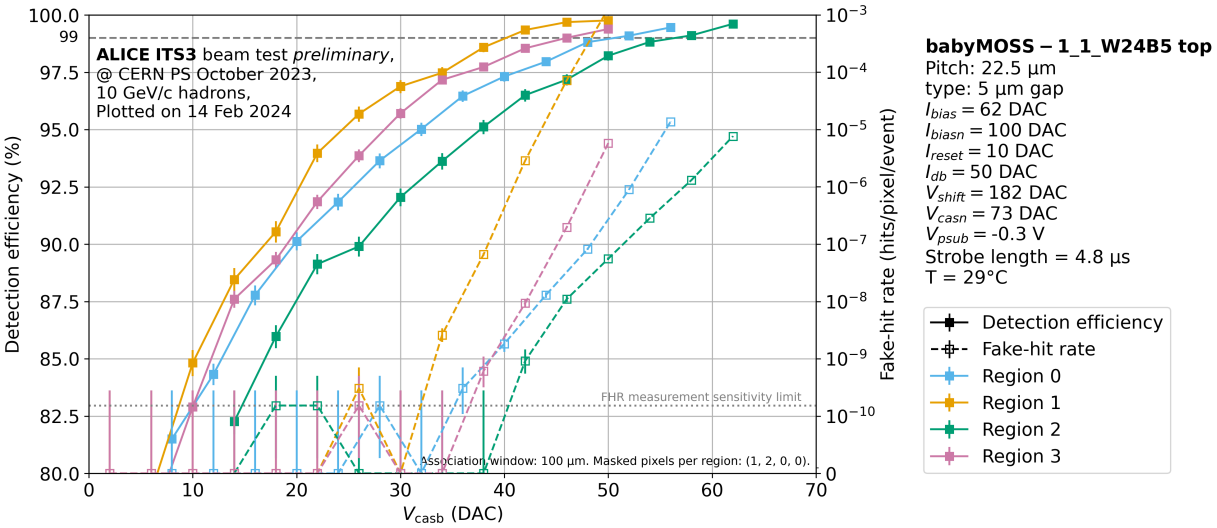

Figure 38. Detection efficiency (solid lines) and fake-hit rate (dashed lines) for different V_{casb} values from the October test beam with babyMOSS-1_1_W24B5, with fixed reverse bias at -0.3 V, for all the regions. Figure produced by the author.

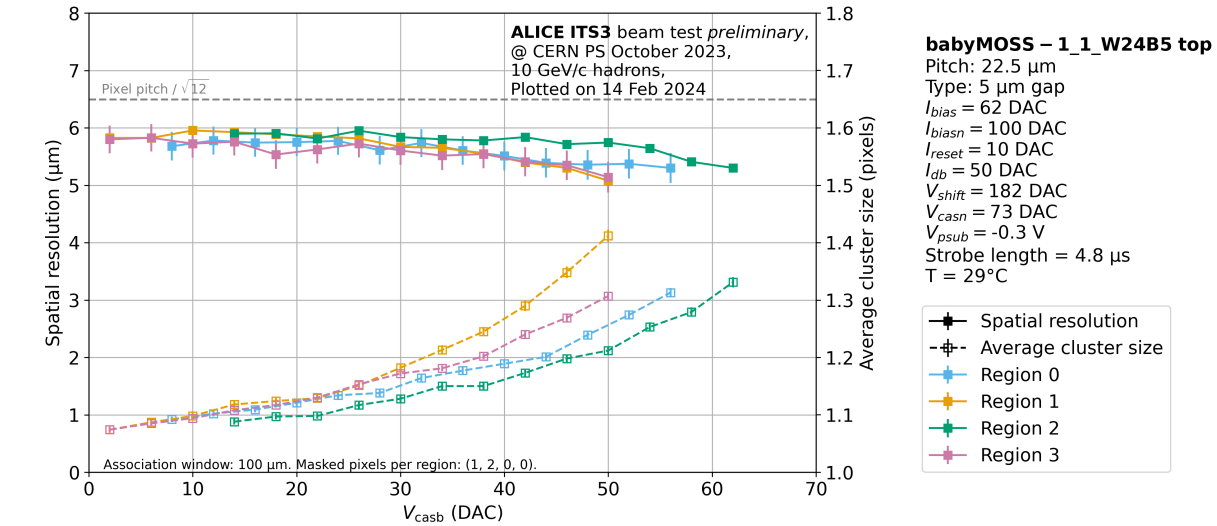

Figure 39. Spatial resolution (solid lines) and average cluster size (dashed lines) for different V_{casb} values from the October test beam with babyMOSS-1_1_W24B5, with fixed reverse bias at -0.3 V, for all the regions. Figure produced by the author.

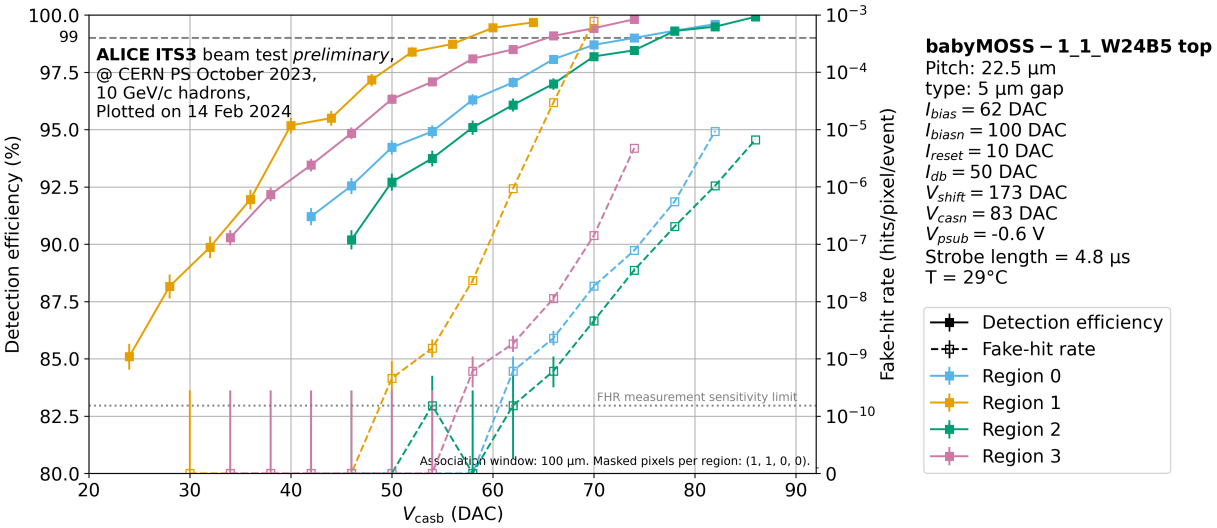

Figure 40. Detection efficiency (solid lines) and fake-hit rate (dashed lines) for different V_{casb} values from the October test beam with babyMOSS-1_1_W24B5, with fixed reverse bias at -0.6 V, for all the regions. Figure produced by the author.

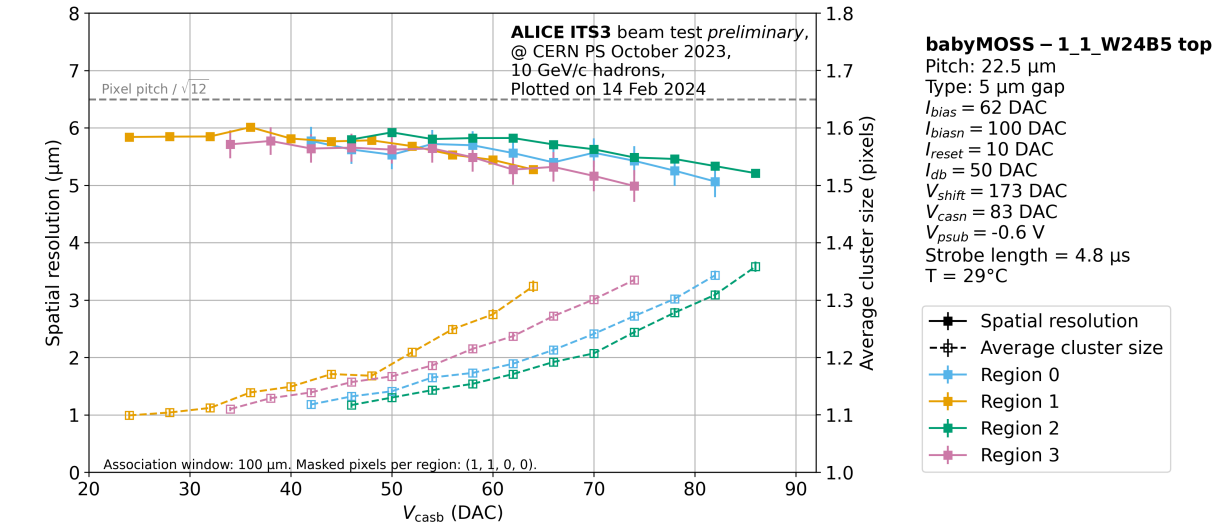

Figure 41. Spatial resolution (solid lines) and average cluster size (dashed lines) for different V_{casb} values from the October test beam with babyMOSS-1_1_W24B5, with fixed reverse bias at -0.6 V, for all the regions. Figure produced by the author.

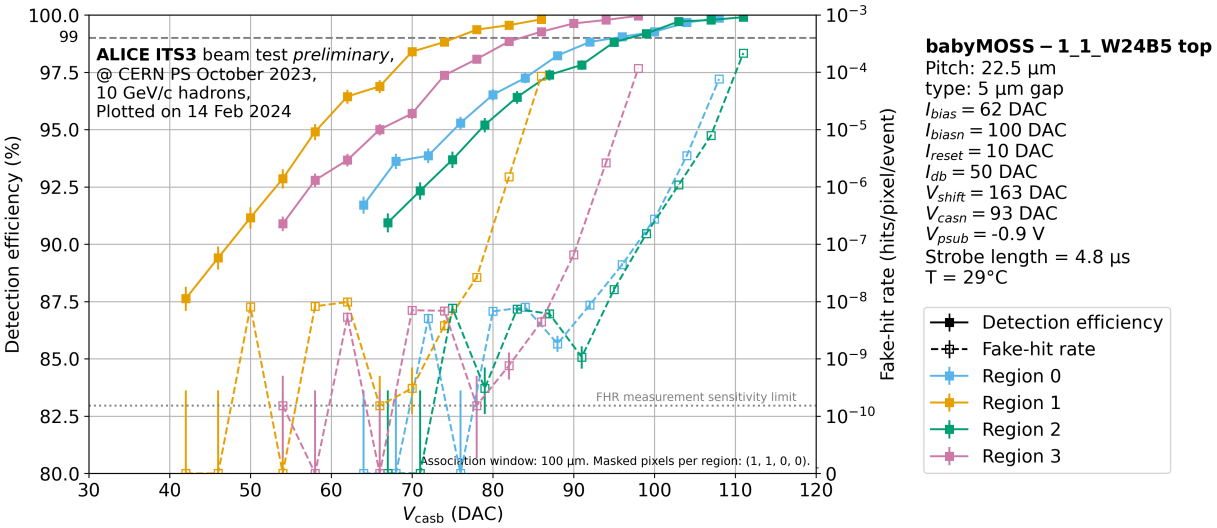

Figure 42. Detection efficiency (solid lines) and fake-hit rate (dashed lines) for different V_{casb} values from the October test beam with babyMOSS-1_1_W24B5, with fixed reverse bias at -0.9 V, for all the regions. Figure produced by the author.

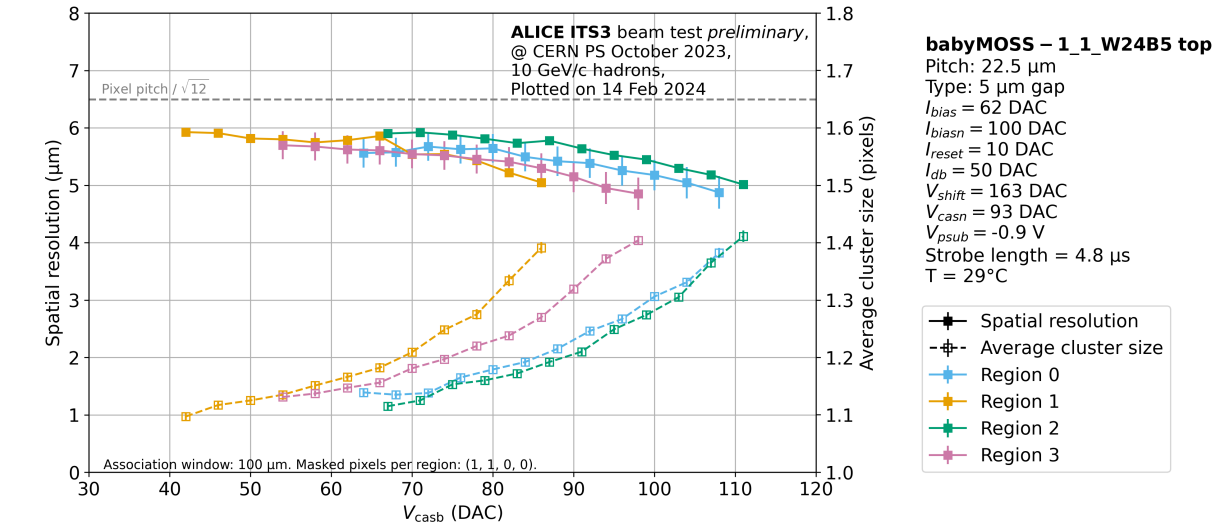

Figure 43. Spatial resolution (solid lines) and average cluster size (dashed lines) for different V_{casb} values from the October test beam with babyMOSS-1_1_W24B5, with fixed reverse bias at -0.9 V, for all the regions. Figure produced by the author.

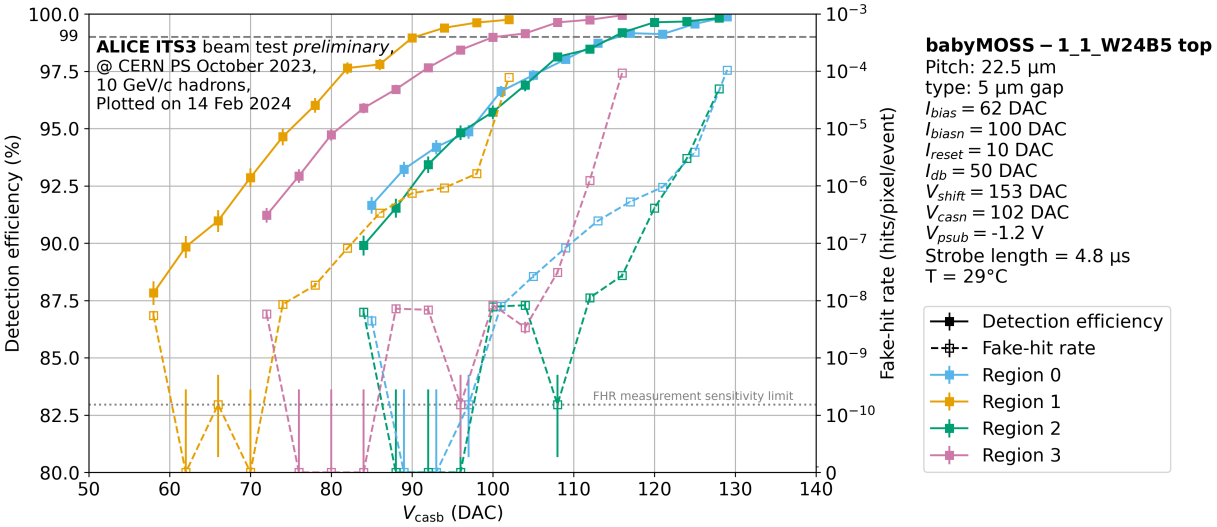

Figure 44. Detection efficiency (solid lines) and fake-hit rate (dashed lines) for different V_{casb} values from the October test beam with babyMOSS-1_1_W24B5, with fixed reverse bias at -1.2 V, for all the regions. Figure produced by the author.

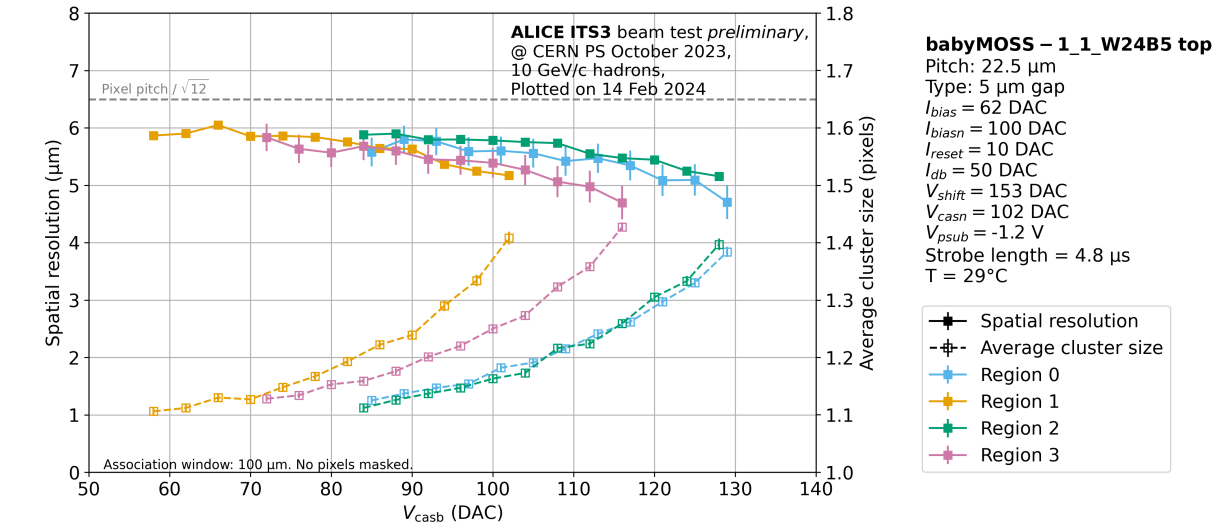

Figure 45. Spatial resolution (solid lines) and average cluster size (dashed lines) for different V_{casb} values from the October test beam with babyMOSS-1_1_W24B5, with fixed reverse bias at -1.2 V, for all the regions. Figure produced by the author.

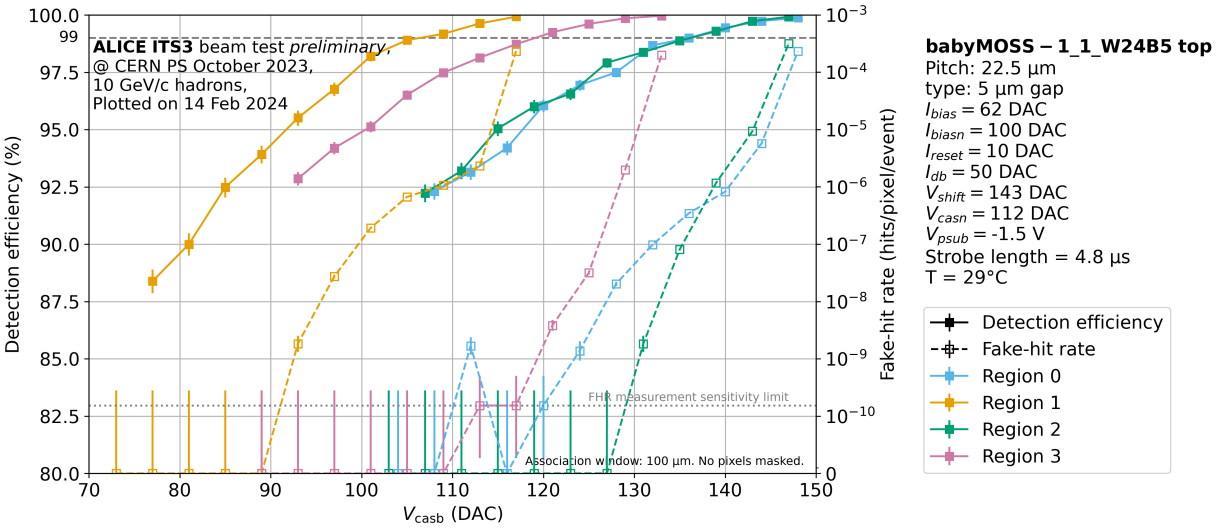

Figure 46. Detection efficiency (solid lines) and fake-hit rate (dashed lines) for different V_{casb} values from the October test beam with babyMOSS-1_1_W24B5, with fixed reverse bias at -1.5 V, for all the regions. Figure produced by the author.

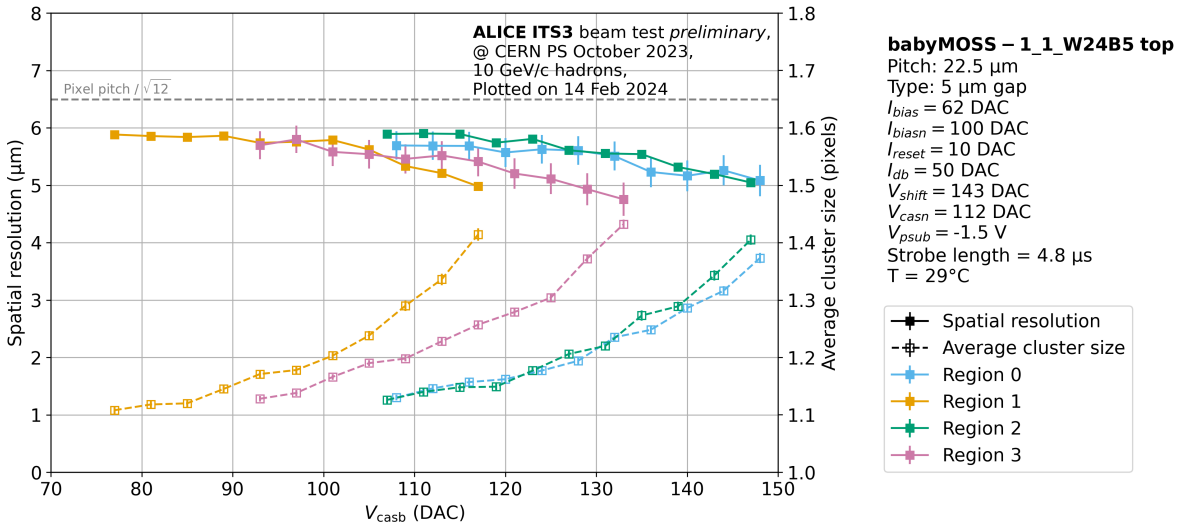

Figure 47. Spatial resolution (solid lines) and average cluster size (dashed lines) for different V_{casb} values from the October test beam with babyMOSS-1_1_W24B5, with fixed reverse bias at -1.5 V, for all the regions. Figure produced by the author.

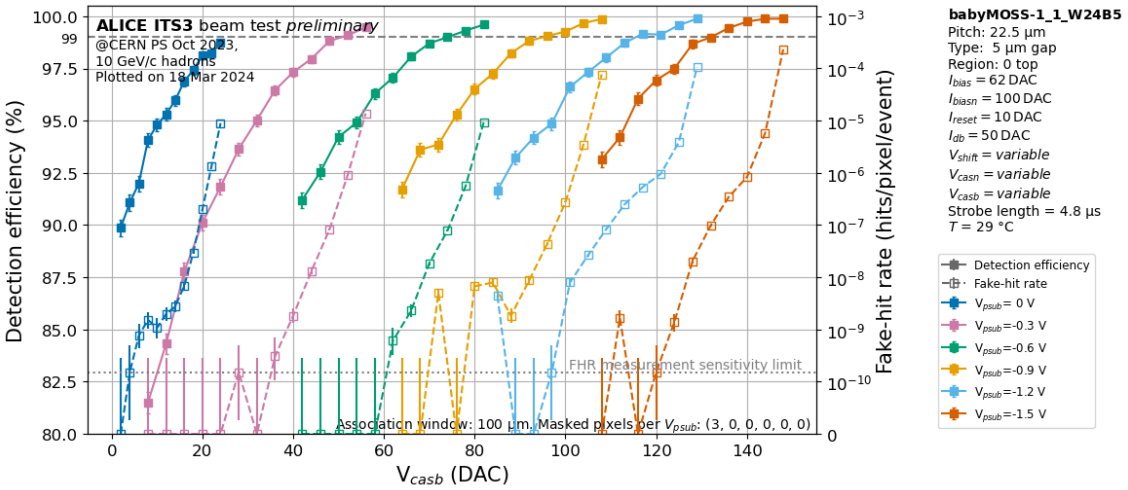

Figure 48. Detection efficiency (solid lines) and fake-hit rate (dashed lines) for different V_{casb} values from the October test beam with babyMOSS-1_1_W24B5, with fixed region 0 and variable reverse bias. Figure produced by the author.

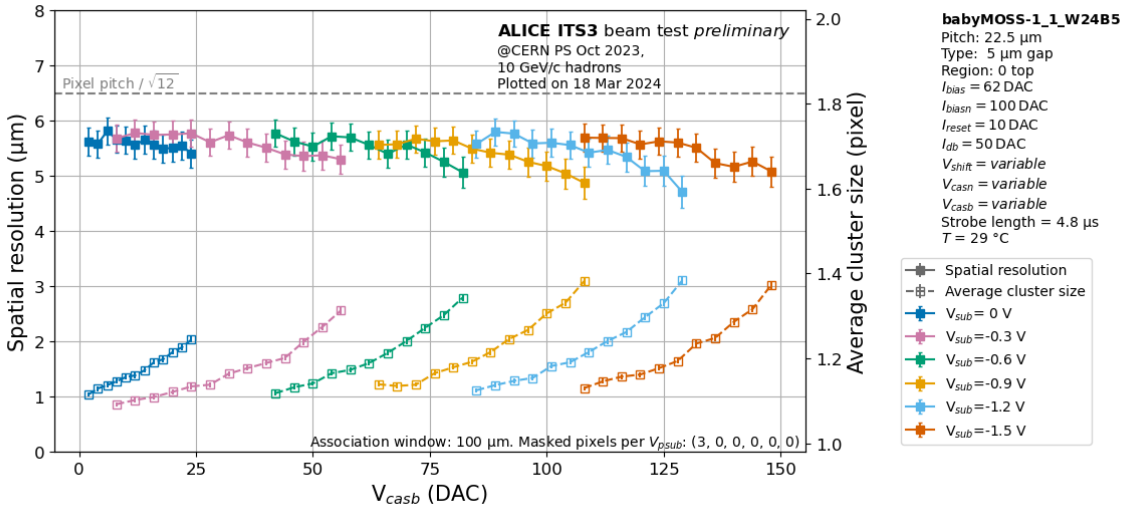

Figure 49. Spatial resolution (solid lines) and average cluster size (dashed lines) for different V_{casb} values from the October test beam with babyMOSS-1_1_W24B5, with fixed region 0 and variable reverse bias. Figure produced by the author.

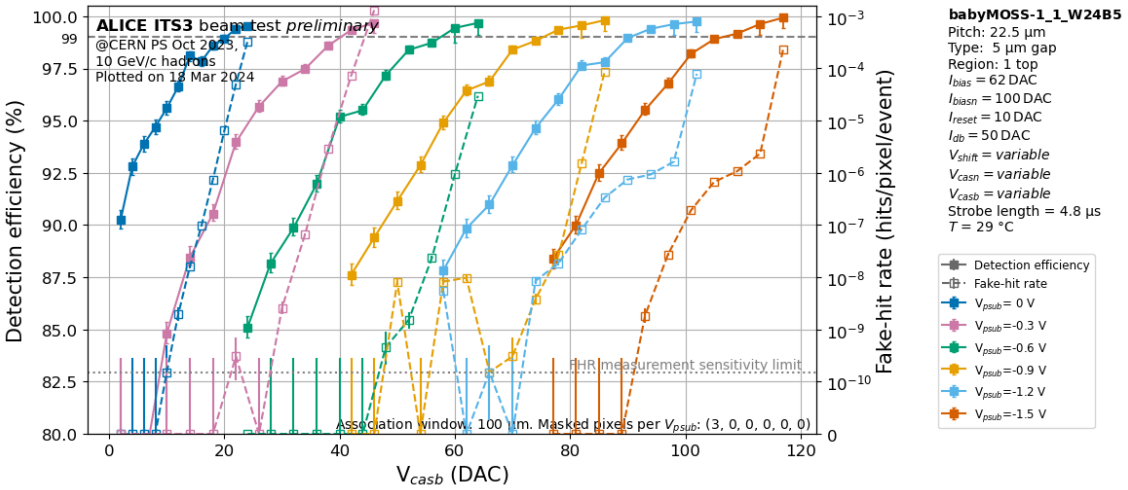

Figure 50. Detection efficiency (solid lines) and fake-hit rate (dashed lines) for different V_{casb} values from the October test beam with babyMOSS-1_1_W24B5, with fixed region 1 and variable reverse bias. Figure produced by the author.

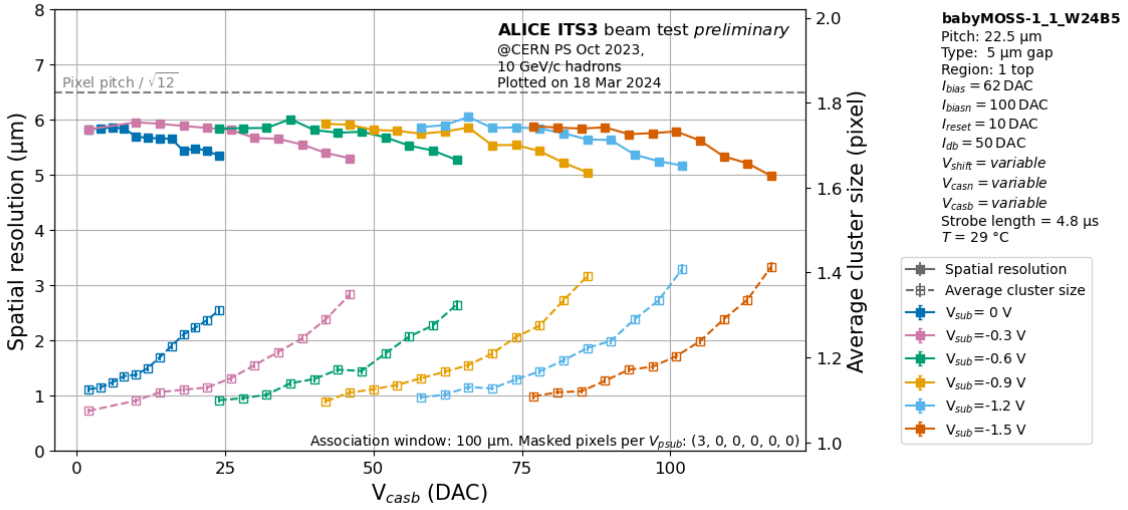

Figure 51. Spatial resolution (solid lines) and average cluster size (dashed lines) for different V_{casb} values from the October test beam with babyMOSS-1_1_W24B5, with fixed region 1 and variable reverse bias. Figure produced by the author.

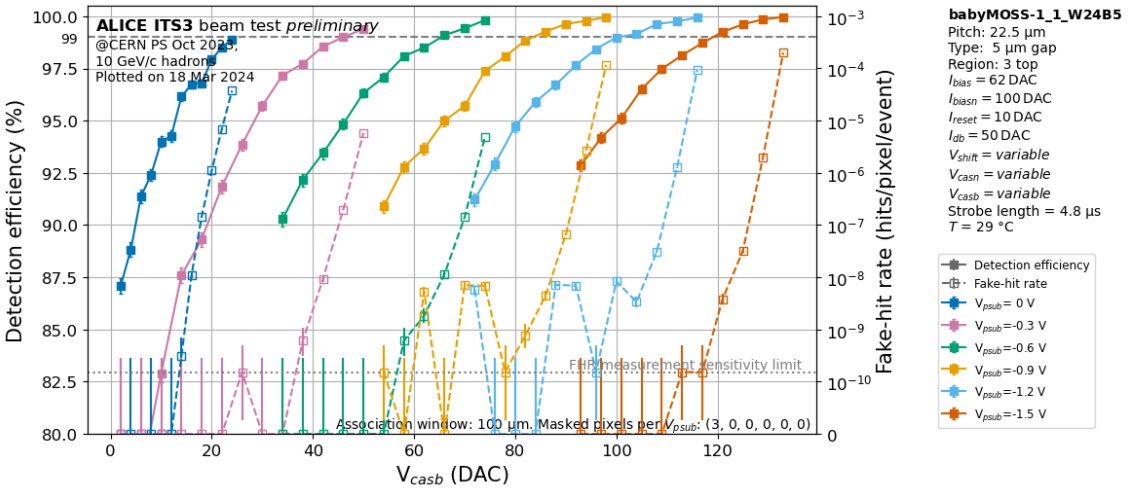

Figure 52. Detection efficiency (solid lines) and fake-hit rate (dashed lines) for different V_{casb} values from the October test beam with babyMOSS-1_1_W24B5, with fixed region 3 and variable reverse bias. Figure produced by the author.

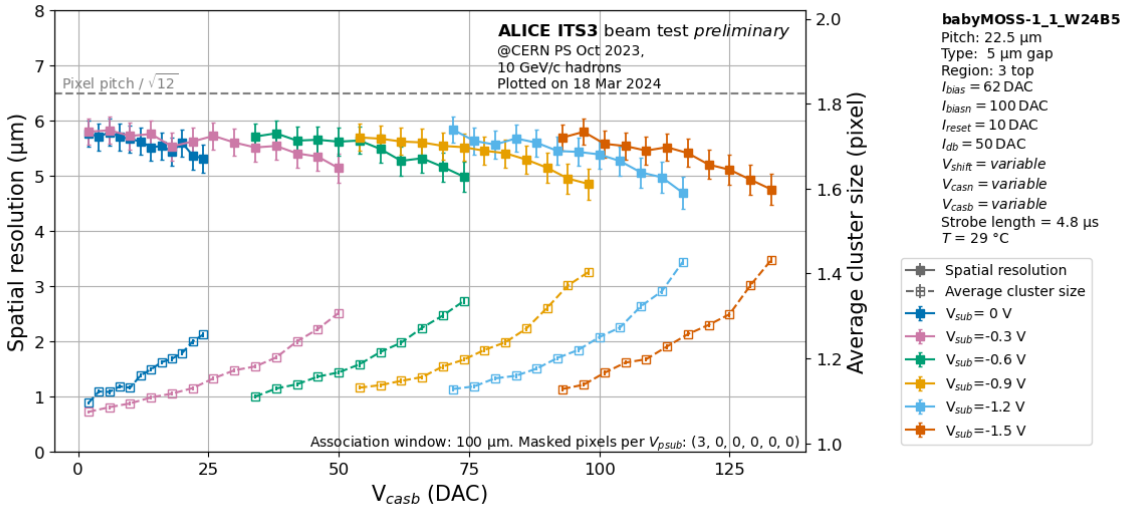

Figure 53. Spatial resolution (solid lines) and average cluster size (dashed lines) for different V_{casb} values from the October test beam with babyMOSS-1_1_W24B5, with fixed region 3 and variable reverse bias. Figure produced by the author.

D FHR and THR as functions of V_{shift} for top regions 0 and 1

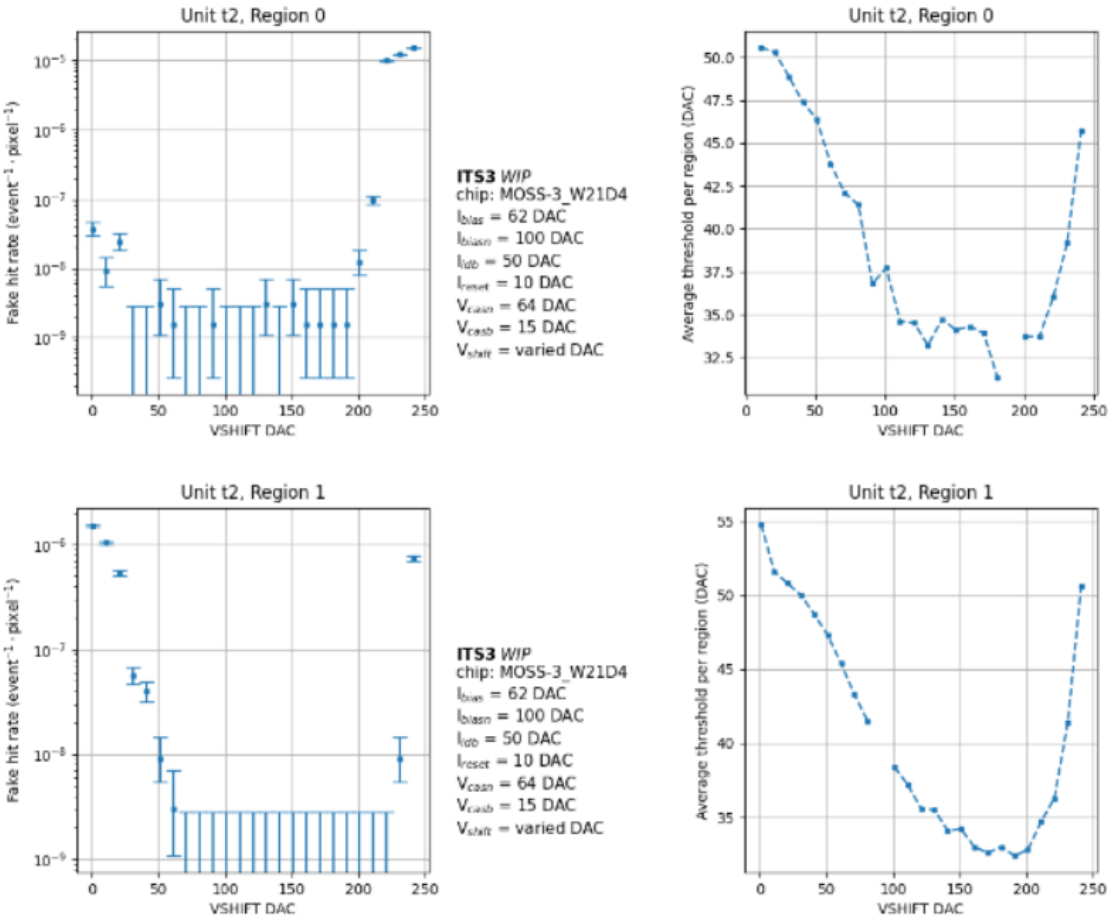

Figure 54. On the left is fake hit rate as a function of V_{shift} in DAC units and on the right side the average threshold per region as a function of V_{shift} in DAC units. All plots are for top HU 2, with the plots on top with region 0 and the bottom ones with region 1 of MOSS-3_W21D4. Figures produced by the test beam team.

E Example of correlations from the testing of region 1 with reverse bias applied

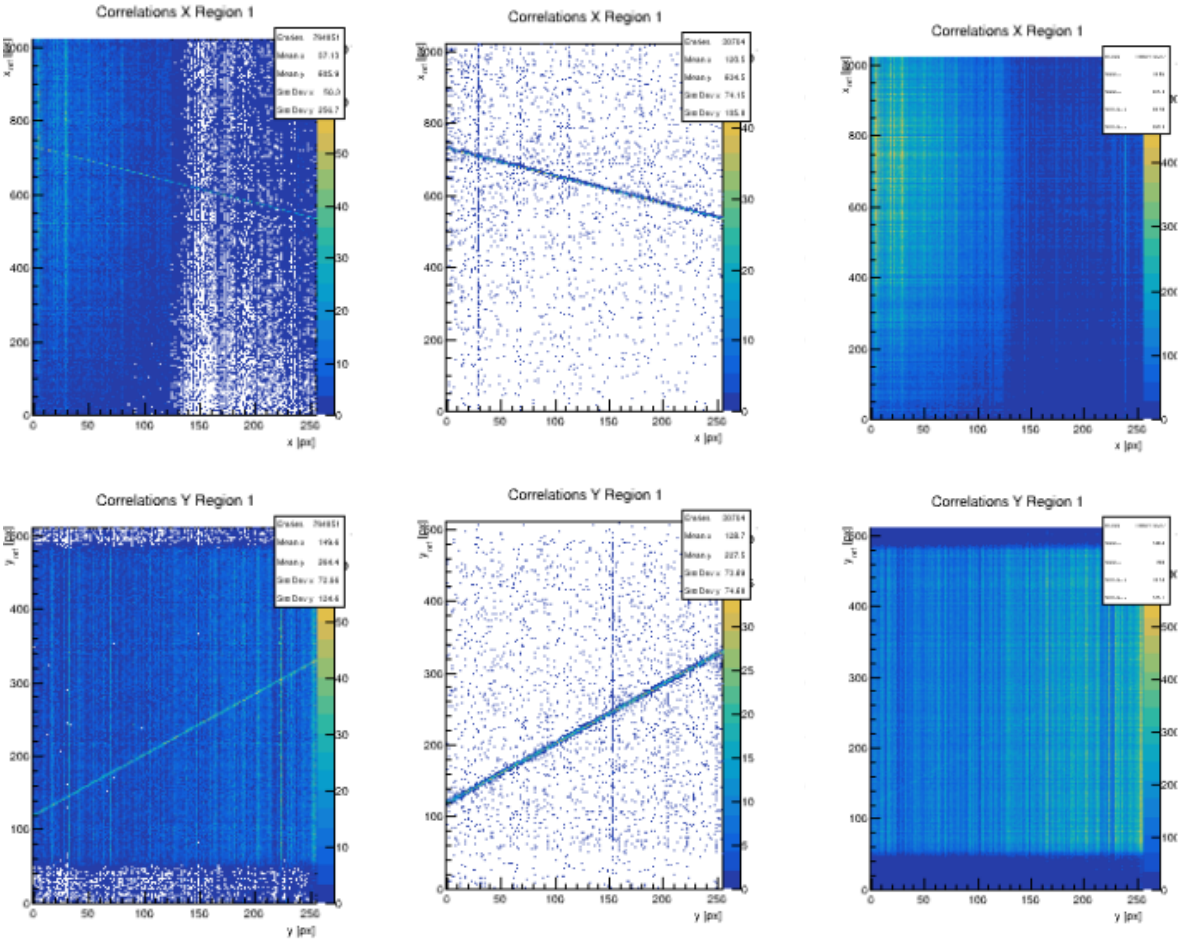

(a) (b) (c)

Figure 55. Correlation of X and Y for the scan of region 1 with reverse bias -1.2 V. In (a) are the correlations for V_{casb} 90 DAC, in (b) are the correlations for V_{casb} 92 DAC and in (c), the correlations for V_{casb} 94 DAC. Even though the noise should be increasing, as V_{casb} increases, for a V_{casb} of 92 DAC the correlations seem much less noisy, explaining the drop in efficiency that was observed in the efficiency plot, for this V_{casb} value. Figures produced by the author.

F Spatial resolution plots for irradiated babyMOSS

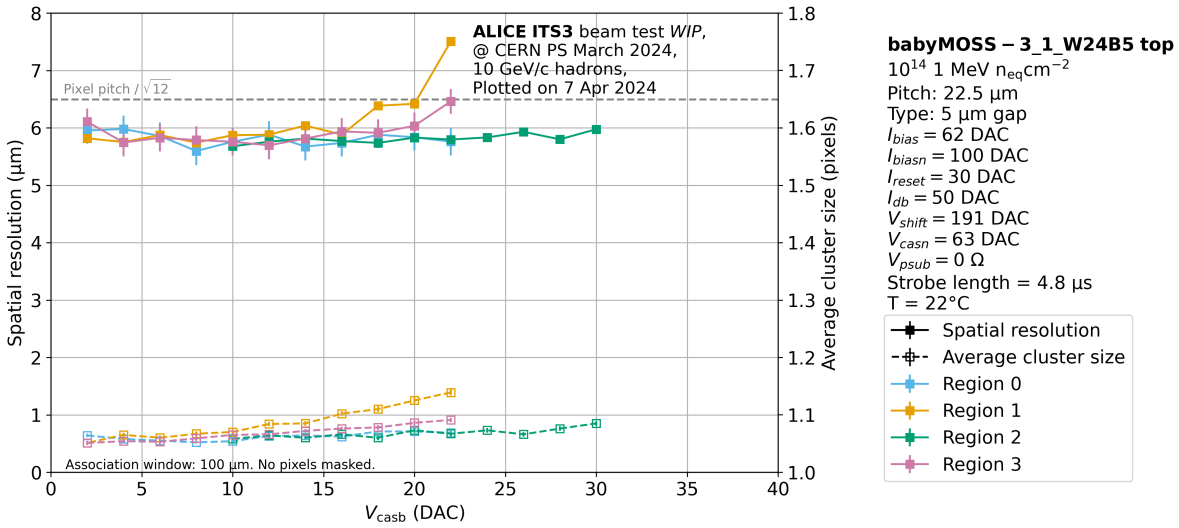

Figure 56. Spatial resolution (solid lines) and average cluster size (dashed lines) for different V_{casb} values from the March test beam with the irradiated babyMOSS-3_1_W24B5, with grounded reverse bias and for all regions. Figure produced by the author.

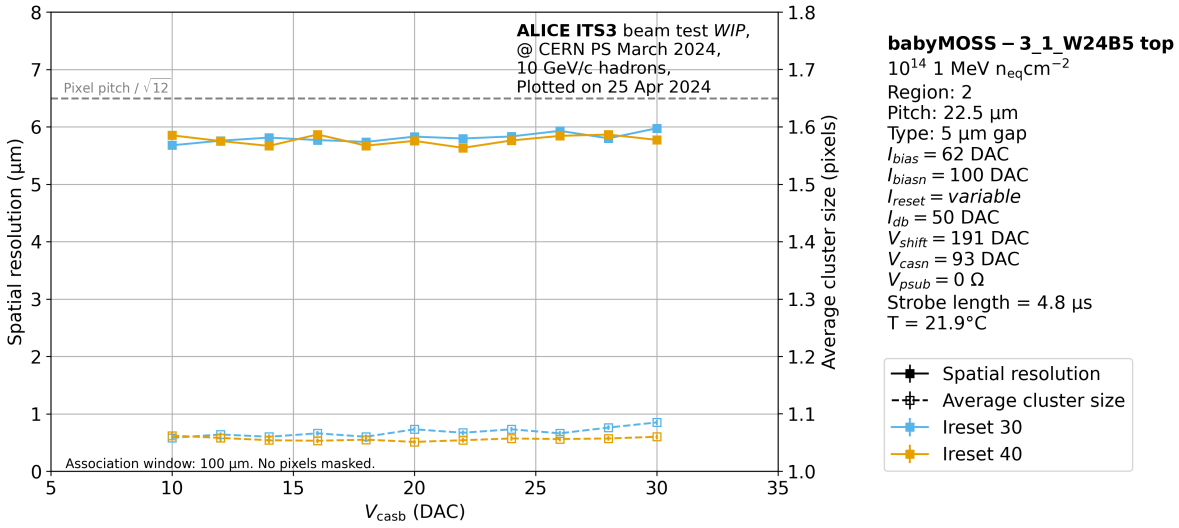

Figure 57. Spatial resolution (solid lines) and average cluster size (dashed lines) for different V_{casb} values from the March test beam with the irradiated babyMOSS-3_1_W24B5, with grounded reverse bias and different I_{reset} values. Figure produced by the author.

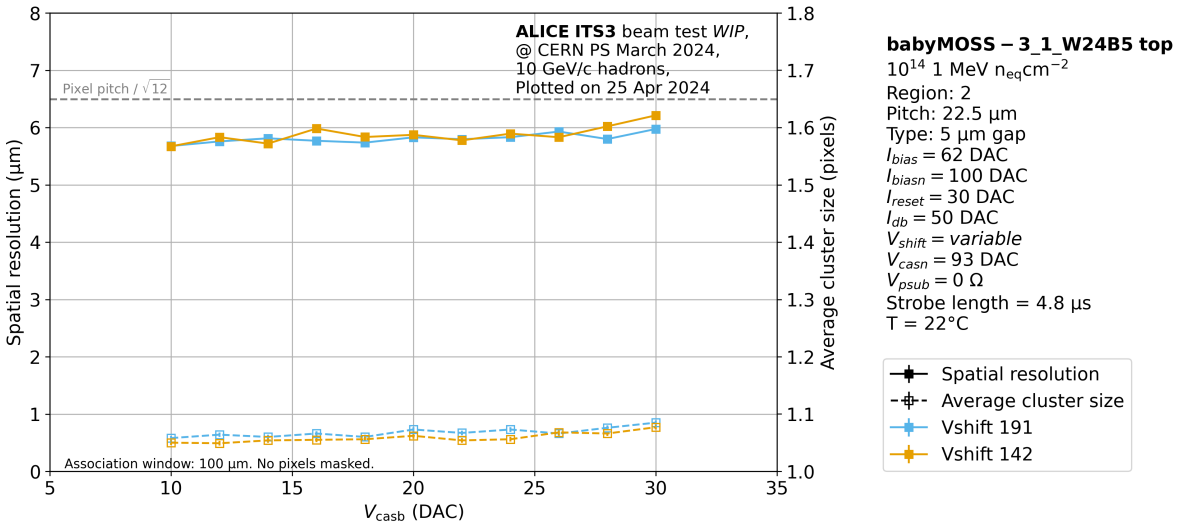

Figure 58. Spatial resolution (solid lines) and average cluster size (dashed lines) for different V_{casb} values from the March test beam with the irradiated babyMOSS-3_1_W24B5, with grounded reverse bias and different V_{shift} values. Figure produced by the author.

G DAC scans on babyMOSS with raiser board setup

Example of the scan of the 8 DACs included in the ALPIDE DAQ board, with the software that was built during this thesis, and by using the new testing system for babyMOSS that includes the raiser board. The 8 DACs are the 8 basic parameters in the analog front-end in-pixel circuitry. In this example, both HUs of babyMOSS-4_6_W24B5 were tested and the results show that the babyMOSS operates at nominal values.

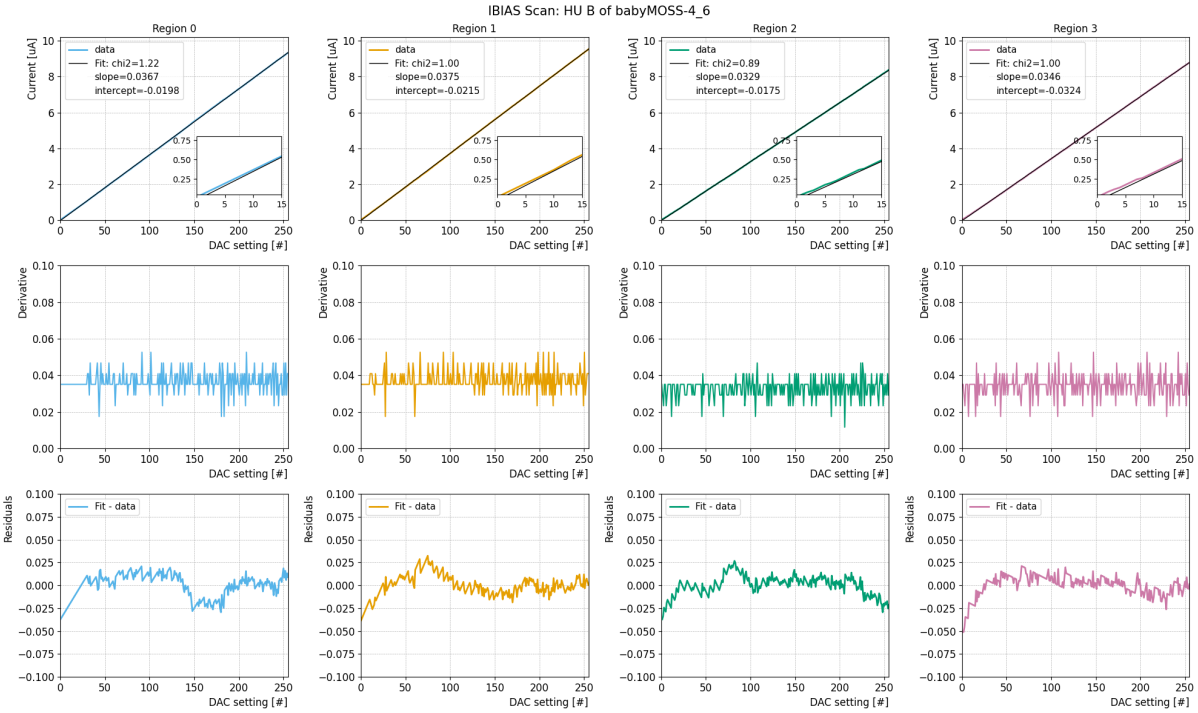

Figure 59. I_{bias} scan of bottom HU from babyMOSS-4_6_W24B5. All top plots are current plots, the middle plots are the derivatives and the bottom plots are the residuals. Region 0 is depicted with blue color, region 1 with yellow, region 2 with green and region 3 with pink. Figure produced by the author with the dac_scan.py script created.

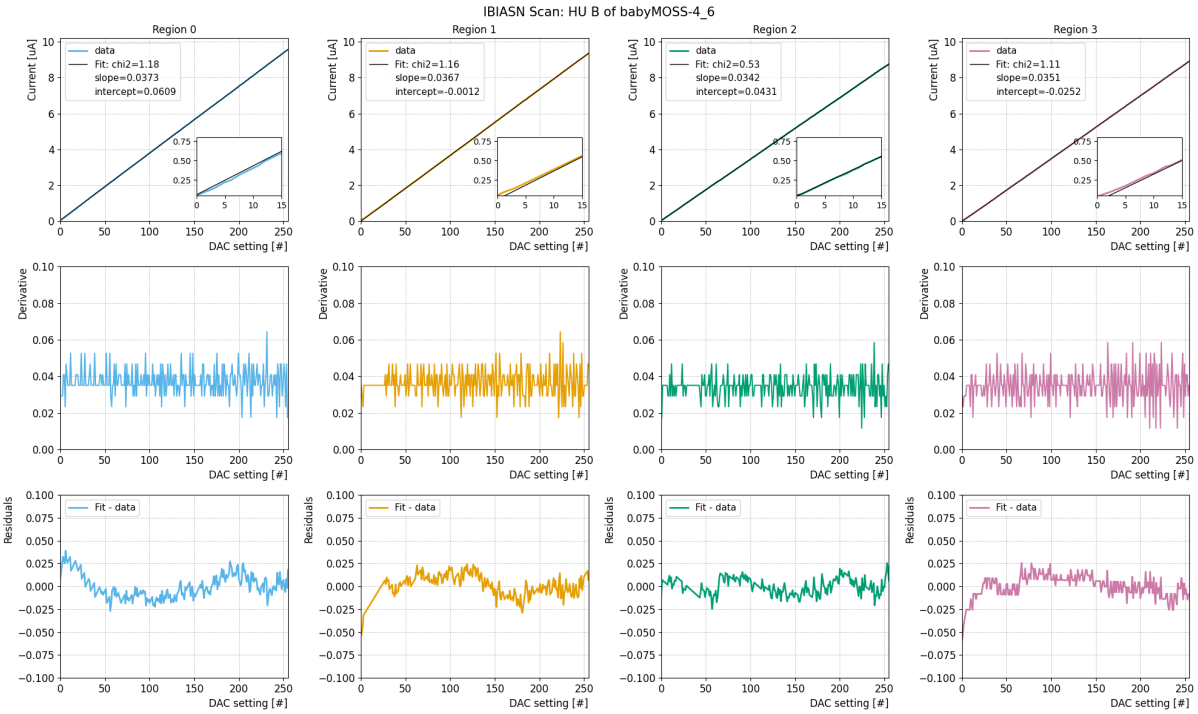

Figure 60. I_{biasn} scan of bottom HU from babyMOSS-4_6_W24B5. All top plots are current plots, the middle plots are the derivatives and the bottom plots are the residuals. Region 0 is depicted with blue color, region 1 with yellow, region 2 with green and region 3 with pink. Figure produced by the author with the dac_scan.py script created.

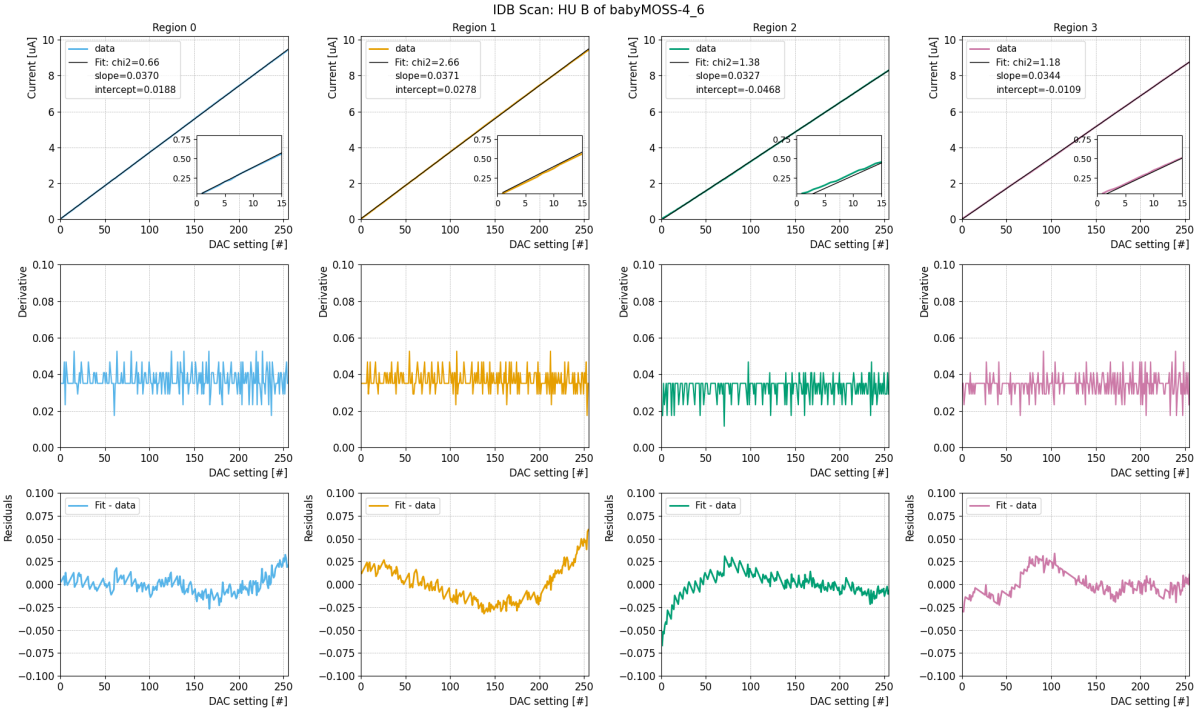

Figure 61. I_{db} scan of bottom HU from babyMOSS-4_6_W24B5. All top plots are current plots, the middle plots are the derivatives and the bottom plots are the residuals. Region 0 is depicted with blue color, region 1 with yellow, region 2 with green and region 3 with pink. Figure produced by the author with the dac_scan.py script created.

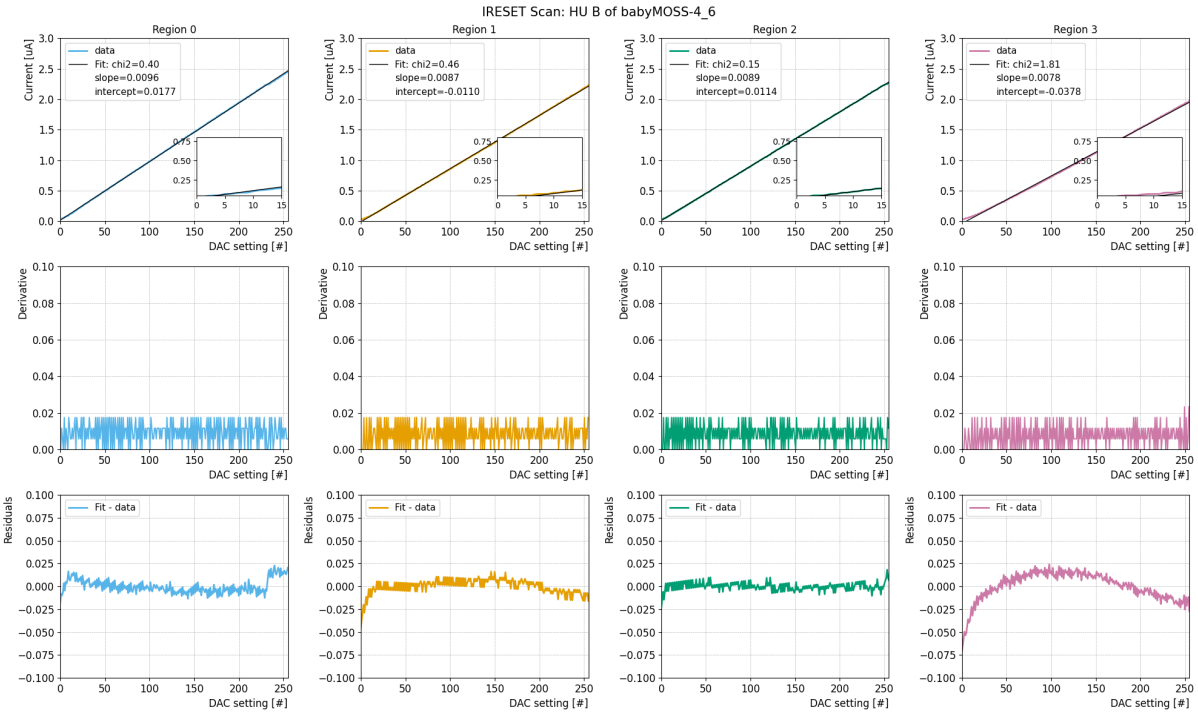

Figure 62. I_{reset} scan of bottom HU from babyMOSS-4_6_W24B5. All top plots are current plots, the middle plots are the derivatives and the bottom plots are the residuals. Region 0 is depicted with blue color, region 1 with yellow, region 2 with green and region 3 with pink. Figure produced by the author with the dac_scan.py script created.

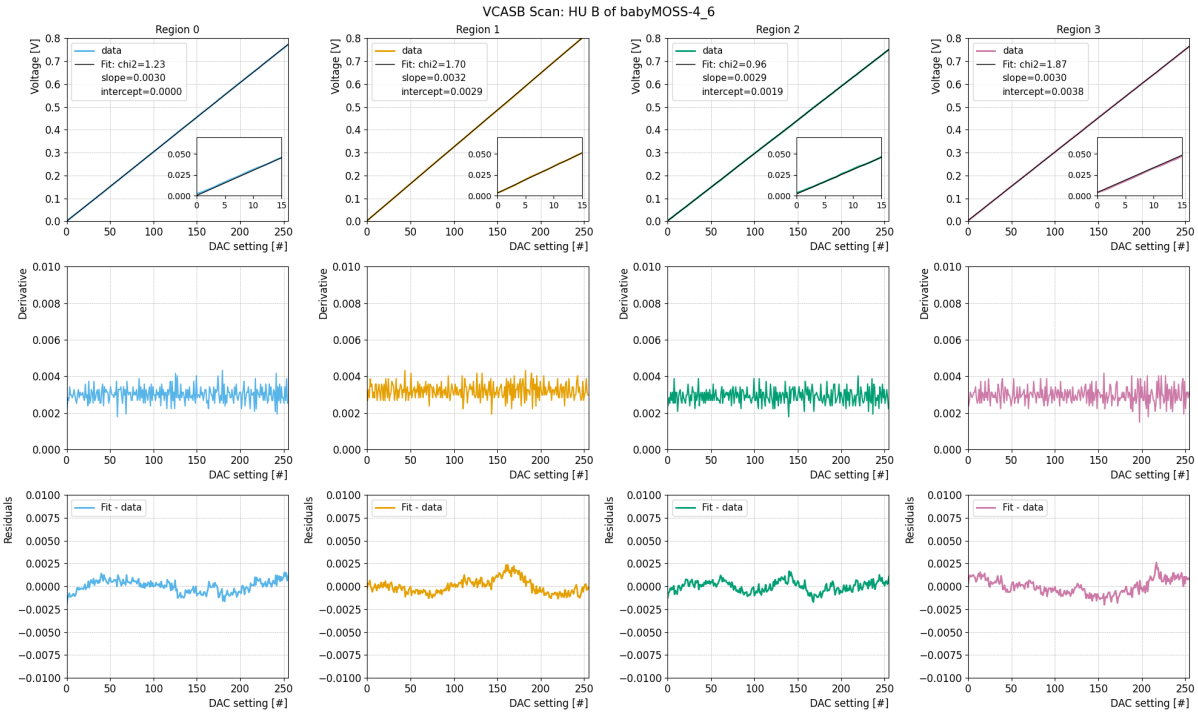

Figure 63. V_{casb} scan of bottom HU from babyMOSS-4_6_W24B5. All top plots are voltage plots, the middle plots are the derivatives and the bottom plots are the residuals. Region 0 is depicted with blue color, region 1 with yellow, region 2 with green and region 3 with pink. Figure produced by the author with the dac_scan.py script created.

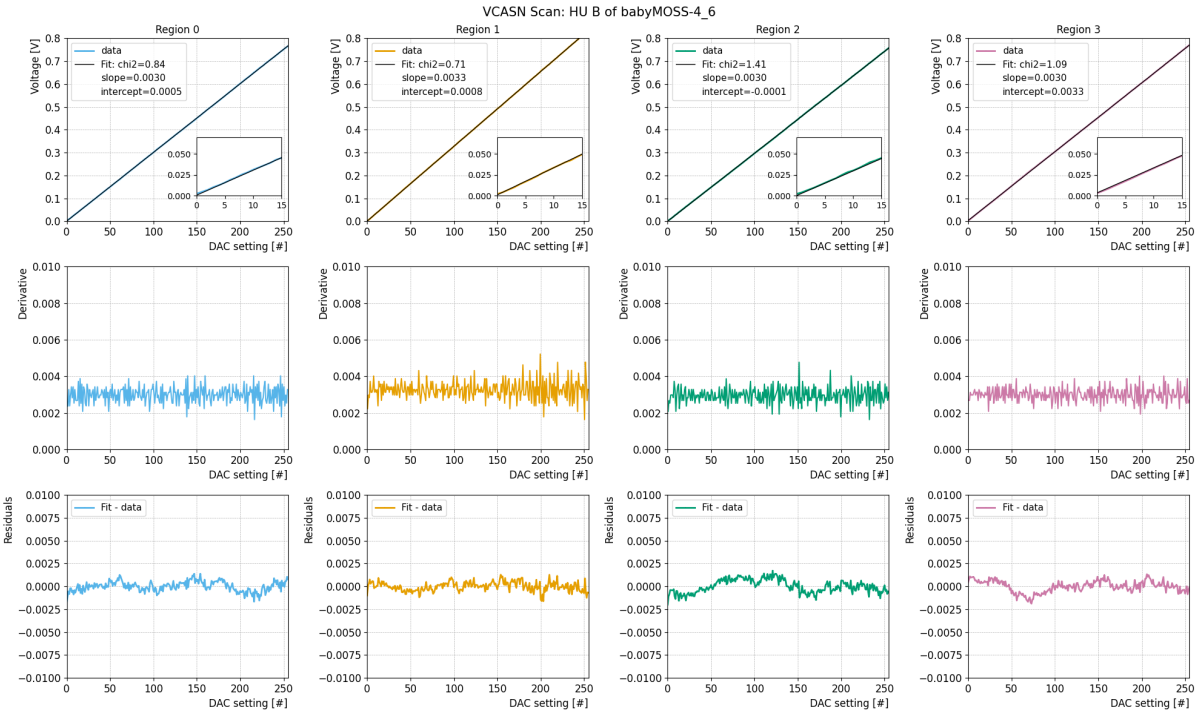

Figure 64. V_{casn} scan of bottom HU from babyMOSS-4_6_W24B5. All top plots are voltage plots, the middle plots are the derivatives and the bottom plots are the residuals. Region 0 is depicted with blue color, region 1 with yellow, region 2 with green and region 3 with pink. Figure produced by the author with the dac_scan.py script created.

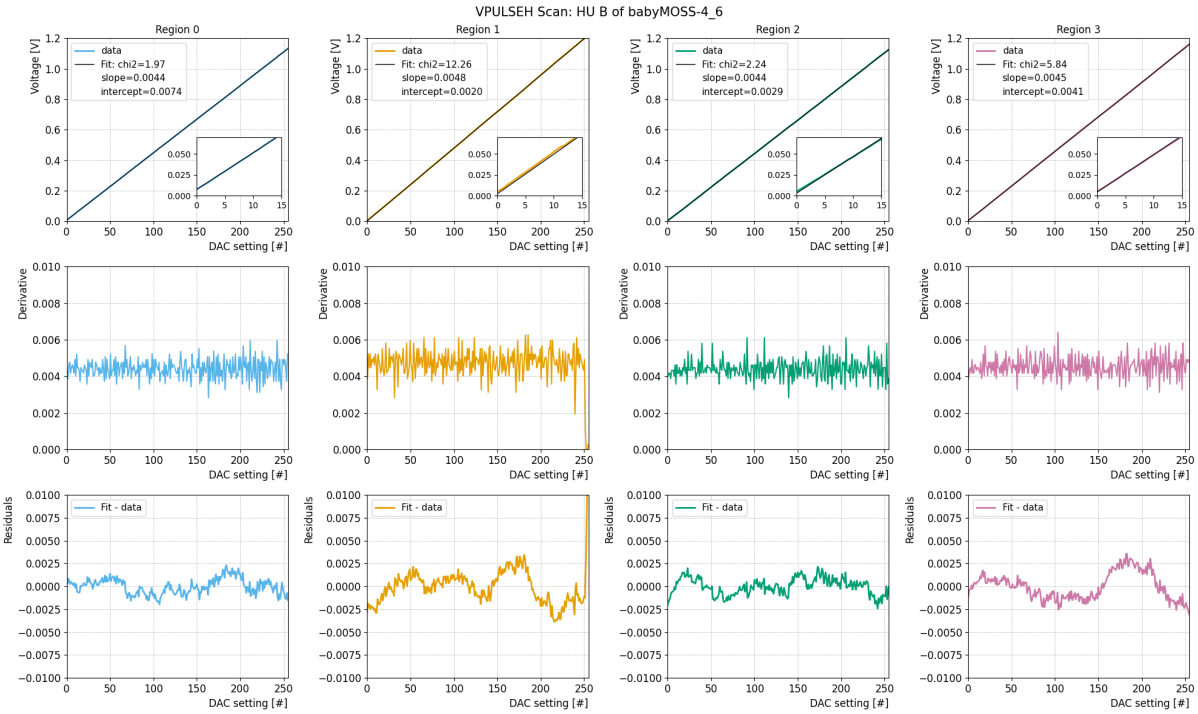

Figure 65. V_{pulseh} scan of bottom HU from babyMOSS-4_6_W24B5. All top plots are voltage plots, the middle plots are the derivatives and the bottom plots are the residuals. Region 0 is depicted with blue color, region 1 with yellow, region 2 with green and region 3 with pink. Figure produced by the author with the dac_scan.py script created.

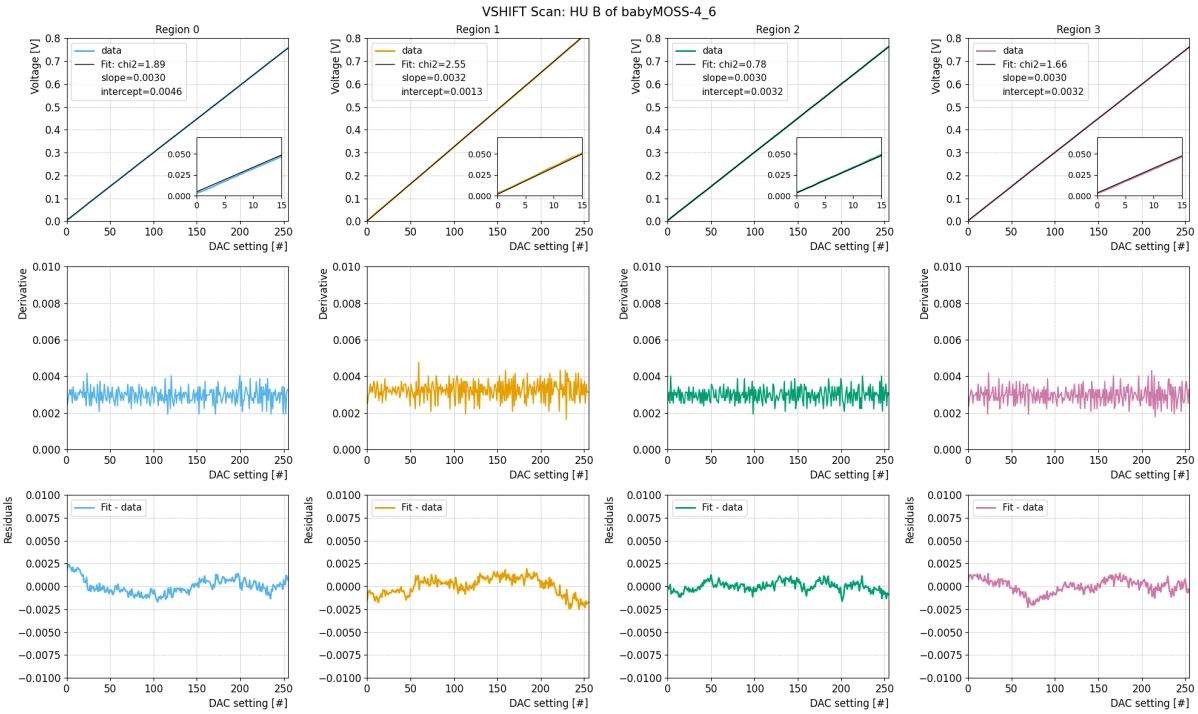

Figure 66. V_{shift} scan of bottom HU from babyMOSS-4_6_W24B5. All top plots are voltage plots, the middle plots are the derivatives and the bottom plots are the residuals. Region 0 is depicted with blue color, region 1 with yellow, region 2 with green and region 3 with pink. Figure produced by the author with the dac_scan.py script created.

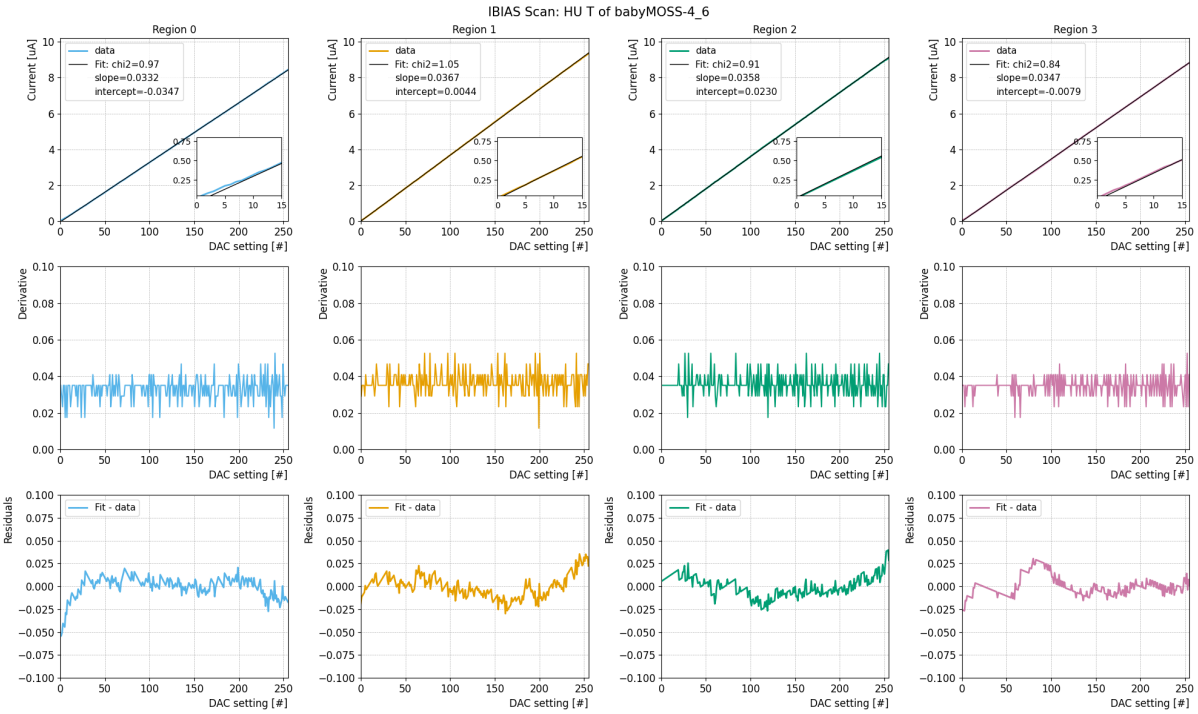

Figure 67. I_{bias} scan of top HU from babyMOSS-4_6_W24B5. All top plots are current plots, the middle plots are the derivatives and the bottom plots are the residuals. Region 0 is depicted with blue color, region 1 with yellow, region 2 with green and region 3 with pink. Figure produced by the author with the dac_scan.py script created.

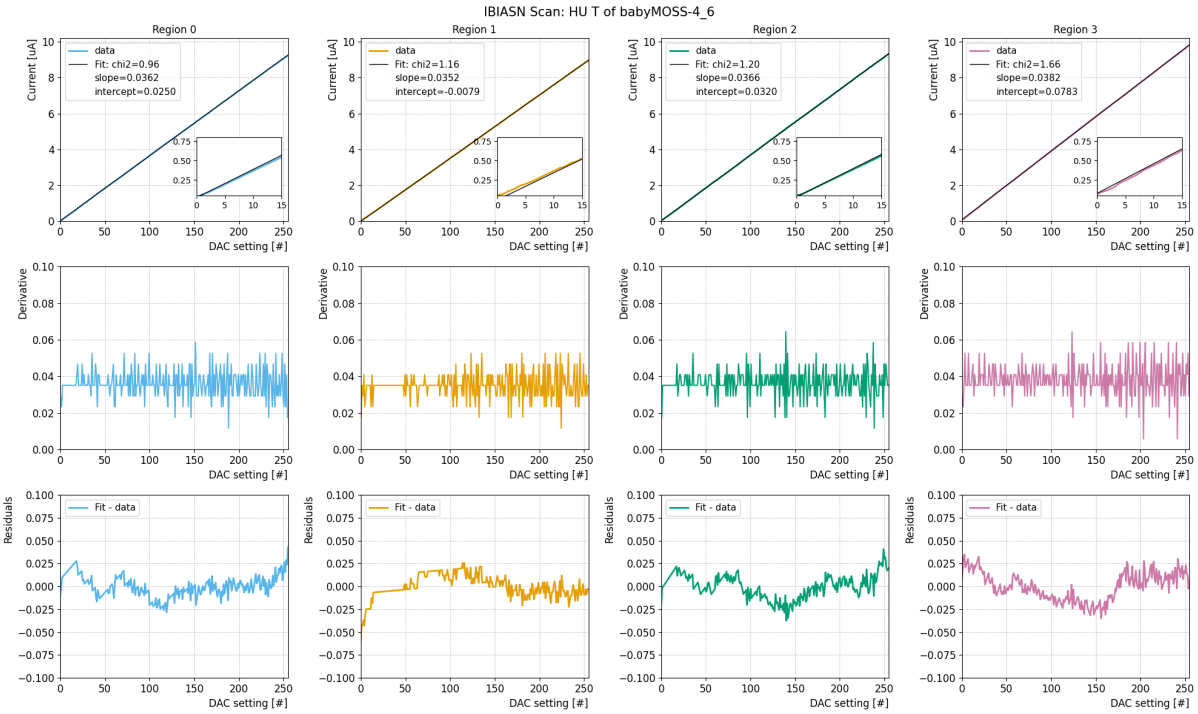

Figure 68. I_{biasn} scan of top HU from babyMOSS-4_6_W24B5. All top plots are current plots, the middle plots are the derivatives and the bottom plots are the residuals. Region 0 is depicted with blue color, region 1 with yellow, region 2 with green and region 3 with pink. Figure produced by the author with the dac_scan.py script created.

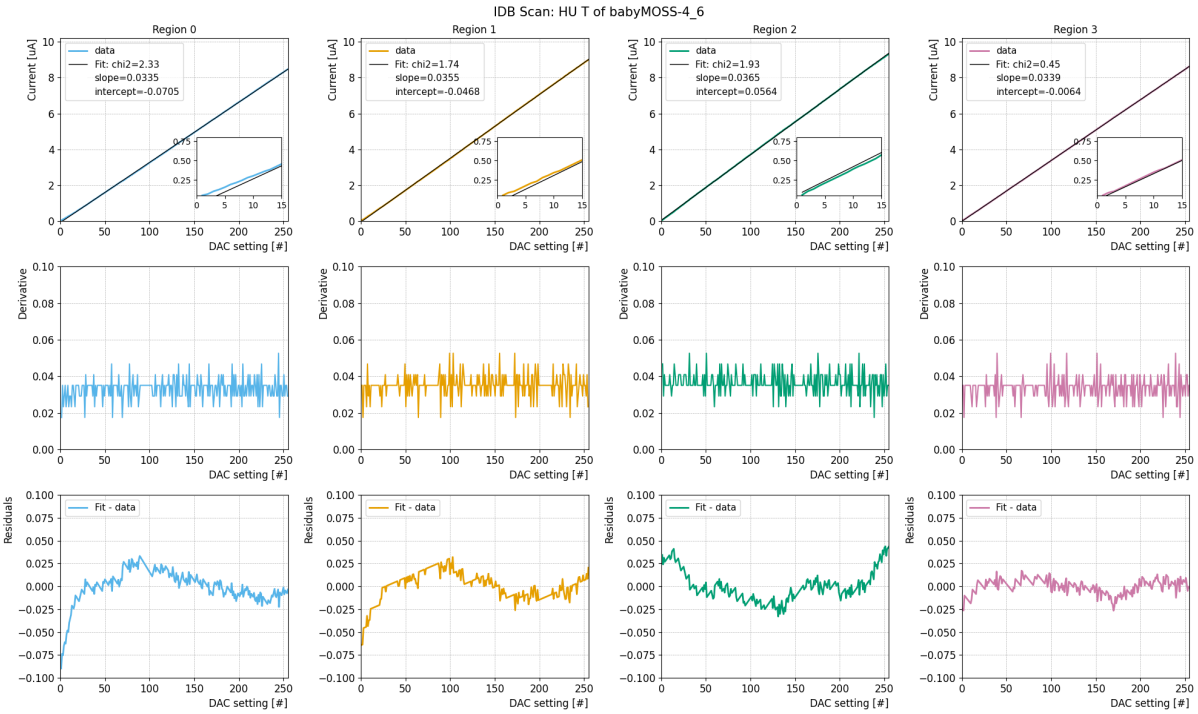

Figure 69. I_{db} scan of top HU from babyMOSS-4_6_W24B5. All top plots are current plots, the middle plots are the derivatives and the bottom plots are the residuals. Region 0 is depicted with blue color, region 1 with yellow, region 2 with green and region 3 with pink. Figure produced by the author with the dac_scan.py script created.

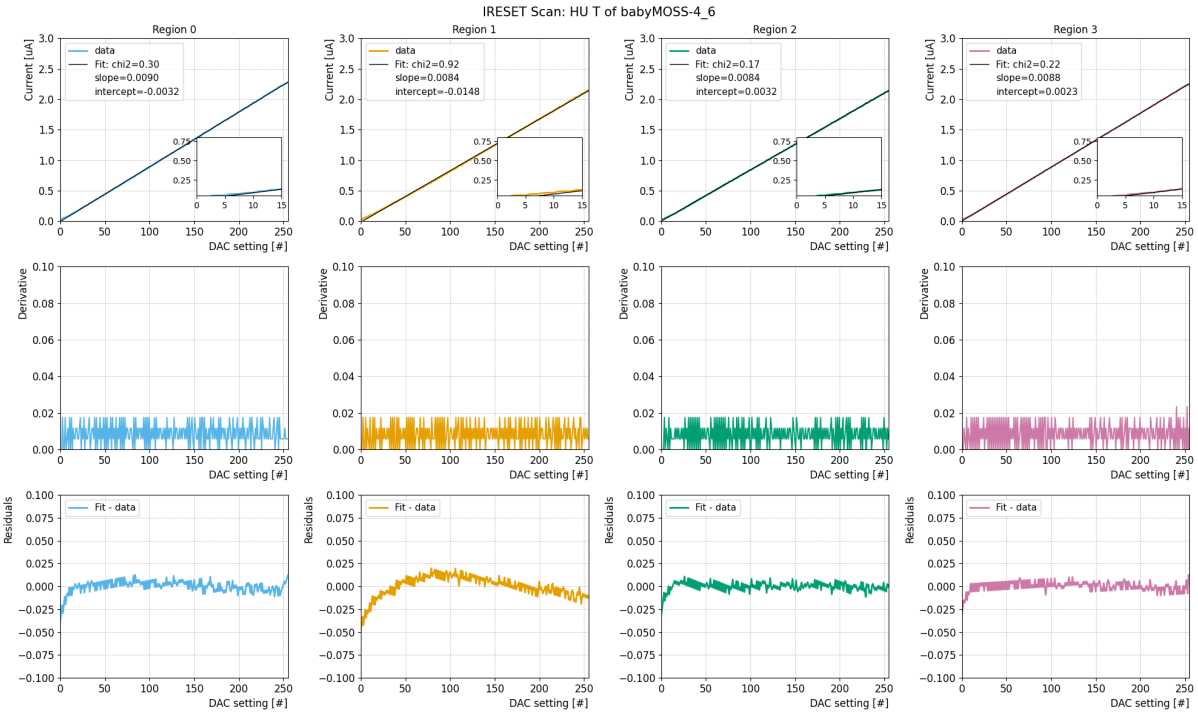

Figure 70. I_{reset} scan of top HU from babyMOSS-4_6_W24B5. All top plots are current plots, the middle plots are the derivatives and the bottom plots are the residuals. Region 0 is depicted with blue color, region 1 with yellow, region 2 with green and region 3 with pink. Figure produced by the author with the dac_scan.py script created.

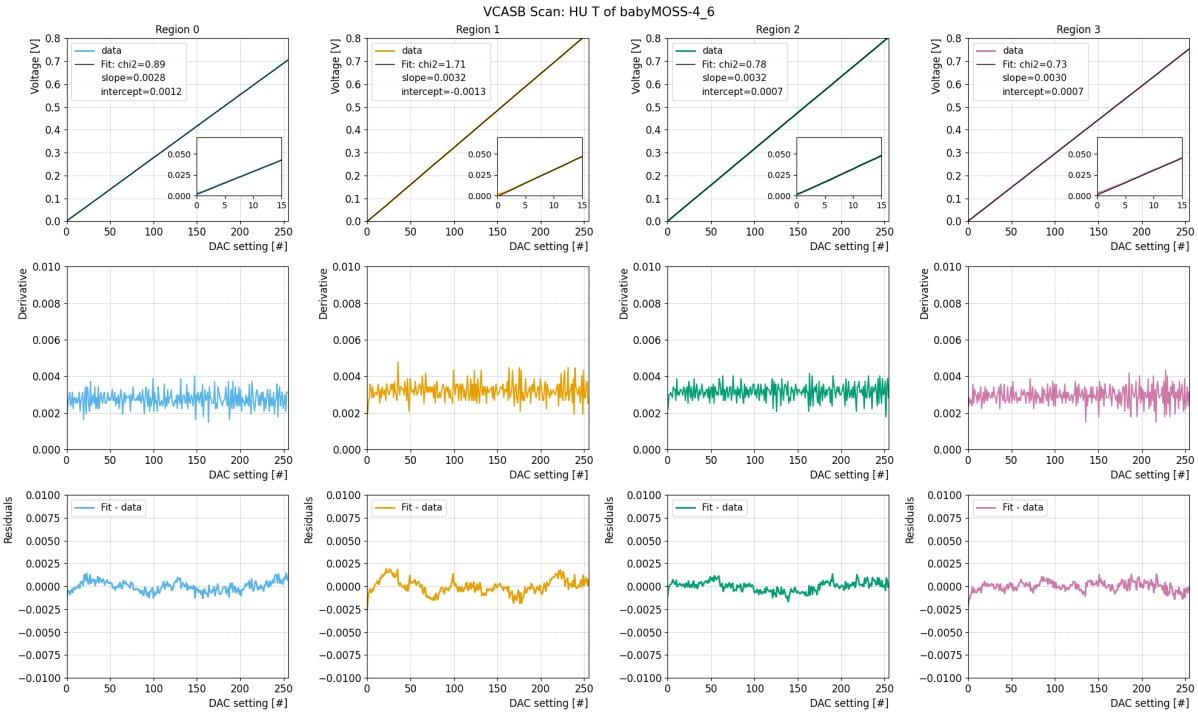

Figure 71. V_{casb} scan of top HU from babyMOSS-4_6_W24B5. All top plots are voltage plots, the middle plots are the derivatives and the bottom plots are the residuals. Region 0 is depicted with blue color, region 1 with yellow, region 2 with green and region 3 with pink. Figure produced by the author with the dac_scan.py script created.

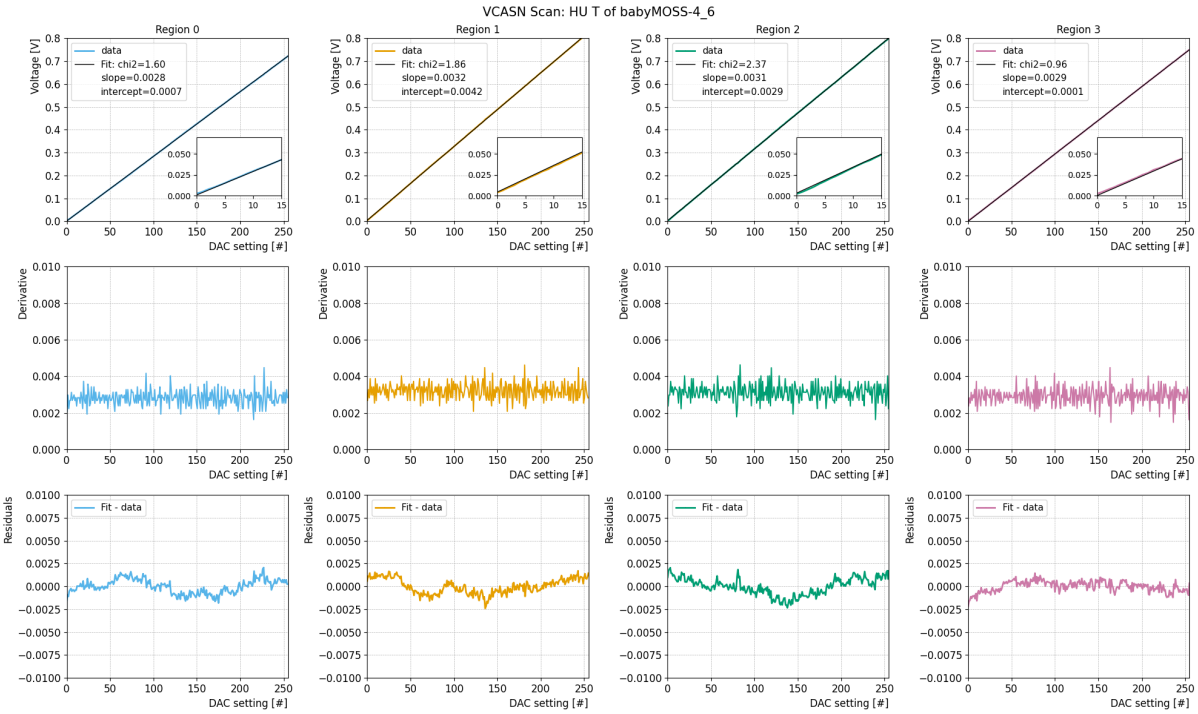

Figure 72. V_{casn} scan of top HU from babyMOSS-4_6_W24B5. All top plots are voltage plots, the middle plots are the derivatives and the bottom plots are the residuals. Region 0 is depicted with blue color, region 1 with yellow, region 2 with green and region 3 with pink. Figure produced by the author with the dac_scan.py script created.

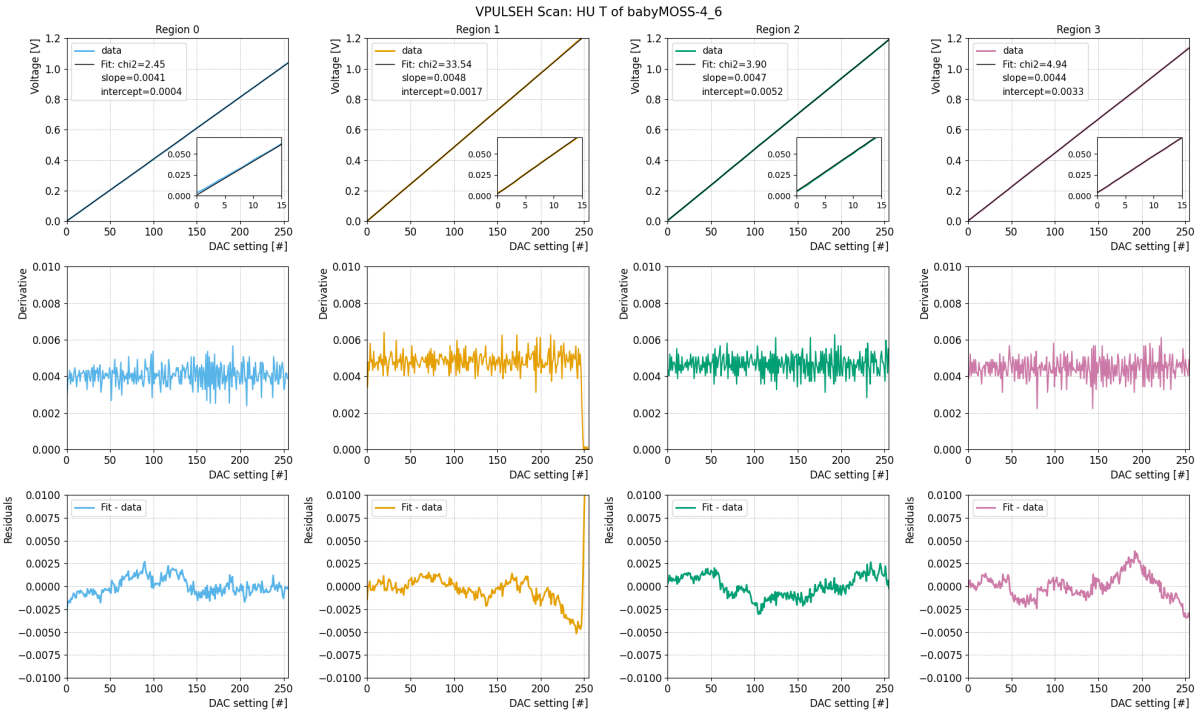

Figure 73. V_{pulseh} scan of top HU from babyMOSS-4_6_W24B5. All top plots are voltage plots, the middle plots are the derivatives and the bottom plots are the residuals. Region 0 is depicted with blue color, region 1 with yellow, region 2 with green and region 3 with pink. Figure produced by the author with the dac_scan.py script created.

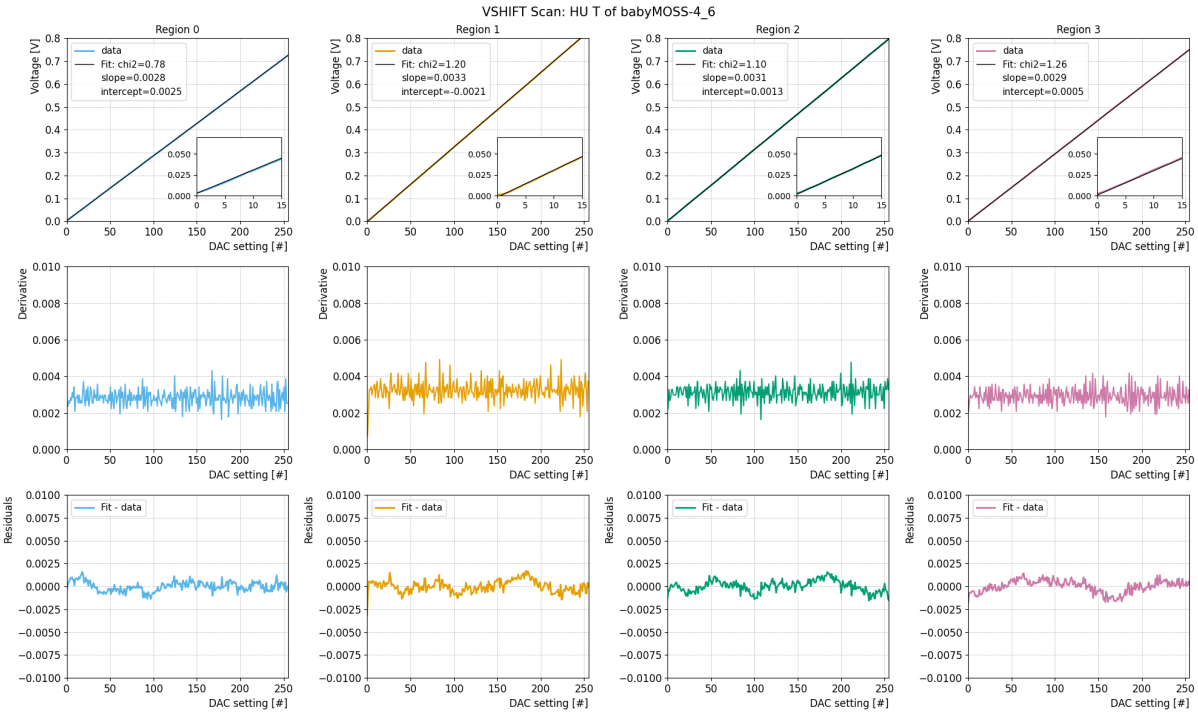

Figure 74. V_{shift} scan of top HU from babyMOSS-4_6_W24B5. All top plots are voltage plots, the middle plots are the derivatives and the bottom plots are the residuals. Region 0 is depicted with blue color, region 1 with yellow, region 2 with green and region 3 with pink. Figure produced by the author with the dac_scan.py script created.

H Irradiated babyMOSS results versus threshold

The following plots are produced as a function of threshold in DAC unis. These plots are not used in the main thesis, since there was a problem with the script that does the trimming of the bandgap. Due to the high noise, when the script tries to identify a voltage or current value and match it with the threshold, the value oscillates between different threshold values, due to the low precision of the DACs. If there were more DACs available and the precision was larger, this problem would not be present. So it was decided, to present the V_{casb} plots, until the trimming of the bandgap is fixed. This is shown in Figure 81, where in the higher threshold region, the FHR in region 0 had a "back and forth" behavior.

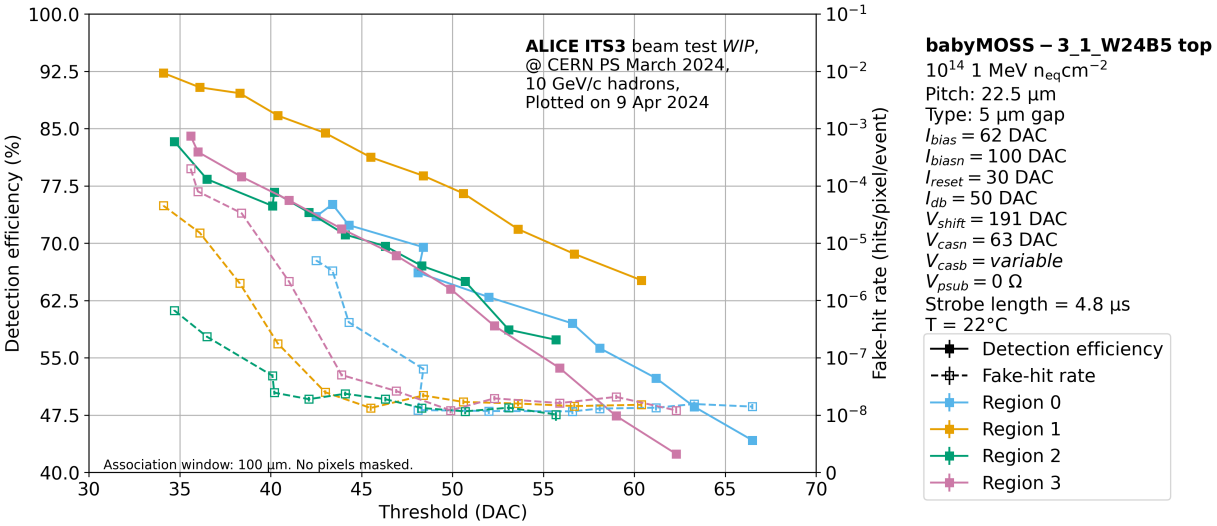

Figure 75. Detection efficiency (solid lines) and fake-hit rate (dashed lines) for different threshold values from the March test beam with the irradiated babyMOSS-3_1_W24B5, with grounded reverse bias and all regions shown. Figure produced by the author.

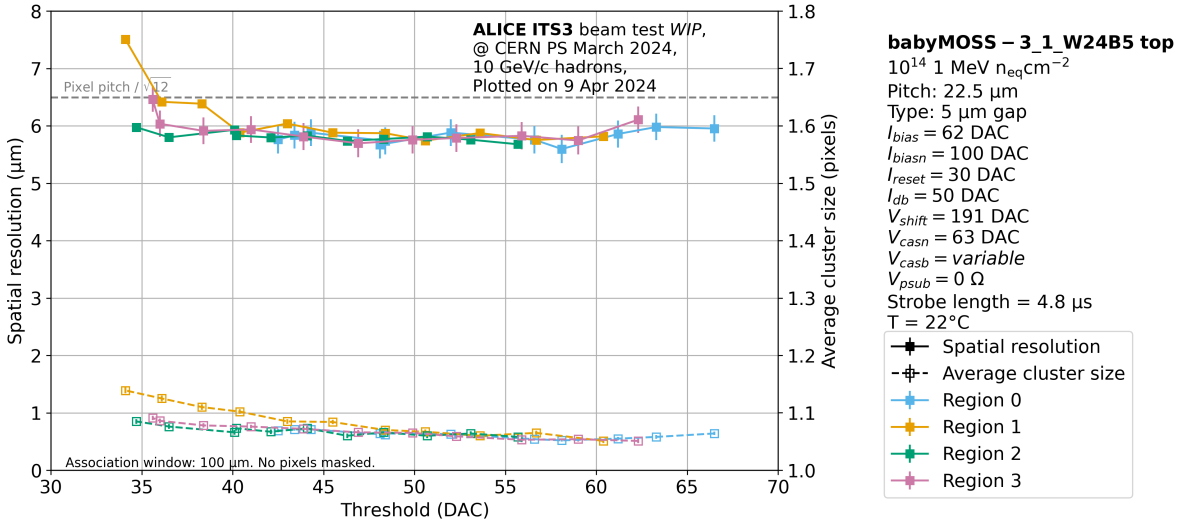

Figure 76. Spatial resolution (solid lines) and average cluster size (dashed lines) for different threshold values from the March test beam with the irradiated babyMOSS-3_1_W24B5, with grounded reverse bias and all regions included. Figure produced by the author.

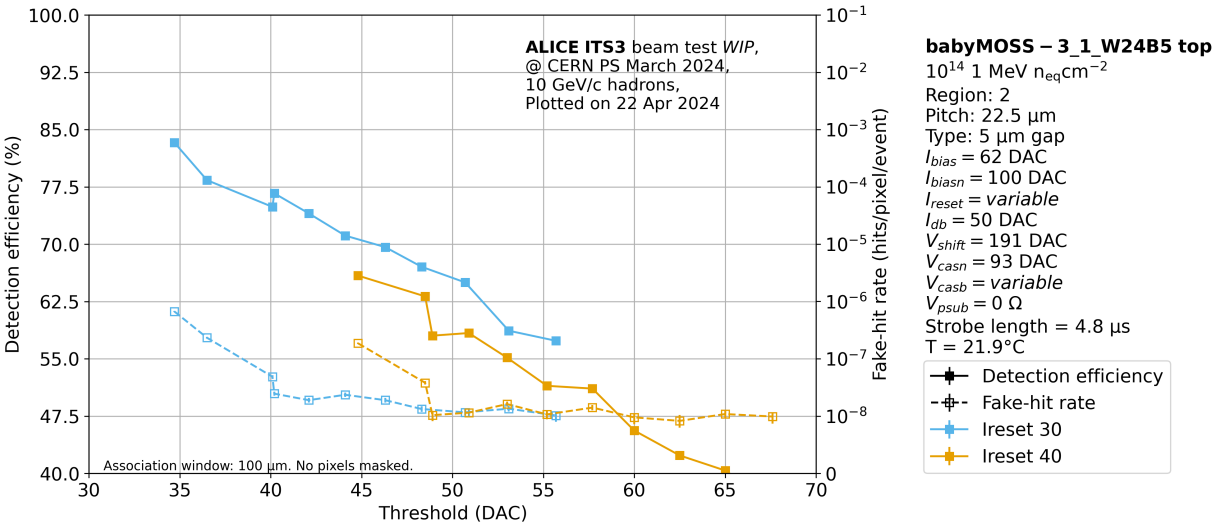

Figure 77. Detection efficiency (solid lines) and fake-hit rate (dashed lines) for different threshold values from the March test beam with region 2 of the irradiated babyMOSS-3_1_W24B5, with grounded reverse bias and variable I_{reset}. Figure produced by the author.

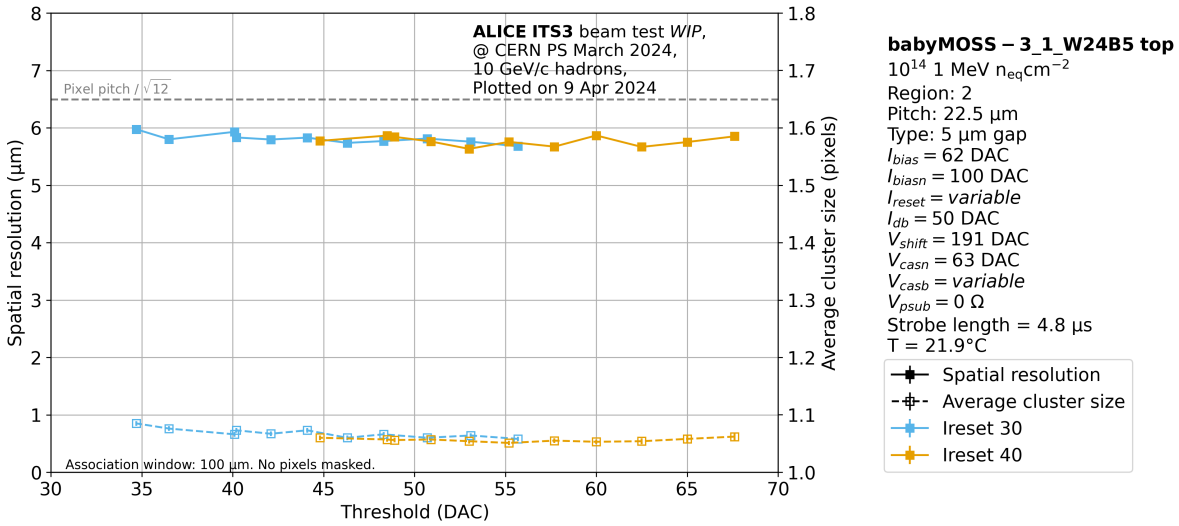

Figure 78. Spatial resolution (solid lines) and average cluster size (dashed lines) for different threshold values from the March test beam with region 2 of the irradiated babyMOSS-3_1_W24B5, with grounded reverse bias and variable I_{reset}. Figure produced by the author.

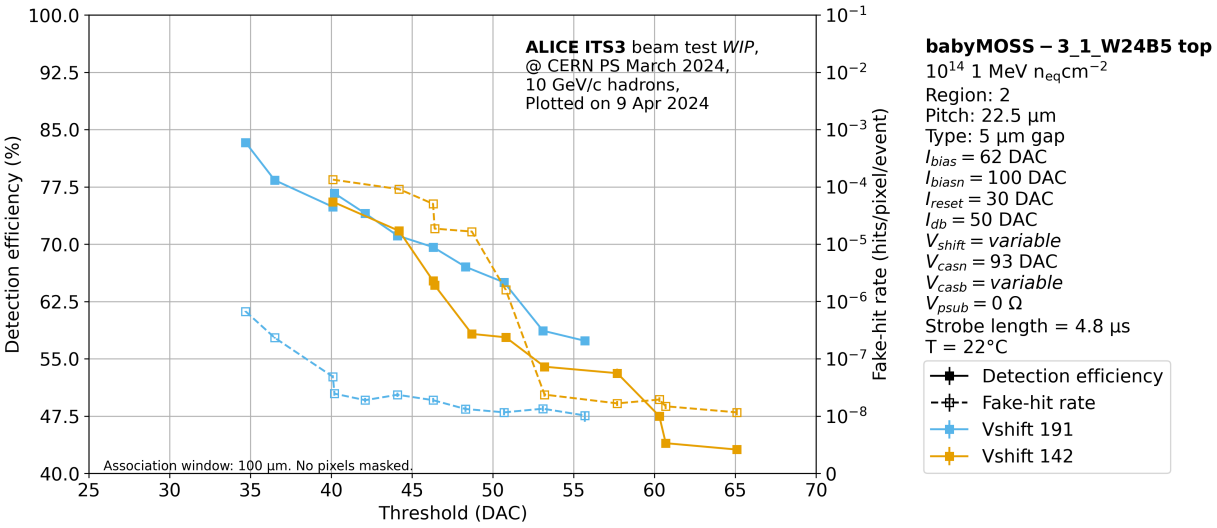

Figure 79. Detection efficiency (solid lines) and fake-hit rate (dashed lines) for different threshold values from the March test beam with region 2 of the irradiated babyMOSS-3_1_W24B5, with grounded reverse bias and variable V_{shift}. Figure produced by the author.

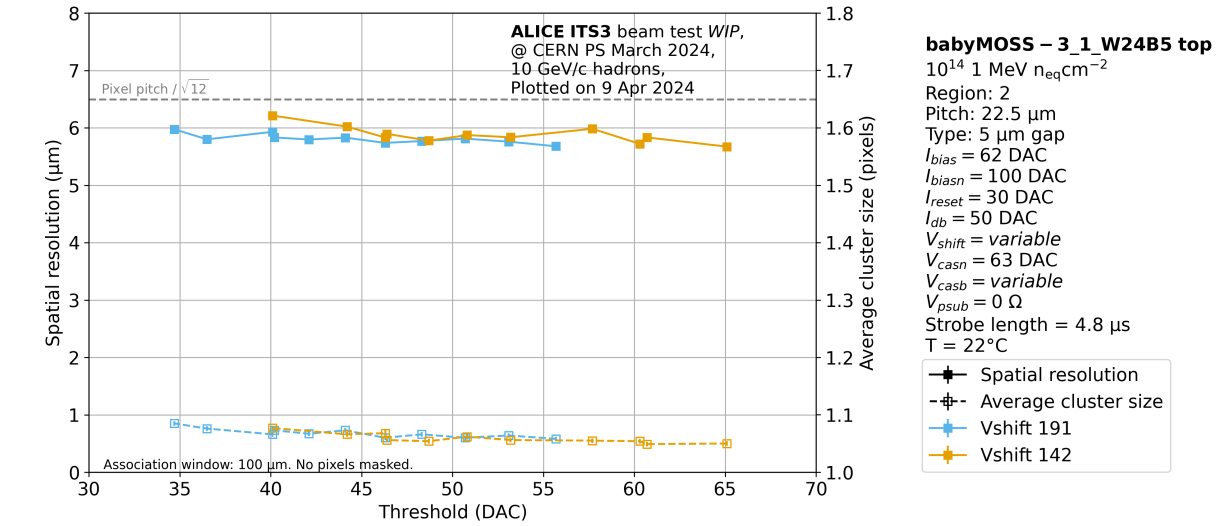

Figure 80. Spatial resolution (solid lines) and average cluster size (dashed lines) for different threshold values from the March test beam with region 2 of the irradiated babyMOSS-3_1_W24B5, with grounded reverse bias and variable V_{shift}. Figure produced by the author.

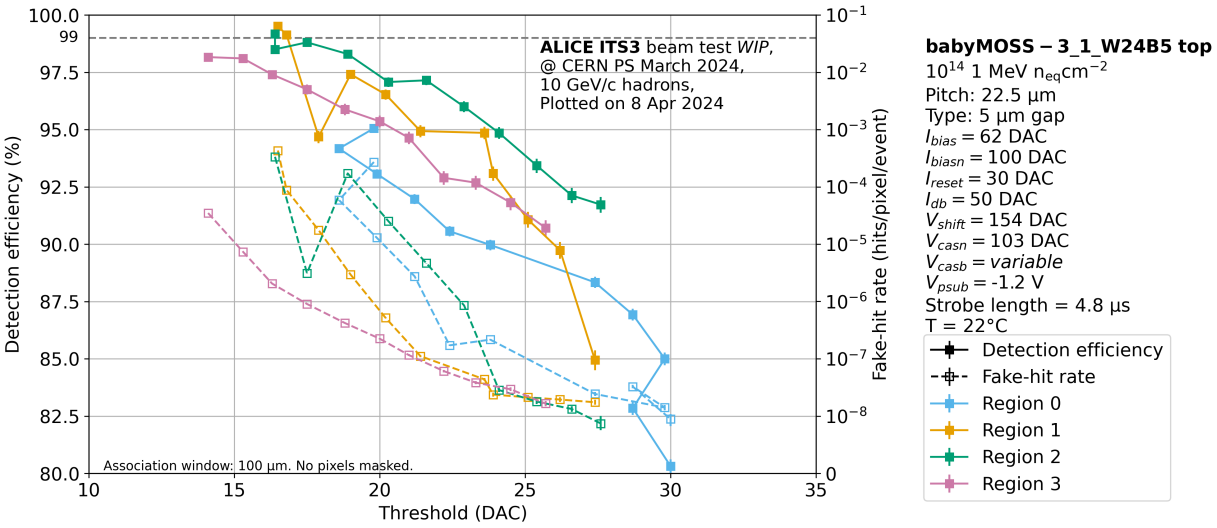

Figure 81. Detection efficiency (solid lines) and fake-hit rate (dashed lines) for different threshold values from the March test beam with the irradiated babyMOSS-3_1_W24B5, with -1.2 V reverse bias and all regions shown. Figure produced by the author.

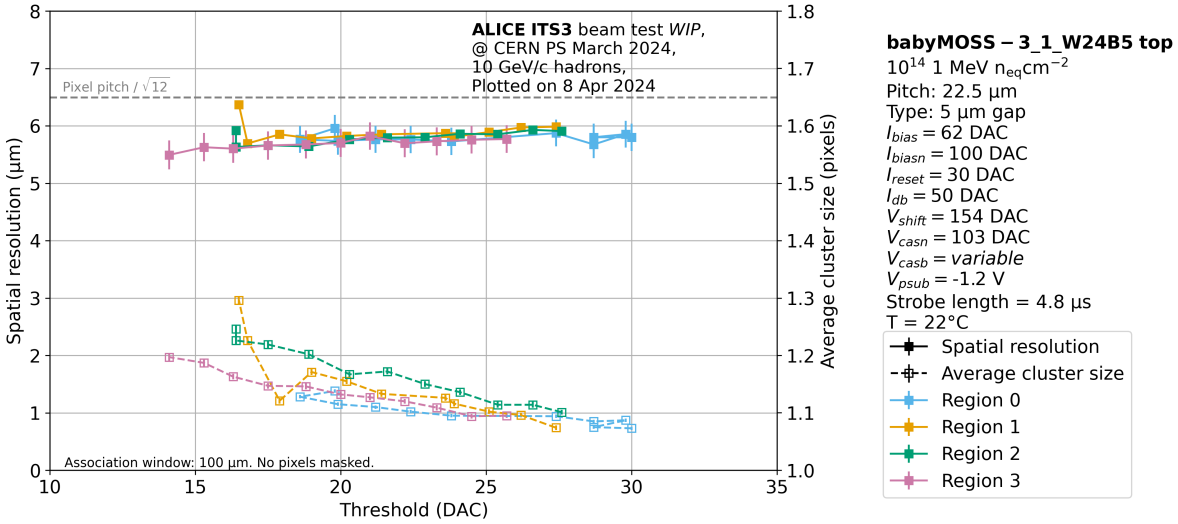

Figure 82. Spatial resolution (solid lines) and average cluster size (dashed lines) for different threshold values from the March test beam with the irradiated babyMOSS-3_1_W24B5, with -1.2 V reverse bias and all regions included. Figure produced by the author.

I Comparison of different irradiated babyMOSS

During the last days of the third test beam, a second babyMOSS was tested, in order to compare its results with the one presented in this thesis. The following plots are for regions 2 and 3 of the two babyMOSSes, with -1.2 V reverse bias and they are both as functions of V_{casb} and threshold. From these Figures, one can notice how the FHR is quite different for the two babyMOSS, and especially in Figure 86, where babyMOSS-2_1_W24B5 has two order of magnitude larger FHR that seems to have an effect on the detection efficiency as well (the shape of the lines becomes the same at low threshold).

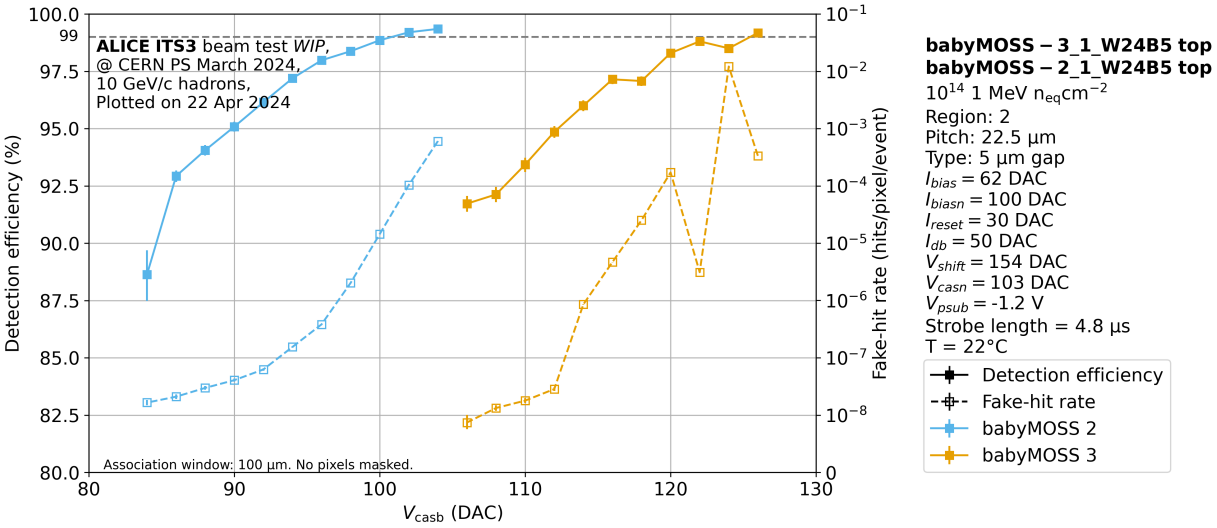

Figure 83. Detection efficiency (solid lines) and fake-hit rate (dashed lines) for different V_{casb} values from the March test beam comparing the irradiated babyMOSS-3_1_W24B5 and babyMOSS-2_1_W24B5, with -1.2 V reverse bias, only for region 2. Figure produced by the author.

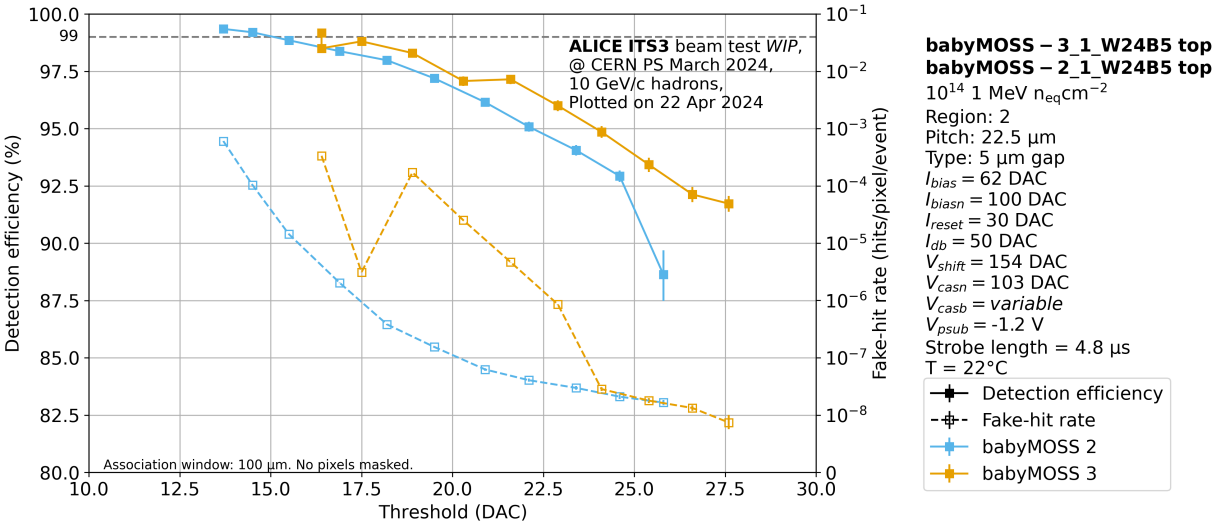

Figure 84. Detection efficiency (solid lines) and fake-hit rate (dashed lines) for different threshold values from the March test beam comparing the irradiated babyMOSS-3_1_W24B5 and babyMOSS-2_1_W24B5, with -1.2 V reverse bias, only for region 2. Figure produced by the author.

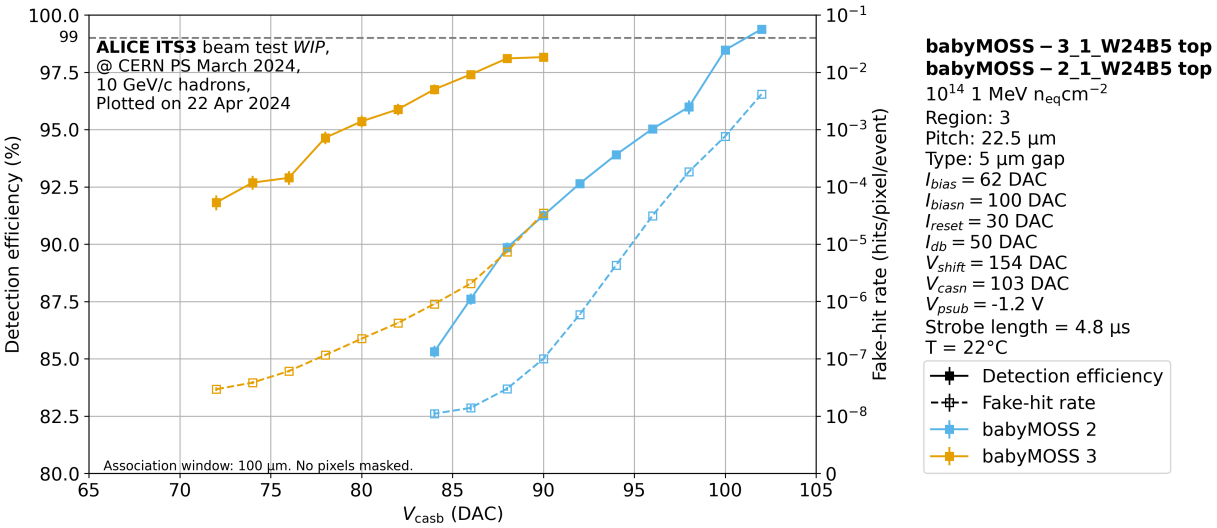

Figure 85. Detection efficiency (solid lines) and fake-hit rate (dashed lines) for different V_{casb} values from the March test beam comparing the irradiated babyMOSS-3_1_W24B5 and babyMOSS-2_1_W24B5, with -1.2 V reverse bias, only for region 3. Figure produced by the author.

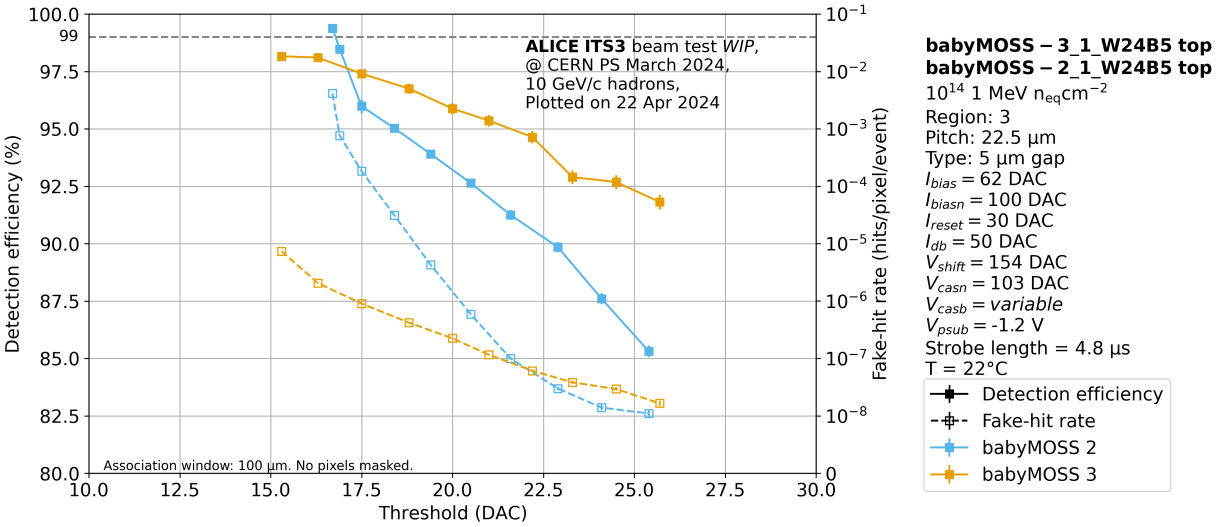

Figure 86. Detection efficiency (solid lines) and fake-hit rate (dashed lines) for different threshold values from the March test beam comparing the irradiated babyMOSS-3_1_W24B5 and babyMOSS-2_1_W24B5, with -1.2 V reverse bias, only for region 3. Figure produced by the author.